

Methods for Enhancing the High Field in vivo Sensitivity of Long-T1 Nuclear Spins via Dynamic Nuclear Polarization

THÈSE N° 5756 (2013)

PRÉSENTÉE LE 31 MAI 2013
À LA FACULTÉ DES SCIENCES DE BASE
GROUPE COMMENT
PROGRAMME DOCTORAL EN PHYSIQUE

ÉCOLE POLYTECHNIQUE FÉDÉRALE DE LAUSANNE

POUR L'OBTENTION DU GRADE DE DOCTEUR ÈS SCIENCES

PAR

Tian CHENG

acceptée sur proposition du jury:

Prof. H. Rønnow, président du jury
Prof. A. Comment, Prof. R. Gruetter, directeurs de thèse
Prof. J.-Ph. Ansermet, rapporteur
Prof. P. Tordo, rapporteur
Dr B. van den Brandt, rapporteur



ÉCOLE POLYTECHNIQUE
FÉDÉRALE DE LAUSANNE

Suisse
2013

Love doesn't mean anything if you're not willing to make a commitment;
You have to think not only about what you want, but about what she wants.
Not just now, but in the future.
— Nicholas Sparks, *Safe Haven*

To those I love...

Acknowledgments

As time flies, four years PhD study in CIBM becomes a very special part of my memories. During this period, colleagues, friends and family members brought me valuable life experience which encourages me to finish the study. Therefore I would like to express my deepest appreciation to them.

To Prof. Arnaud Comment, my thesis supervisor. Thank you for offering me this great opportunity to do PhD with you in the DNP field. Without your guide and your interesting ideas I would not experience all these wonderful technologies and studies about DNP.

To Prof. Rolf Gruetter, my thesis co-supervisor. Thank you for giving me valuable suggestions and advices to my work, presentations and writings.

To Dr. Ben van den Brandt and Dr. Patrick Hautle, my collaborators in PSI. Thank you for sharing your wide range of knowledges with me and for kindly treating me as a group member.

To Ms. Jessica Bastiaansen, Mr. Riccardo Balzan and Mr. Andrea Capozzi, my teammates and also polarized friends. Thank you for bringing me lots of happiness not only in the lab with your efficient work but also with the beers after work .

To Dr. Arthur Magill and Mr. Yves Pilloud, my teachers in the RF lab. Thank you so much for always being patient to teach me how to design, simulate and improve the RF circuits.

To Dr. Najat Salameh and Dr. Mor Mishkovsky, my teammates for the DNP projects. Thank you for helping me to set up the experiment protocols, to modify imaging sequences and even to translate my thesis.

To Dr. Yuhei Takado, Dr. Lijing Xin and Dr. Hongxia Lei, my listeners. Thank you for teaching me, encouraging me and sharing your happiness with me as a big family.

To my sister and parents. Thank you for always supporting my "selfish" ideas, giving me maximal freedom and letting me be independent ten years ago. I am so proud of you.

Last but not the least to my wife, Yu Xia. Thank you for always accompanying and supporting me. Without you I definitely cannot make all these happen.

Lausanne, 12 May 2013

T.C.

Abstract

Dissolution dynamic nuclear polarization (DNP) became a very powerful technique for enhancing nuclear magnetic resonance (NMR) signals of insensitive nuclear spins for analytical chemistry and biomedical research. In this thesis we describe methods and hardware developments to maximize the NMR signals of substrates of biological interest containing insensitive nuclear spins with long longitudinal relaxation time T_1 . The overall aim was to extend the acquisition time window of *in vivo* metabolic studies.

The dissolution and transfer procedures of the hyperpolarized molecules from the polarizer to the imager prior to *in vivo* measurements lead to unavoidable losses in nuclear polarization which are difficult to evaluate once the solution has been injected into an animal. We proposed a method to measure the polarization of the hyperpolarized molecules inside the imager bore, 3s following dissolution, at the time of the injection. Our method includes a radical scavenging process that does not lead to reduced sample concentration and takes place within a couple of seconds following the dissolution in order to minimize the losses due to the presence of paramagnetic polarizing agent in the infusate.

The stable radicals used as polarizing agents in the solid-state DNP process become undesirable in the liquid-state, following dissolution, due to the paramagnetic relaxation effect on the hyperpolarized nuclear spins and their toxicity to biological tissues. We demonstrated the feasibility of preparing hyperpolarized alcohol aqueous solutions free of stable radicals by using spin-labeled thermoresponsive hydrophilic polymer networks. We applied this method to hyperpolarize *tert*-butanol, which has been recently shown to be a promising contrast agent for perfusion imaging, and ethanol, which is an interesting substrate for probing liver metabolism.

Extensive DNP studies on bio-compatible molecules labeled with ^{15}N and ^{89}Y , which have exceptionally long- T_1 , have been carried out to maximize their polarization for *in vivo* metabolic and perfusion hyperpolarized MR studies. We designed an *in vivo* protocol for investigating the normal brain uptake of choline via injection of hyperpolarized ^{15}N -choline into rats. We successfully performed the first *in vivo* hyperpolarized ^{89}Y experiments using bio-compatible $\text{Y}[\text{DOTA}]^-$ compounds.

Sensitivity and B_1 homogeneity are two essential factors for magnetic resonance spectroscopy (MRS) and magnetic resonance imaging (MRI). As the magnetic field strength increases, NMR probes become increasingly difficult to design. The main challenges are the limited probe size, radiation and sample losses caused by the reduced wavelengths as well as B_1 field inhomogeneity. We designed and built surface and birdcage coils for *in vivo* MR

Abstract

measurements in ultra high magnetic field. Bench tests and *in vivo* imaging data recorded with these surface and birdcage coils at 9.4T and 14.1T showed that the surface coil loops had to have a limited diameter due to sensitivity issue and radiofrequency (RF) power limitation. For birdcage coils the major losses were not inside the sample or via radiation, but rather caused by the low filling factor.

keywords: *dissolution dynamic nuclear polarization (DNP), nuclear magnetic resonance (NMR), in vivo magnetic resonance spectroscopy (MRS) and imaging (MRI), longitudinal relaxation time, radical scavenging, spin-labeled hydrophilic polymer network(SL-hydrogel), birdcage coil.*

Zusammenfassung

Die dynamische Kernspinpolarisation (DNP) mit einem Auflösungsverfahren, ist mittlerweile eine vielversprechende Technik der analytischen Chemie und biomedizinischen Forschung zur Erhöhung kernmagnetischer Resonanzsignale (NMR) unempfindlicher Kernspins. In dieser Arbeit werden die Methoden und Systemteile dargestellt, welche zur die Maximierung der NMR Signale von Substanzen mit unempfindlichen und lange longitudinale Relaxationszeiten T_1 beinhaltenden Kernspins benutzt wurden.

Die Auflösungs- und Übertragungsverfahren der hyperpolarisierten Moleküle vom Polarisator zum Scanner vor der eigentlichen *in vivo* Messung führen zu unvermeidlichen Verluste in Kernpolarisation, die nach der Injektion ins Tier schwierig zu beurteilen sind. Wir haben eine Methode vorgeschlagen, bei welcher die Polarisation der hyperpolarisierten Moleküle im Magnet 3 Sekunden nach der Auflösung zum Zeitpunkt der Injektion gemessen wird. Zusätzlich ist eine radikalfangende Methode beschrieben, die die Konzentration der hyperpolarisierten Flüssigkeit nicht reduziert und innerhalb weniger Sekunden nach der Auflösung erledigt, um Verluste bedingt durch der Anwesenheit paramagnetischer Zentren im Infusat zu minimieren. Die stabilen freien Radikale, die als polarisierendes Mittel durch chemische Dotierung während des DNP Prozesses verwendet werden, sind im auflösten Zustand aufgrund der paramagnetischen Relaxation der hyperpolarisierten Nukleonen und der Toxizität für biologisches Gewebe unerwünscht. Wir konnten die Herstellung von hyperpolarisierten Alkohollösungen frei von stabilen Radikalen durch die Verwendung spinmarkierter thermoreagierender hydrophiler Polymernetzwerke zeigen. Diese Methode wurde angewandt auf die Polarisation des *tert*-Butanols, einem vielversprechenden Kontrastmittel für die Perfusion, und des Ethanol, einem interessanten Substrat zur Untersuchung des Leberstoffwechsels.

Ausführliche DNP Studien über biokompatiblen Verbindungen markiert mit den Isotopen ^{15}N und ^{89}Y , die eine außergewöhnlich lange Relaxationszeit T_1 aufweisen, wurden durchgeführt, um eine maximierte Polarisation für *in vivo* Stoffwechsel- und Perfusionsstudie. Wir entwickelten ein *in vivo*-Protokoll zur Untersuchung der normalen Cholinaufnahme des Gehirns nach Injektion von hyperpolarisiertem ^{15}N -Cholin. Wir haben das erste *in vivo* ^{89}Y Experiment mit biokompatible Y[DOTA] durchgeführt.

Empfindlichkeit und B_1 Homogenität sind zwei wesentliche Faktoren der Magnetresonanz-Spektroskopie (MRS) und -Tomographie (MRT). Bei zunehmender Magnetfeldstärke wird die Konstruktion der Hochfrequenzspule schwieriger. Die Hauptherausforderungen dabei sind die begrenzte Größe der Spulen als auch die Strahlungs- und Probenverluste, welche durch die reduzierten Wellenlängen sowie die B_1 Feldinhomogenität verursacht werden. Wir

Zusammenfassung

entworfen und konstruierten verschiedene Oberflächen- und Vogelkäfigspulen für *in vivo* MR-Messungen im Ultrahochfeld. Laborversuche und *in vivo* Tomographiedaten aufgenommen mit eben diesen Oberflächen- und Vogelkäfigspulen bei 9,4T und 14,1T zeigten einerseits, dass Oberflächenspulen mit kleinerem Durchmesser weniger Empfindlichkeitsprobleme und Hochfrequenz Leistungsbegrenzungen aufwiesen, und andererseits, dass bei den Vogelkäfigspulen die großen Verluste weder in der Probe noch durch die Strahlung, sondern durch den geringen Füllfaktor verursacht wurden.

Stichwörter: *Dynamische Kernspinpolarisation (DNP) mit Auflösungsverfahren; kernmagnetische Resonanz (NMR); in vivo Magnetresonanztomographie (MRS) und -tomographie (MRT); longitudinale Relaxationszeit; Abfang freier Radikale; spinmarkierte thermoreagierende hydrophile Polymernetzwerke (SL-hydrogel); Vogelkäfigspule.*

Résumé

La polarisation dynamique nucléaire (Dynamic Nuclear Polarization - DNP) est une technique puissante qui permet d'augmenter le signal obtenu par résonance magnétique nucléaire (RMN) provenant de noyaux à faible sensibilité. Cette technique ouvre ainsi le champ des possibles en chimie analytique et dans le cadre de la recherche biomédicale. Dans cette thèse, nous décrivons les développements méthodologiques et instrumentaux nécessaires à maximiser les signaux RMN de substrats d'intérêt biologique contenant des spins nucléaires de faible sensibilité avec de longs temps de relaxation longitudinale T_1 . Le but global était d'élargir la fenêtre temporelle d'acquisition pour pouvoir effectuer des études métaboliques *in vivo*.

La dissolution ainsi que les procédures de transfert des molécules hyperpolarisées du polariseur vers l'imageur en amont des mesures *in vivo* mènent inévitablement à des pertes de la polarisation nucléaire qui demeurent difficiles à évaluer une fois que la solution est injectée dans l'animal. Dans ce contexte, nous proposons une méthode pour mesurer la polarisation des molécules hyperpolarisées à l'intérieur du tunnel de l'imageur, 3s après la dissolution, au moment de l'injection. Notre méthode comprend un processus de neutralisation des radicaux n'entraînant pas de réduction de la concentration de l'échantillon et prenant place dans les deux secondes qui suivent la dissolution afin de minimiser les pertes dues à la présence d'agent polarisant paramagnétiques dans la solution infusée.

Les radicaux libres utilisés comme agents polarisants pour les processus de DNP à l'état solide deviennent indésirables lors du transfert à l'état liquide, après la dissolution, en raison des effets de relaxation paramagnétique des spins nucléaires hyperpolarisés et de leur toxicité pour les tissus biologiques. Nous avons alors montré la faisabilité de préparer des solutions hyperpolarisées à base d'eau et d'alcool, dépourvues de tout radical libre, en utilisant des réseaux de polymères hydrophiles et thermo-sensible aux spins. Nous avons utilisé cette méthode pour polariser du tert-butanol qui a récemment été utilisé comme agent de contraste prometteur pour l'imagerie de perfusion, mais également l'éthanol qui représente un substrat d'intérêt pour suivre le métabolisme hépatique.

Par ailleurs, des études extensives par DNP sur des molécules biocompatibles marquées au ^{15}N et ^{89}Y , dont les T_1 sont particulièrement longs, ont été menées pour maximiser leur polarisation et pouvoir effectuer des recherches *in vivo* sur le métabolisme et la perfusion. Nous avons mis en place un protocole expérimental pour étudier *in vivo* la consommation cérébrale en choline en injectant de la choline marquée au ^{15}N chez le rat. Nous avons par la suite également effectué avec succès la première étude *in vivo* avec du ^{89}Y en utilisant des

composés biocompatibles de Y[DOTA].

Enfin, la sensibilité et l'homogénéité du champ B_1 sont deux facteurs essentiels pour la spectroscopie et l'imagerie par résonance magnétique (SRM et IRM, respectivement). Quand l'intensité du champ magnétique principal augmente, les sondes RMN (ou résonateurs) deviennent de plus en plus difficiles à construire. Les défis principaux sont leur taille, la radiation et les pertes provenant de l'échantillon, ces dernières étant causées par des longueurs d'onde réduites, aussi bien que les inhomogénéités de champ B_1 . Malgré ces contraintes, nous avons conçu et construit des résonateurs de surface et en cage d'oiseau pour les mesures RMN *in vivo* à très haut champ. Des expériences de faisabilité, ainsi que des données d'imagerie acquises *in vivo* effectuées avec ces sondes de surface et en cage d'oiseau à 9,4 T et 14,1 T ont montré que les bobines constituant la sonde de surface doivent avoir un diamètre limité en raison de contraintes dues à la sensibilité et à la limitation de puissance radiofréquence utilisable. En ce qui concerne les sondes en cage d'oiseau, les pertes principales ne provenaient pas de l'échantillon ou de la radiation, mais plutôt du faible facteur de remplissage de ce résonateur.

Mots clés : *Polarisation dynamique nucléaire (PDN) ; Résonance magnétique nucléaire (RMN) ; Spectroscopie magnétique nucléaire (SMN) ; Imagerie par résonance magnétique (IRM) ; technique de dissolution rapide ; temps de relaxation longitudinale ; neutralisation des radicaux ; le sonde en cage d'oiseau.*

Contents

Acknowledgments	v
Abstract (English/Deutsch/Français)	vii
Table of contents	xv
Introduction	1
1 Basics about NMR and DNP	5
1.1 Fundamental of Spins	6
1.1.1 Spins	6
1.1.2 Polarization	7
1.2 Pulsed NMR	8
1.2.1 Bloch equation and relaxation processes	11
1.3 Dynamic Nuclear Polarization (DNP)	13
1.3.1 Global mechanism of DNP	14
1.3.2 Spin temperature	16
1.3.3 Overhauser Effect	17
1.3.4 Solid Effect	18
1.3.5 Thermal mixing	20
1.4 Other hyperpolarization methods	21
1.4.1 Spin-Exchange Optical Pumping(SEOP)	21
1.4.2 ParaHydrogen Induded Polarization(PHIP)	22
1.5 Methods to determine the longitudinal relaxation time T_1	23
1.5.1 Magnetization recovery schemes	23
1.5.2 Polarization decay scheme	24
2 <i>In vivo</i> DNP-enhanced MR experiment protocol	29
2.1 Standard experimental protocol for dissolution DNP	30
2.1.1 Dissolution DNP setup	30
2.1.2 NMR probes	30
2.1.3 DNP sample preparation	33
2.1.4 DNP experiment protocol	35
2.2 Method to minimize and monitor in situ the polarization losses	35

Contents

2.3 Discussion	39
3 Producing radical-free hyperpolarized solutions for <i>in vivo</i> MR	45
3.1 Introduction	46
3.2 Materials and Methods	47
3.2.1 Thermoresponsive spin-labeled hydrogel	47
3.2.2 DNP procedure	48
3.2.3 balanced Steady State Free Precession (b-SSFP) sequence	48
3.3 Results	50
3.4 Discussion	50
3.5 Conclusion	52
4 Preliminary results on ^{15}N and ^{89}Y labeled tracers for <i>in vivo</i> hyperpolarized NMR	57
4.1 Introduction	58
4.2 ^{15}N choline	59
4.3 ^{89}Y chloride and DOTA	61
5 MR probes for <i>in vivo</i> MRS and MRI at ultra high magnetic field	65
5.1 Introduction	66
5.2 Surface coil	68
5.2.1 Design of the surface coil	69
5.2.2 Results	70
5.3 Birdcage coil	71
5.3.1 Resonance modes of the birdcage coil	71
5.3.2 RF design of HP birdcage coil	73
5.3.3 Results and Discussions	75
5.3.4 Preparation of BP birdcage coil and preliminary test results	77
5.3.5 Conclusions	80
Conclusions and future perspectives	83
Appendix A DNP performance of biradicals	87
Appendix B X-ray induced radicals	89
Appendix C Optimization of dissolution parameters	91
Appendix D Polarization level determination	93
D.1 Classical polarization determination	93
D.2 Polarization build-up simulation	94
D.3 Polarization calculation through build-up	95
D.3.1 varying flip angle	96
D.3.2 varying time interval	96
D.3.3 Summary	97

Curriculum Vitae

Introduction

Magnetic resonance imaging (MRI) and magnetic resonance spectroscopy (MRS) are non-invasive techniques based on nuclear magnetic resonance (NMR) and widely used in medicine for acquiring anatomic and metabolic information about diseased tissues. ^1H , as a spin-1/2 element with the largest nuclear gyromagnetic ratio γ , is the nucleus of choice for *in vivo* NMR due to the large signal related to its high natural isotopic (99.99%) and biological abundance (63% for human). However, ^1H spectra are often limited by the strong water signal and the relatively small spectral dispersion due to the narrow resonance frequency range. ^{13}C , ^{15}N and ^{31}P , are biologically relevant spin-1/2 nuclei involved in a wide range of metabolic processes. Their γ is substantially lower than that of ^1H and their natural isotopic and biological abundance is very low. These characteristics indicate relatively low NMR sensitivity on one hand, but little MRS and MRI background signals on the other hand. How to efficiently improve the MR sensitivity of these nuclei recently became a very important field of research, in particular in the context of metabolic studies.

The Dynamic Nuclear Polarization (DNP) method, based on the saturation of the electron spin resonance (ESR) transition of free radicals to transfer the unpaired electron spin polarization to the surrounding nuclear spins in solid samples, was theoretically and experimentally studied since 1950s to produce polarized targets for nuclear and particle physics research. Large polarizations were observed not only for proton but also for deuteron, lithium and other nuclei. Recently, a novel technique consisting in the dissolution of DNP-enhanced solid samples to obtain a nuclear spin polarization up to four orders of magnitude larger than the room-temperature thermal polarization in liquids was applied to MRS and MRI. It became a prominent technique not only for chemical analysis but also for visualizing *in vivo* the bio-distribution of hyperpolarized substrates and their downstream metabolites. The intrinsic limitation of the technique is the finite life time of the hyperpolarized state of the molecule, which is determined by the longitudinal relaxation time of the nuclei of interest. The hyperpolarized state cannot be recovered once the magnetization is destroyed and therefore, although it is very intense, the signal is only available for a limited amount of time. Hence, the strategy for DNP becomes to find biologically relevant substrates with long T_1 nuclear spins and maximize their polarization for *in vivo* metabolic studies. Low- γ nuclear spins with spin-1/2 can have usually long T_1 , in particular ^{13}C , ^{15}N and ^{89}Y spins on molecular sites with no direct bond to protons, e.g. carboxyl group and trimethyl-ammonium cation etc., are

excellent candidates for DNP and exhibit a remarkably long T_1 of at least 50s and up to several hundred seconds.

In order to improve the sensitivity of hyperpolarized MRS and MRI, a large effort has been so far devoted to the optimization of the sample preparation (e.g. choice of radicals^{1;2}, solvents³, adjunction of Gd(III) complexes^{4;5}) and hardware developments^{1;6;7}, to maximize the solid-state nuclear spin polarization. A hardware characteristic of dissolution DNP is that the DNP and the MRS/MRI are done in separate magnets, at different fields. The dissolved sample is usually transported from one to the other by blowing it through a thin plastic tube. However, little has been done to minimize the polarization losses once the sample is dissolved. Losses due to relaxation can be essentially minimized by, on one hand, alleviating relaxation pathways through cancellation of some interactions between the nuclear spins of interest and their environment and, on the other hand, reducing the time delay between the dissolution step and the injection into the subject under investigation. The use of deuterated solvents to dissolve the samples can significantly reduce the dipolar relaxation but in most cases the residual paramagnetic centers (polarizing agents and Gd^{3+} ions used during the solid-state polarization process) will be the main source of relaxation. In addition, the toxicity issue due the presence of a few mM of free radical in the hyperpolarized solution has to be addressed and so far this problem has been largely overlooked.

Another important aspect of hyperpolarized MRS and MRI is that the acquisitions are essentially single-shot experiment. Since it is impossible to perform signal averaging, it is important to have highly sensitive NMR probes. For *in vivo* experiments, surface coils are the most adapted for obtaining the higher local signal-to-noise ratio (SNR).

Scope of the thesis

The results presented in this thesis were obtained using a home-built 5T polarizer. The main goals was to optimize the DNP enhancement in samples containing long- T_1 ^{13}C , ^{15}N , and ^{89}Y spins in molecules that can be used for *in vivo* metabolic studies and molecular imaging. The aim was to first, optimize the polarization both in solid-state and liquid-state, and to reduce the polarization losses during the sample transfer; second, investigate how to efficiently scavenge or trap the radicals used for the DNP process and therefore increase the longitudinal relaxation time and acquisition window for *in vivo* studies; third, build sensitive MR probes for *in vivo* metabolic studies in ultra high field NMR scanner. Low toxicity, larger polarization and longer longitudinal relaxation time in the liquid state are three requirements for improved hyperpolarized MRS and MRI experiments that we attempted to meet.

In chapter 1, a brief overview on pulsed NMR will be given to introduce the basic concepts of NMR and relaxation mechanisms of nuclear spins. The principles and mechanisms of the different DNP processes will then be briefly described. To highlight the diversity of hyperpolarization techniques other methods, such as parahydrogen induced polarization (PHIP) and spin-exchange optical pumping (SEOP), will also be introduced. The chapter will

end with a discussion of the three different methods usually used to determine longitudinal relaxation time.

A short description of the DNP setup used for this work will be presented in the first part of chapter 2. Various recipes and strategies for optimal sample preparation will be discussed. The second part of the chapter will focus on the development of a unique protocol for *in vivo* hyperpolarized MRS and MRI experiments comprising *in situ* polarization measurement prior to injection. The protocol was used in the frame of a metabolic study in rat skeletal muscle. Methods to efficiently scavenge the residual nitroxyl radicals present in the hyperpolarized liquids using deuterated ascorbate are presented at the end of the chapter.

Chapter 3 introduces a novel method to hyperpolarize liquids using thermoresponsive spin-labeled hydrogel. Since the radicals are covalently attached to the hydrogel, it was possible to prepare radical-free hyperpolarized ^{13}C -labeled *tert*-butanol and ethanol solutions following dissolution with adapted dissolution parameters. This method was used to obtain ^{13}C imaging in a mouse brain.

Results of hyperpolarized ^{15}N for determining *in vivo* choline uptake in rat brain and preliminary results of hyperpolarized ^{89}Y complexes are shown in chapter 4.

Chapter 5 first introduces the design of surface coils used for *in vivo* MRS measurements. RF circuit analysis, bench test results and results of *in vitro* experiments are presented. In the second part of the chapter, the performances of two high-pass birdcage coils designed for NMR experiments at 9.4T and 14.1T and one band-pass coil developed for the 14.1T scanner are discussed. These coils were optimized to obtain a highly homogeneous B_1 field for *in vivo* MRS/MRI experiments at ultra high magnetic field.

At the end of the thesis an overall conclusion is drawn and some future perspectives related to this thesis are highlighted.

References

- [1] J. H. Ardenkjaer-Larsen, B. Fridlund, A. Gram, G. Hansson, L. Hansson, M. H. Lerche, R. Servin, M. Thaning, and K. Golman. Increase in signal-to-noise ratio of > 10,000 times in liquid-state nmr. *Proceedings of the National Academy of Sciences of the United States of America*, 100(18):10158–10163, 2003.
- [2] L. Lumata, S. J. Ratnakar, A. Jindal, M. Merritt, A. Comment, C. Malloy, A. D. Sherry, and Z. Kovacs. Bdpa: An efficient polarizing agent for fast dissolution dynamic nuclear polarization nmr spectroscopy. *Chemistry-a European Journal*, 17(39):10825–10827, 2011.
- [3] F. Kurdzesau, B. van den Brandt, A. Comment, P. Hautle, S. Jannin, J. J. van der Klink, and J. A. Konter. Dynamic nuclear polarization of small labelled molecules in frozen water-alcohol solutions. *Journal of Physics D-Applied Physics*, 41(15), 2008.
- [4] J. H. Ardenkjaer-Larsen, S. Macholl, and H. Johannesson. Dynamic nuclear polarization with trityls at 1.2 k. *Applied Magnetic Resonance*, 34(3-4):509–522, 2008.

Contents

- [5] L. Lumata, M. E. Merritt, C. R. Malloy, A. D. Sherry, and Z. Kovacs. Impact of $gd3+$ on dnp of $[1-13c]$ pyruvate doped with trityl ox063, bdpa, or 4-oxo-tempo. *J Phys Chem A*, 116(21):5129–38, 2012.
- [6] J. H. Ardenkjaer-Larsen, A. M. Leach, N. Clarke, J. Urbahn, D. Anderson, and T. W. Skloss. Dynamic nuclear polarization polarizer for sterile use intent. *Nmr in Biomedicine*, 24(8):927–932, 2011.
- [7] S. Jannin, A. Comment, F. Kurdzesau, J. A. Konter, P. Hautle, B. van den Brandt, and J. J. van der Klink. A 140 ghz prepolarizer for dissolution dynamic nuclear polarization. *Journal of Chemical Physics*, 128(24), 2008.

1 Basics about NMR and DNP

Abstract

NMR is a non-invasive technique to probe the magnetic properties of the molecules in the solid-state, liquid state and *in vivo*. In particular, information relative to the chemical structure and the environment of the molecules can be extracted from frequency spectrum obtained by Fourier transforming the temporal response of the nuclear spins excited by RF pulses. Since the signal intensity of conventional pulsed NMR depends on the thermal polarization of the nuclear spins, which is usually very small at ambient temperature, DNP can lead to tremendous SNR ratio enhancement of insensitive nuclear spins with low gyromagnetic ratio and low natural isotropic abundance. An overview of the basics of pulsed NMR and DNP mechanisms is given in this chapter.

1.1 Fundamental of Spins

1.1.1 Spins

NMR technique probes molecules magnetic properties through the intrinsic nuclear angular momentum \vec{J} , a momentum combination of the constituents of nucleus, protons and neutrons, and their orbital momentum. This angular momentum can be expressed as,

$$\hat{J} = \hat{I} \cdot \hbar \quad (1.1)$$

where \hbar is the reduced Planck's constant, also known as the Dirac's constant, and \hat{I} is the total nuclear spin momentum. The spin quantum number I , measurable quantity of \hat{I} , can only be a multiple of half-integer as protons and neutrons have the same spin quantum number of 1/2 and the orbital quantum number is an integer. The magnetic quantum number of the spin, m_I represents the spin state which can take a value from $-I$ to I in a step of 1. The total spin can be zero which leads to a non-magnetic atom. All nuclei in the periodic table can be categorized into three types according to their total spin number:

- a) Non-magnetic nuclei with $|I| = 0$;
- b) Nuclei with $|I| = 1/2$;
- c) Quadrupolar nuclei with $|I| > 1/2$.

As this thesis concentrates on the DNP of long- T_1 nuclei with spin-1/2, for sake of simplicity only nuclear spins with $|I| = 1/2$ will be treated and discussed. Table 1.1 shows all NMR-detectable nuclei that will be discussed in this thesis. Note that only elements with spins $|I| \neq 0$ can be detected by NMR.

Nucleus	Net spin	γ [MHz/T]	N.A. [%]
1H	1/2	42.58	99.985
2H	1	6.54	0.015
^{13}C	1/2	10.71	1.11
^{15}N	1/2	-4.32	0.37
^{31}P	1/2	17.25	100
^{89}Y	1/2	0.8	100
^{129}Xe	1/2	0.8	75.1

Table 1.1: List of the nuclear species relevant for the DNP-enhanced NMR experiments treated in the present thesis along with their gyromagnetic ratio and natural abundance.

The magnetic property of a nuclear spin with angular momentum \vec{J} is defined by its magnetic moment $\vec{\mu}$ given by,

$$\vec{\mu} = \gamma \vec{J} = \gamma \hbar \vec{I}. \quad (1.2)$$

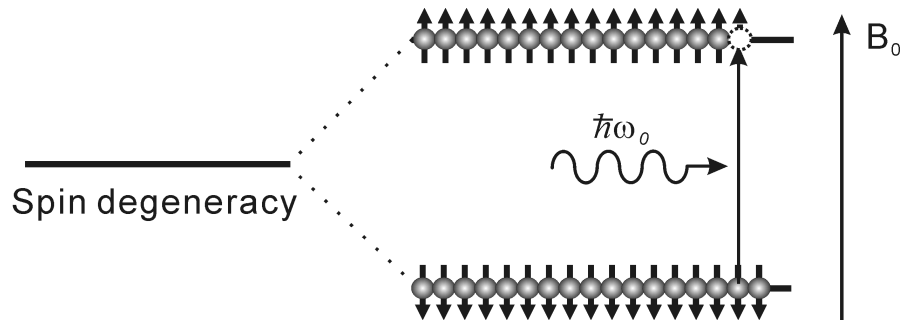


Figure 1.1: Spin population distribution at thermal equilibrium ($\gamma < 0$) and spin transition induced by energy quantum of $\hbar\omega_0$.

where γ is the characteristic gyromagnetic ratio of the spin species. The gyromagnetic ratio is an intrinsic characteristics of a spin (electron spins have a gyromagnetic ratio which is 658 times larger than for ^1H). Gyromagnetic ratios of several NMR nuclei of interest are shown in table 1.1.

When a spin is placed in an external magnetic field \vec{B}_0 , the spin starts to precess around \vec{B}_0 due to the torque exerted on the magnetic moment $\vec{\mu}$ which is described as,

$$\frac{d\vec{\mu}}{dt} = \gamma(\vec{\mu} \times \vec{B}_0). \quad (1.3)$$

The solution of equation 1.3 gives a trajectory for a spin at thermal equilibrium as a cone-shape motion around \vec{B}_0 with a Larmor frequency.

$$\omega_0 = \gamma B_0. \quad (1.4)$$

The application of \vec{B}_0 lifts the degeneracy of the spin energy and create $2I + 1$ energy levels. This splitting is called Zeeman effect. The possible energy levels for the spins are determined by the magnetic quantum number m_s through the relationship,

$$E_m = -\hbar\gamma B_0 m_s. \quad (1.5)$$

The energy difference between two neighboring energy levels is given by,

$$\Delta E = \gamma B_0 \hbar = \hbar\omega_0. \quad (1.6)$$

1.1.2 Polarization

As described in 1.1.1, spins with $I = 1/2$ can be either in a "up" or "down" states, which are separated with an energy difference of a quantum with a frequency of ω_0 . Although spin

transitions induced by thermal fluctuations continuously take place, the population ratio between the two spin states stays constant at thermal equilibrium. As nuclear spins are fermion, the population on both energy levels follows Boltzmann distribution and is described as,

$$\frac{N_{\uparrow}}{N_{\downarrow}} = e^{-\frac{\Delta E}{kT}} \quad (1.7)$$

where N_{\uparrow} and N_{\downarrow} represent the spin population of the spin up and spin down states, respectively. T is the sample temperature and k is the Boltzmann constant. The polarization P is defined as,

$$P = \frac{N_{\downarrow} - N_{\uparrow}}{N_{\downarrow} + N_{\uparrow}} = \frac{1 - \frac{N_{\uparrow}}{N_{\downarrow}}}{1 + \frac{N_{\uparrow}}{N_{\downarrow}}} = \tanh \frac{\hbar\gamma B_0}{2kT} \quad (1.8)$$

an indirect quantity which reflects the spin states population. A null polarization means that the spin population on both energy levels is equal. A unity polarization corresponds to the case in which the spins are all located in one of two energy levels. A positive polarization expresses the fact that the population of the low energy level is larger than that of the higher energy level, which is the case at thermal equilibrium. On the contrary, if the population of the high energy level is larger the polarization is negative. With the high-temperature approximation ($\frac{\gamma B_0 \hbar}{2kT} \ll 1$), the expression for the polarization can be simplified as,

$$P \approx \frac{\gamma B_0 \hbar}{2kT} \quad (1.9)$$

From equation 1.9, we see that the polarization at thermal equilibrium depends on two external factors: the applied magnetic field \vec{B}_0 and the temperature T . At ambient temperature and in a magnetic field of 9.4 T, ^1H polarization is around 0.0032% and ^{13}C polarization is around 0.0008%. Due to its large gyromagnetic ratio, the electron spin polarization is much higher, around 2.11%. If the temperature is decreased to 1 K, the ^1H polarization increases to 1%, and the electron spin polarization is almost 100%.

1.2 Pulsed NMR

Section 1.1 described the spin behavior in an external magnetic field at thermal equilibrium and introduced the definition of polarization. The detectable quantity in NMR is the magnetization M , the sum of all the magnetic moments of the spins. Although the number of spins in a sample is usually very large, the net magnetization is in fact rather small due to the small nuclear spin polarization. Therefore, NMR is considered as an insensitive method compared to other spectroscopy methods.

Unlike current or voltage which can be directly measured, magnetization can only be indirectly measured. According to the Maxwell equations shown in equation 1.10, a fluctuating

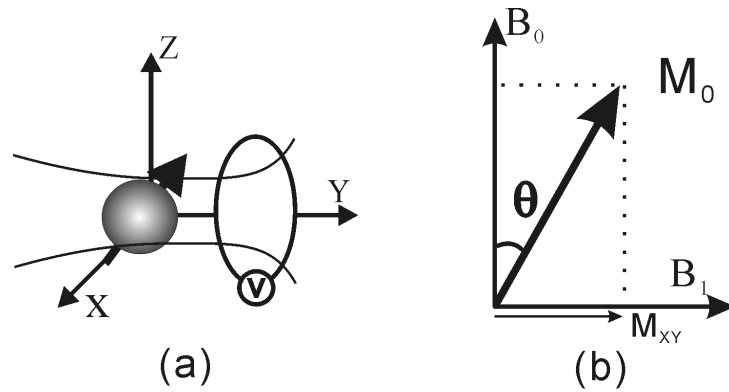


Figure 1.2: (a) Schematics of the spin excitation and NMR signal received through a loop; (b) Nuclear spin magnetization following the application of a RF pulse with a flip angle of θ .

magnetic field \vec{B} generates electric field \vec{E} inducing current across a conducting loop, e.g. RF coil, and the electric displacement field \vec{D} in a conductor generates magnetic field \vec{H} around it. So the basic idea of NMR is to perturb the thermal equilibrium state of the spin system and measure the alternative magnetic signals generated in the sample. The maximal NMR signal is detected when the detecting surface is perpendicular to the magnetic flux (figure 1.2a). For convenience we define the laboratory frame with the magnetic field \vec{B}_0 along the Z axis and the main RF coil axis inside the XY plane.

$$\begin{aligned}\nabla \times \vec{E} &= -\frac{\partial \vec{B}}{\partial t} \\ \nabla \times \vec{H} &= \vec{J}_0 - \frac{\partial \vec{D}}{\partial t}\end{aligned}\quad (1.10)$$

To detect the nuclear magnetization, two prerequisites need to be fulfilled: first, an additional magnetic field, B_1 field should be applied orthogonal to B_0 , to create an alternative magnetic flux; second, the NMR signal which is generated by the disturbed spin system, needs to be transformed into a measurable electrical signal. In practice, as shown in figure 1.2b, one conducting loop representing the RF coil is implemented perpendicular to the XY plane to generate the B_1 field by injecting a high-power current into the loop and then used to detect the NMR signal shortly after switching off the excitation current. The measured NMR signal is dependent not only on the magnetization of the sample, but also on the sensitivity of the RF coil. Details about the RF coils used in this work will be given in chapter 5.

Rotating frame

Since the spins precess around \vec{B}_0 with a Larmor frequency ω_0 , it is convenient to set up a new frame of reference called the rotating frame, which rotates around the Z axis of the laboratory frame. The rotating frequency of the new frame is set to $\Omega = \omega_{\text{RF}} - \omega_0$, which is

called offset frequency, where ω_{RF} is the excitation frequency. Combined with the B_1 field created by the RF coil, the effective magnetic field B_{eff} acting on the spins is given by,

$$B_{\text{eff}} = \sqrt{B_1^2 + \frac{\Omega^2}{\gamma}} \quad (1.11)$$

If the offset frequency Ω is tuned to zero, B_{eff} is equal to B_1 , perpendicular to \vec{B}_0 and it is static in the rotating frame. This situation is called on-resonance.

RF pulses

RF pulses are used in NMR for quantitatively perturbing spin ensembles. If we apply a RF pulse on-resonance ($\Omega = 0$) in a coil surrounding the sample, the torque created on the spins by the B_1 field forces the spins to rotate by a flip angle (or rotating angle) of θ , which is given by,

$$\theta = -\gamma \cdot B_1 \cdot \tau_P \quad (1.12)$$

where τ_P refers to the RF pulse length and the negative sign in the front reflects the counter-clockwise rotation direction. By increasing the pulse length τ_P , the flip angle will increase linearly. The detectable NMR signal corresponds to the magnetization in the XY plane, which is given by (see figure 1.2),

$$M_{XY} = M_0 \sin\theta \quad (1.13)$$

Therefore, the NMR signal is maximized when $\theta = 90^\circ + n\pi$ and minimized when $\theta = n\pi$ (n is an integer). As 90° and 180° pulses are essential in NMR experiments, it is necessary to calibrate the pulses before each experiment.

Free induction decay (FID) and Fourier transformed NMR

RF coils only detect the magnetization of spin ensembles evolving in the transverse plane. After the application of a RF pulse, the detectable NMR signal in the transverse plane oscillates around \vec{B}_0 with a frequency of Ω and decreases to zero after a time characterized by a time constant T_2^* due to the transverse relaxation processes. This phenomenological oscillation is called free induction decay (FID).

The FID acquired from the spin system in the time domain following a RF pulse is usually complex and composed by several different single decays. To separate all the components from the FID, a Fourier transformation is applied to the temporal signal $f(t)$:

$$F(\omega) = \int_{-\text{inf}}^{\text{inf}} f(t) \exp(-i\omega t) dt \quad (1.14)$$

with

$$F(\omega) = Re(F(\omega)) + Im(F(\omega)) \quad (1.15)$$

$$Re(F(\omega)) = \int_{-\infty}^{\infty} f(t) \cos(-i\omega t) dt \quad (1.16)$$

$$Im(F(\omega)) = \int_{-\infty}^{\infty} f(t) \sin(-i\omega t) dt \quad (1.17)$$

In practice, both real and imaginary parts are measured using a quadrature phase detector. The line width of the Fourier-transformed signal at half maximum (FWHM) is representative of the field inhomogeneity and is related to T_2^* by $FWHM = \frac{1}{\pi T_2^*}$. It is important to note that the acquired signal does not cover all the frequencies since the applied RF pulse has a finite length τ_P in the time domain only covers a spectrum width of $\Delta = \frac{1}{2\tau_P}$.

Chemical shift

The chemical shift is defined as the relative frequency offset of the detected NMR signal from a given reference. It depends on the chemical structure of the molecules in which the nuclear spins of interest are located and is given by,

$$\delta = \frac{\omega - \omega_0}{\omega_0} \cdot 10^6 ppm \quad (1.18)$$

For 1H and ^{13}C , TMS (tetramethylsilane) is used as the zero reference. As we can see from equation 1.18, the chemical shift is a relative value and it is independent of the magnetic field \vec{B}_0 , but the higher the magnetic field the larger the spectral resolution. This frequency shift is caused by the local magnetic field generated by the electron clouds orbiting around the nuclear spins. Chemical shift are used in NMR spectroscopy for analyzing chemical compositions.

1.2.1 Bloch equation and relaxation processes

After applying a RF pulse to disturb the spin ensemble, the system relaxes back to its thermal equilibrium state with a nuclear magnetization along the Z direction. This evolution can be semi-classically described in the rotating frame by the Bloch equations¹ as following,

$$\frac{d}{dt} \vec{M}(t) = \gamma \cdot \vec{M}(t) \times \vec{B}(t) + R(\vec{M}(t) - \vec{M}_0), \quad (1.19)$$

where the magnetic field vector $\vec{B}(t) = (\vec{B}_1 \cos(\omega_0 t), \vec{B}_1 \sin(\omega_0 t), \vec{B}_0)$ and the relaxation matrix $R = (1/T_2, 0, 0; 0, 1/T_2, 0; 0, 0, 1/T_1)$. T_1 and T_2 are the longitudinal and transversal relaxation

time, respectively. Solving all three time-dependent differential Bloch equations gives,

$$\begin{aligned} M_Z(t) &= M_0(1 - e^{-t/T_1}) + M_Z(t_0)e^{-t/T_1} \\ M_{X,Y}(t) &= M_{X,Y}(t_0)e^{-t/T_2} \end{aligned} \quad (1.20)$$

where $M_{X,Y}$ and M_Z represent the transverse and longitudinal magnetization, respectively. From equations 1.20, we see that the longitudinal relaxation time corresponds to the time constant needed by the spin ensemble to recover its thermal equilibrium magnetization and that the transverse relaxation time is the time constant relative to the dephasing of the magnetization in the XY plane. As $M_{XY}(t)$ or $M_Z(t)$ can be measured by NMR, the solution of the Bloch equations is used for determining T_1 and T_2 . In this work we mainly focused on T_1 measurements and various methods for determining T_1 are presented in section 1.5.

NMR relaxation mechanisms were first explained by the BPP (Bloemberg Purcell Pound) theory² by considering the motion and rotation of the spins influenced by the environment. Longitudinal relaxation, also called spin-lattice relaxation, is mainly caused by the vibration and rotation of the local magnetic field of the environment (lattice) of the nuclear spins. T_1 relaxation describes the tendency of the spins to reorient themselves with the applied static magnetic field \vec{B}_0 .

Transverse relaxation indicates the loss of coherence in the transverse plane within the spin ensemble caused by the spin-spin interactions. These spin-spin interactions influence the precession speed of the spins around \vec{B}_0 and thus lead to a dephasing of the initial coherent motion of the spins to finally cancel the net magnetization $M_{X,Y}$ in the XY plane. T_2 is usually much shorter than T_1 .

To understand the concepts behind both relaxation processes and to evaluate the influence of molecular motion at a certain frequency ω in the local magnetic field, a fluctuation spectral density function $J(\omega)$ is usually introduced in the form of,

$$J(\omega) = \frac{\tau_c}{1 + \omega^2\tau_c^2} \quad (1.21)$$

where τ_c is the correlation time related to the random motions. For a homonuclear spin system with $I = 1/2$, the two relaxation times can be described as,

$$\begin{aligned} \frac{1}{T_1} &= K[J(\omega_0) + 4J(2\omega_0)] \\ \frac{1}{T_2} &= \frac{K}{2}[3J(0) + 5J(\omega_0) + 2J(2\omega_0)] \end{aligned} \quad (1.22)$$

where K , which represents a constant related to the spin species and the average distance r

between two spins, is given by,

$$K = \left(\frac{\mu_0}{4\pi}\right)^2 \cdot \frac{3}{10} \cdot \frac{\hbar^2 \gamma^4}{r^6}. \quad (1.23)$$

From equations 1.22, several situations can be considered:

- a) When the correlation time is extremely short such as to have the condition $\omega_0^2 \tau_c^2 \ll 1$, T_2 tends to be the same as T_1 ;
- b) When the correlation time is long enough such as to have the condition $\omega_0^2 \tau_c^2 \gg 1$, T_2 tends to be much shorter than T_1 ;
- c) Between these two extreme cases, there is a range of τ_c values for which, T_1 reaches a minimum, but T_2 continuously decreases with increasing τ_c because of the $J(0)$ term.

The main sources of relaxation are paramagnetic species, dipolar interaction, and chemical shift anisotropy. More detailed descriptions of these mechanisms can be found in many references²⁻⁴.

1.3 Dynamic Nuclear Polarization (DNP)

The intensity of the NMR signal is directly dependent on the nuclear polarization which varies with the magnetic field and temperature (see equation 1.9). Since this polarization is on the order of 10^{-5} at room temperature (see section 1.1.2), a large number of spins are required to have a substantial NMR signal. To overcome this drawback, important technical improvements were achieved to increase the magnetic field of the superconducting magnet and sensitivity of the RF coils. Hyperpolarization techniques have been developed to improve NMR sensitivity. The idea is to create an out of equilibrium nuclear spin polarization that is far beyond the thermal equilibrium polarization. One of the hyperpolarization methods proposed so far is DNP. Continuous microwave irradiation is applied to saturate the polarization of the unpaired electrons of paramagnetic impurities embedded in a sample containing the nuclear spins of interest. Through dipolar-dipolar hyperfine interactions the polarization can be transferred from the electron spins to the nuclear spins. The MR sensitivity of nuclear spins can thus be significantly enhanced. This section starts with a description of several fundamental spin transition processes that play an important role in DNP. After the introduction of spin temperature, three important DNP mechanisms, the Overhauser effect, the solid effect and the thermal mixing, will be discussed. Finally, some other hyperpolarization methods will be briefly introduced.

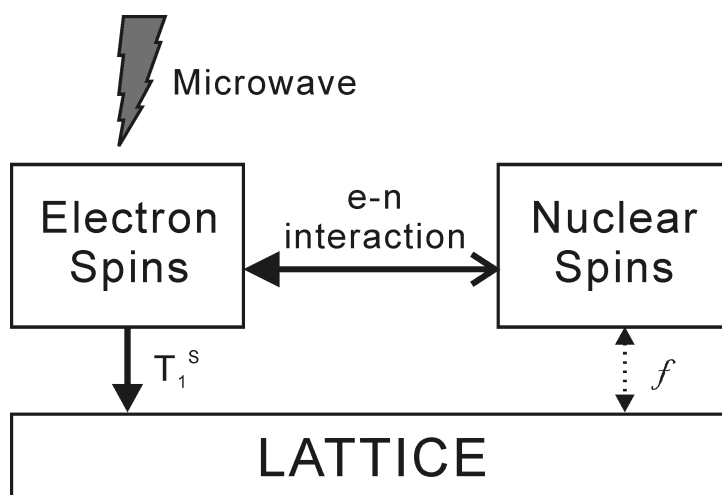


Figure 1.3: Global mechanism of DNP: Microwave source saturates the ESR transition at certain frequency and then polarization is transferred through flip-flop electron-nuclear spin transition from electron spin to nuclear spin. Besides fast relaxation process of electron spin which helps electron spin quickly back to the thermal equilibrium makes the polarization process more efficiently.

1.3.1 Global mechanism of DNP

The general mechanism of DNP is depicted in figure 1.3. To polarize the nuclear spins efficiently, the electron spin transition is saturated by microwave irradiation at a specific frequency ω which is around the Larmor frequency of the electron spins ω_e . The electron spin population of both energy levels becomes identical and the electron spins are forced to make electron-nuclear spin flip-flop transitions. The exchange of energy between the electron and the nuclear spins through electron-nuclear interactions typically involves one nuclear spin and one or more electron spins.

It is of the uttermost importance to note that the electron spins can on one hand help polarize the nuclear spins but on the other hand are paramagnetic centers inducing the relaxation of the nuclear spins back to thermal equilibrium. It is thus necessary for the polarized nuclear spins to be rather well isolated from the electron spins, at least for the major part of the time of the DNP experiment. For this reason, it is necessary to carefully choose the ratio between nuclear spin and electron spin density. These densities also depend on the ratio between the nuclear and electron spin longitudinal relaxations, a ratio which is highly influenced by the applied magnetic field \vec{B}_0 and the temperature of the sample. As a rule of thumb, A. Abragam and M. Goldman stated that to effectively enhance the nuclear polarization of solid dielectric samples via DNP the following condition should be fulfilled¹⁵:

$$(N_I T_{1,e}) / (N_S T_{1,n}) \ll 1 \quad (1.24)$$

where N_I and N_S are respectively the number of nuclear and electron spins in the sample.

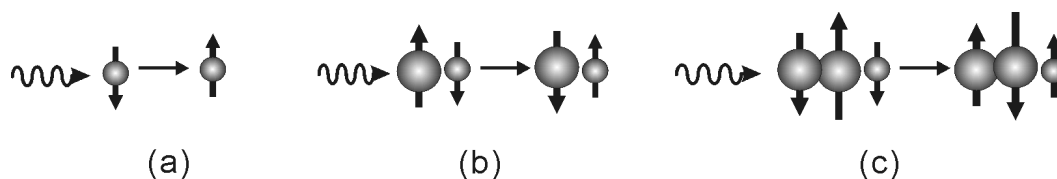


Figure 1.4: (a) One-spin system consisting of an electron spin; (b) Flip-flop process in a two-spin system composed of one electron spin (large) and nuclear spin (small); (c) Flip-flop process in a three-spin system consisting of two electron spins (large) with different Zeeman energy and one nuclear spin (small).

In the liquid-state (as well as in metals), the DNP process involves moving electrons and the interaction, which will involve only one nuclear spin and one electron spin, is only effective during a very short "contact" time between the moving electrons and the nuclear spins. In dielectric solids, spin diffusion (via nuclear spin-nuclear spin dipolar interactions) will lead to the polarization of remote nuclear spins (the nuclear spins in close contact with the electron spins will experience a large number of flip-flop transitions and will effectively not be polarized). The spin diffusion mechanism involves both dipolar spin diffusion and Zeeman spin diffusion. Reports have shown that dipolar spin diffusion is much faster than Zeeman spin diffusion^{5,6}. This suggests that cooling the dipolar reservoir efficiently can accelerate the spin diffusion process and thus reduce the polarization time.

Fundamental spin transitions in DNP

The spin transitions involving both electron spins and nuclear spins are the essential processes leading to the transfer of polarization in DNP. The fundamental transitions can be visualized using a simplified pictorial representations involving one, two or three spins and electromagnetic perturbation.

One-spin systems. The simplest spin system is composed of one electron spin or one nuclear spin, and therefore represents the standard electron spin or nuclear spin resonance transitions.

In the case of an electron spin, the absorption of microwave tuned to the electron resonance frequency can either pump the electron spin from the lower energy state (spin up) to the higher energy state (spin down), or stimulate the electron spin from the higher energy state down to the lower energy state with emission of one (or more) phonon with the same energy. The transition probability is identical for both processes. If the irradiation power is large enough, the population of both energy levels will equalize and thus the electron spin polarization become zero.

Two-spins systems. Three different types of two-spin systems associated with three types of transitions are involved in DNP: homonuclear transitions, electron-nuclear transitions and electron-electron transitions.

Homonuclear transitions are at the origin of T_2 relaxation and spin diffusion mechanisms. Two nuclear spins with different orientation simultaneously change their orientation due to dipolar-dipolar interaction. Extending this process to a multiple homonuclear spins system, the polarization of a local spin ensemble can therefore "diffuse" to surrounding spins in the solid sample.

When both electron spins have the same transition energy, electron-electron transitions are allowed due to the energy and angular momentum conservation. This type of transition is depicted in figure 1.4: one of the two electron spins flips (or flops) and the emitted energy will be absorbed by the other electron spin to complete the flopping (or flipping) process. These flip-flop transitions are at the origin of electron T_2 relaxation.

Due to the large difference in Zeeman energy, the electron-nuclear transitions involving one electron spin and one nuclear spin are forbidden transitions. With the involvement of microwaves, the nuclear spin can flip (or flop) simultaneously when the electron spin flops (or flips). Thanks to the hyperfine interaction between electron and nuclear spins, Zeeman energy can thus flow from the nuclear spins system to the electron spins system and vice-versa. Two-spin electron-nuclear transition are at the origin of the Overhauser and the solid effects, which will be discussed in details in following sections.

Three spin system. The transitions involving three-spin systems compose of two electron spins with different Zeeman energy and one nuclear spin are the fundamental transitions leading to the thermal mixing and the cross effect. A flip-flop transition of both electron spins can induce a flip (or a flop) of the nuclear spin. This process is possible when the ESR linewidth is larger than the nuclear resonance frequency, so that flip-flop transition between two electron spins with a Zeeman energy difference equal to a nuclear resonance frequency can take place. As cross effect ($\omega_{e1} - \omega_{e2} = \omega_n$) can be described as a particular case of thermal mixing, only thermal mixing will be discussed in the following.

1.3.2 Spin temperature

To understand the DNP processes, it is useful to introduce the concept of the spin temperature T_S . Each nuclear spin population distribution is linked to a temperature through the Boltzmann distribution as described in equation 1.7 since the nuclear spin system is relatively well isolated from the lattice in the dielectric solids of interest for DNP (long $T_{1,n}$), it is possible to create a nuclear spin population distribution that is far from thermal equilibrium with the sample (lattice) temperature T_L . This population distribution can nevertheless be associated with a temperature called spin temperature T_S which is different from T_L and is defined as,

$$\frac{N_{\uparrow}}{N_{\downarrow}} = e^{-\frac{\hbar\omega_0}{kT_S}} \quad (1.25)$$

$$= e^{-\beta\omega_0} \quad (1.26)$$

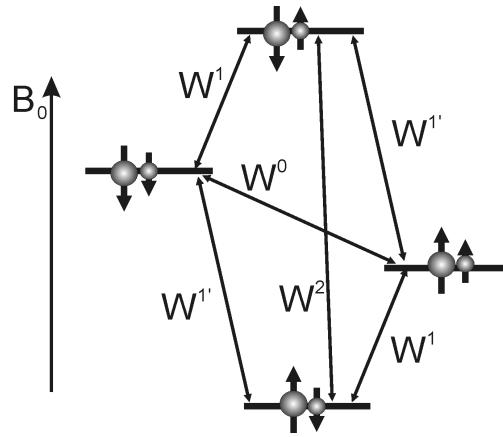


Figure 1.5: (Schematics of the energy levels and transitions of a two-spin system consisting of a nuclear spin and a electron spin: W^0 and W^2 are the relaxation rates for zero quantum and double quantum transitions, respectively; W^1 represents the NMR relaxation rate and $W^{1'}$ the ESR relaxation rate.

where

$$\beta = \frac{\hbar}{kT_S}. \quad (1.27)$$

β is the so-called inversed temperature. At thermal equilibrium, $T_S = T_L$. From equation 1.26 it is easy to link the nuclear spin polarization to the spin temperature which gives with high temperature approximation,

$$P = \frac{1}{2} \beta \omega_0 \quad (1.28)$$

A positive polarization is characterized by a positive spin temperature whereas a negative polarization will give a negative spin temperature.

1.3.3 Overhauser Effect

A.W. Overhauser was the first one to predict that nuclear spins can be polarized by the electron spins⁷. It was shown experimentally that not only metals⁸, but also insulators doped with paramagnetic impurities⁹ can be polarized by DNP. It is based on the spin flip-flop transitions in two-spin systems consisting of one electron spin and one nuclear spin. A microwave irradiation is applied at the frequency of the electron spin resonance in order to saturate the ESR transitions (see figure 1.5). During the electron spin relaxation the nuclear spins will be polarized through hyperfine coupling.

By solving the rate equations established by Solomon³, the enhancement of the Over-

hauser effect can be written as,

$$\epsilon = 1 - \xi s f \frac{|\gamma_S|}{\gamma_I}, \quad (1.29)$$

where the electron spin saturation level (saturation parameter s), the microwave power (coupling factor ξ) and the paramagnetic relaxation time (leakage factor f) are introduced. The coupling factor ξ is given by,

$$\xi = \frac{W^2 - W^0}{W^0 + W^2 - 2W^1}. \quad (1.30)$$

The coupling factor can take the value from -1, in the case of a pure scalar interaction, to 0.5, in the case of a pure dipolar interaction. The saturation parameter s represents the degree of saturation of the electron spins and can be expressed in term of the magnetization along the Z axis,

$$s = \frac{M_0 - \langle M_z \rangle}{M_0}. \quad (1.31)$$

It is clear that in the case of full saturation $s = 1$, and that without microwave $s = 0$. The leakage factor f represents the fraction of nuclear polarization that is lost because of the presence of the electron spins and is described as,

$$f = \frac{W^2 + W^0 + 2W^1}{W^0 + W^2 + 2W^1 + w^{1'}} = 1 - \frac{T_{1n}^{+S}}{T_{1n}^{-S}}, \quad (1.32)$$

where T_{1n}^{-S} is the nuclear relaxation time without any electron spins, and T_{1n}^{+S} is the nuclear relaxation time with electron spins. If s and f are equal to unity and $\xi = -1$, we can see that the enhancement factor from the Overhauser effect is proportional to the gyromagnetic ratio between the electron spin and nuclear spin. This means that the maximal theoretical enhancement factor is ≈ 660 for ^1H and ≈ 2630 for ^{13}C .

1.3.4 Solid Effect

Similarly to the Overhauser effect, the solid effect is also based on the spin transitions between one electron spin and one nuclear spin. However, unlike the Overhauser effect, the spin transitions take place at the same time as the microwave irradiation. The microwave frequency should be equal to the relative difference between the electron resonance frequency and the nuclear resonance frequency or the sum of both frequencies, i.e. $(\omega_e \pm \omega_n)$. The offset from the electron spin resonance frequency forces the simultaneous transition of the electron spin and the nuclear spin either as a flip-flop transition (zero quantum transition) or a flip-flip transition (double quantum transition). We refer to the polarization at frequency of $(\omega_e + \omega_n)$ as negative DNP and the polarization at frequency of $(\omega_e - \omega_n)$ as positive DNP.

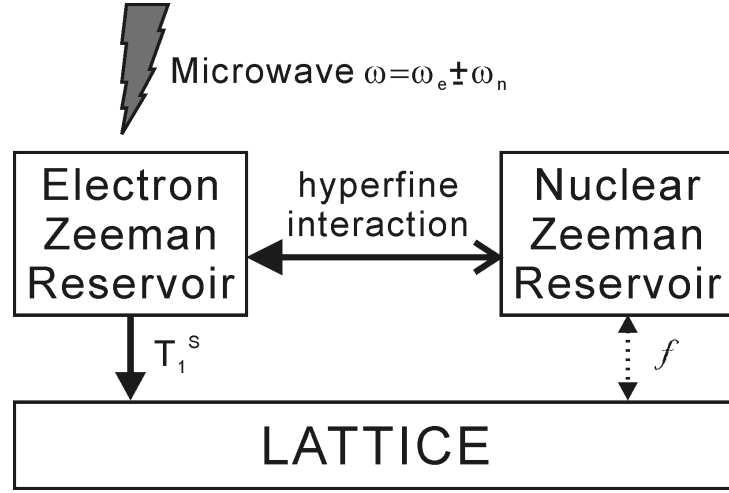


Figure 1.6: Heat flow chart describing the solid effect: the nuclear spin temperature is lowered through the electron Zeeman reservoir by electron-nuclear spin flip-flop (or flip-flip) process.

The Hamiltonian of the solid effect can be written as,

$$H = -\omega_e S_Z - \omega_n I_Z + 2\omega_{1e} S_x \cos \omega t + \mathbf{S} \times \mathbf{A} \times \mathbf{I} \quad (1.33)$$

The first and second terms of the equation are the Zeeman terms. The third term is the microwave irradiation term and the last term is the hyperfine interaction term with \mathbf{A} , the hyperfine interaction tensor. By using perturbation theory, the transition rate of flip-flop or flip-flip can be obtained as¹¹,

$$W^+ = 2\pi \frac{\omega_{1e}^2 \left| \frac{1}{4} A_{z+} \right|}{\omega_{0n}^2} \delta(\omega_{0e} + \omega_{0n} - \omega) W^- = 2\pi \frac{\omega_{1e}^2 \left| \frac{1}{4} A_{z+} \right|}{\omega_{0n}^2} \delta(\omega_{0e} - \omega_{0n} - \omega) \quad (1.34)$$

where operator $A_{z+} = A_{zx} + iA_{zy}$. δ -function indicates that the transition is maximized when the microwave frequency ω fits the condition $\omega = \omega_{0e} \pm \omega_{0n}$. For the zero quantum transition ($\omega = \omega_{0S} + \omega_{0I}$), the rate equations for all possible transitions can be summarized as,

$$\frac{\partial \rho_+^S \rho_-^I}{\partial t} = -W^+ (\rho_+^S \rho_-^I - \rho_-^S \rho_+^I) \quad (1.35)$$

$$\frac{\partial \rho_+^S \rho_+^I}{\partial t} = 0 \quad (1.36)$$

$$\frac{\partial \rho_-^S \rho_-^I}{\partial t} = 0 \quad (1.37)$$

$$\frac{\partial \rho_-^S \rho_+^I}{\partial t} = W^+ (\rho_+^S \rho_-^I - \rho_-^S \rho_+^I) \quad (1.38)$$

where $\rho_{\pm}^S \rho_{\pm}^I$ represents the probability of the corresponding spin state. Then by recombining

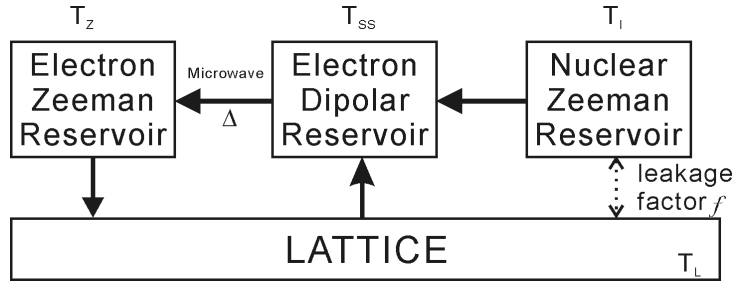


Figure 1.7: Heat flow chart describing the thermal mixing: the electron dipolar reservoir is cooled by the electron Zeeman reservoir using off-resonance irradiation. Thermal contact between the electron dipolar reservoir and the nuclear Zeeman reservoir lowers the nuclear spin temperature.

the equations as well as by using the definition of electron spin and nuclear spin polarization, we can get,

$$\frac{\partial}{\partial t}(P_S + P_I) = -2W^+(P_S + P_I) \quad (1.39)$$

$$\frac{\partial}{\partial t}(P_S - P_I) = 0 \quad (1.40)$$

The solution of above equations shows that the nuclear spin polarization P_I exponentially grows towards the negative electron spin polarization $-P_S$ with a time constant of $(2W^+)^{-1}$. In the case of double quantum transition ($\omega = \omega_{0S} - \omega_{0I}$), the nuclear polarization exponentially grows towards $+P_S$ with a time constant of $(2W^-)^{-1}$.

1.3.5 Thermal mixing

Thermal mixing can be described using the three-spin systems introduced in section 1.3.1. Compared to the solid effect, the electron spin concentration in samples experiencing thermal mixing is larger and the dipolar interactions are thus non-negligible. Due to the local magnetic field B_I caused by the electron spins dipolar field, the width of the electron Zeeman energy levels becomes non-negligible. In other words, there is a high probability that there exists two electron spins ensembles with a difference in Zeeman energy that matches the Zeeman energy of surrounding nuclear spins.

For understanding thermal mixing it is necessary to use the spin temperature formalism and to define several thermal reservoirs: the Electron Zeeman Reservoir (EZR), the Electron Dipolar Reservoir (EDR) and the Nuclear Zeeman reservoir (NZR) shown in figure 1.7. EZR or NZR include the Zeeman energy of the electron or nuclear spins ensembles, respectively and EDR includes the dipolar energy of the electron spins ensemble. Each reservoir has its own spin temperature, T_Z for EZR, T_{SS} for EDR and T_I for NZR. At thermal equilibrium $T_Z = T_{SS} = T_L$ means that all spin temperatures are equal to the lattice temperature.

Thermal mixing can be understood as a two-step process, namely dynamic cooling and thermal mixing¹³⁻¹⁵. The dynamic cooling process consists in lowering the spin temperature of EDR, T_{SS} . The final spin temperature can be estimated from the intensity of the local magnetic field B_l as,

$$T_f \cong \frac{B_l}{B_i} T_i \quad (1.41)$$

where B_i , T_i represents the initial magnetic field and temperature of the system.

Through continuous RF irradiation with an off-resonance frequency ω , the effective local magnetic field B_{eff} is reduced by a factor,

$$\frac{B_{eff}}{B_0} = \frac{\omega_0 - \omega}{\omega_0} = \frac{\Delta}{\omega_0}. \quad (1.42)$$

Depending on the resonance offset, $\Delta = \omega_0 - \omega$, the spin temperature can be either positive or negative. The Zeeman spin temperature under microwave irradiation, T'_Z , is reduced by the same factor and is given by,

$$T'_Z = \frac{\Delta}{\omega_0} T_L. \quad (1.43)$$

In this case, electron Zeeman energy at local magnetic field is lowered and comparable to the transition energy needed for dipolar interaction so that energy exchange between EZR and EDR is possible.

The thermal mixing process consists in lowering the NZR spin temperature through thermal contact with the EDR. This contact is inherent to the spin system and depends on the radical concentration. The leakage factor f represents the direct relaxation from NZR to lattice.

1.4 Other hyperpolarization methods

1.4.1 Spin-Exchange Optical Pumping(SEOP)

The spin-exchange optical pumping method is based on the transfer of the angular momentum of polarized optical electromagnetic waves to polarize the valence electron shell of alkali metal atoms. The nuclear spin polarization of noble gases can be enhanced through the collisions (dipolar interactions) between the polarized alkali vapors and the nuclear spins of the surrounding noble gas atom. Almost all alkali atoms can be used for SEOP due to their single free valence electron, but Rubidium is usually used. To increase the probability of collision and therefore the nuclear spin polarization, the pressure of the noble gas is maintained at a level of several bars and the temperature of the polarizing cell is set up to be high enough to create saturated rubidium atom vapor. The typical achievable polarization

level by SEOP is five orders of magnitude, up to 70%^{16;17}.

Most biomedical applications of SEOP have been focused on lungs^{18;19} since nuclear spins of noble gas, i.e. ^3He and ^{129}Xe , have several advantages for MR detection: first, noble gases can enter the lung without any harm to the biological tissues; second, the relaxation time of noble gas is relative long, around several hundreds of seconds^{20;21}; third, they give the best contrast for MR imaging due to their zero biological natural abundance.

To explore the potential of hyperpolarized gas for other organs, the relatively high solubility of Xe gas in the blood plays an important role^{22;23}. Hyperpolarized ^{129}Xe was used to measure diffusion and perfusion in different tissues in both human and rodents²⁴⁻²⁶ after intravenous injection. Recently, more progresses in pharmaceutical field allowed the design of different carriers of hyperpolarized ^{129}Xe ²⁷⁻³⁰ which targets specific diseased tissues and thus broadens the application range of hyperpolarized gas in molecular imaging field.

1.4.2 ParaHydrogen Induced Polarization(PHIP)

Hydrogen is a very interesting element for MR technique since it is a spin-1/2 element and possesses the largest gyromagnetic ratio among nuclear spins. Moreover it can be thermally forced into its singlet spin state, the so-called parahydrogen state. Its other state is the orthohydrogen which has a total spin of 1 and an energy degeneracy of 3^{31;32}. Transitions between ortho- and para- hydrogen are normally forbidden due to the state symmetry. To increase the population of the parahydrogen, one can pump the hydrogen gas simply through a catalyst at very low temperature ($\sim 20\text{K}$)³³.

A specific PHIP method, called Parahydrogen And Synthesis Allow Dramatically Enhanced Nuclear Alignment (PASADENA), is based on the hydrogenation reactions of parahydrogen with substrates containing a particular type of carbon double bond³⁴. The two protons of parahydrogen will be separated and attached to both side of the double bond. The hydrogenation reactions used for PASADENA method are usually carried out at high magnetic field where the magnetic symmetry of parahydrogen is broken while a spin-spin coupling between them remains. Several applications for MR metabolic studies and imaging have already been reported. $[1-^{13}\text{C}]$ diethyl-succinate was polarized to a level of 17% *in vitro*³⁵ and used for *in vivo* imaging³⁶.

Another PHIP method, called SABRE, is based on the fast magnetization transfer from parahydrogen to a substrate without hydrogenation process³⁷. It has been reported that substrates labeled with ^{13}C can be polarized by SABRE³⁸.

PHIP is an interesting method to increase the MR sensitivity since it is much faster than DNP to prepare highly polarized substrates. It has been used to study catalytic chemistry, drug developments and has a great potential for biomedical applications.

1.5 Methods to determine the longitudinal relaxation time T_1

Several methods can be used to determine the longitudinal relaxation time T_1 in solid-state or liquid-state sample. The standard methods are based on magnetization recovery schemes that are widely used in high resolution NMR spectroscopy and *in vivo* MRI T_1 mapping. The T_1 of DNP-enhanced solid samples and hyperpolarized nuclei can be determined using a polarization decay scheme. For instance, *in vitro* DNP experiments can be performed to study the influence of the external conditions on the liquid-state ^{13}C T_1 of biomolecules of interest.

1.5.1 Magnetization recovery schemes

The longitudinal relaxation time T_1 is a time constant which characterizes the exponential recovery of the spin magnetization along the direction of the applied static magnetic field. To measure T_1 the Z-magnetization must be forced out of equilibrium using a preparation pulse (or series of pulses) in the XY plane. The evolution of the magnetization back to thermal equilibrium can be followed by applying a $\pi/2$ pulse in the XY plane at different time intervals following the preparation pulse (or series of pulses). Here we present the two most common magnetization recovery schemes used to measure T_1 .

Inversion recovery scheme

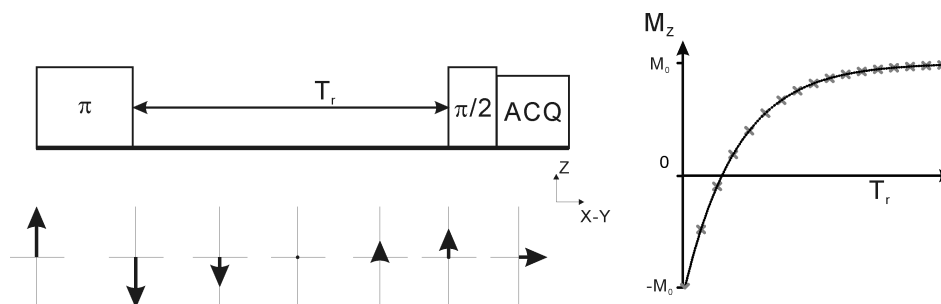


Figure 1.8: Inversion recovery pulses sequence along with a sketch of the evolution of the magnetization (left) as well as the magnetization recovery along the Z direction (right).

The preparation pulse is a π pulse which inverts the Z-magnetization from $+M_0$ to $-M_0$. The longitudinal relaxation process leads to the magnetization recovery back to $+M_0$, the thermal equilibrium position. After a recovering time T_r following the preparation pulse, the recovered magnetization will be flipped into the XY plane and measured immediately afterwards (shown in figure 1.8).

The evolution of the magnetization observed using the inversion recovery scheme can be calculated by using the solution of the Bloch equation in the Z-direction described in section 1.3. After imposing the initial and final conditions for the Z-magnetization, $M(0) = M_z(T_r = 0) = -M_0$ and $M(\infty) = M_z(T_r = \infty) = M_0$, the recovered magnetization M_{IR} can be described

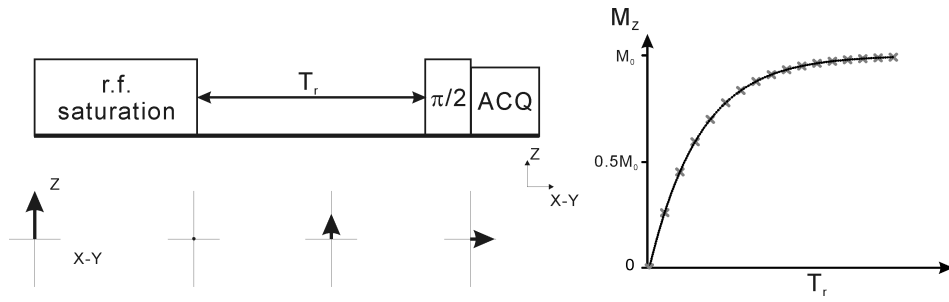


Figure 1.9: Saturation recovery pulses sequence along with a sketch of the evolution of the magnetization (left) as well as the magnetization recovery along the Z direction(right).

as,

$$M_{IR} = M_0 \cdot (1 - 2e^{-T_r/T_1}) \quad (1.44)$$

A series of measurements with different T_r values within the range $[0, 5T_1]$ are necessary to extract T_1 .

Saturation recovery scheme

In the saturation recovery scheme, the magnetization is saturated by a long RF pulse or a series of short pulses replacing the π pulse used as preparation pulse in the inversion recovery scheme. The series of pulses aim at dephasing the magnetization in the X,Y, and Z directions so that the final net magnetization of the sample is equal to zero. The measurements following the recovery time T_r are done exactly the same way as in the inversion recovery scheme. The signal intensity of the saturation recovery scheme can be theoretically deduced from Bloch equation with the initial conditions of $M(0) = M_z(T_r = 0) = 0$ and $M(\infty) = M_z(T_r = \infty) = M_0$ and is described as,

$$M_{SR} = M_0(1 - e^{-T_r/T_1}) \quad (1.45)$$

The advantage of the saturation recovery scheme compared to the inversion recovery scheme is that the total measuring time is shorter since the sequence can be repeated just after the acquisition whereas in the inversion recovery sequence cannot be repeated until the magnetization has fully recovered (typically $5T_1$). The drawback of the saturation recovery scheme lies in the resolution of the recovery curve as the magnetization recovers from $-M$ to $+M$ in the inversion recovery scheme and only from 0 to $+M$ in saturation recovery scheme.

1.5.2 Polarization decay scheme

The magnetization of DNP-enhanced spins is much larger than their thermal equilibrium magnetization. Since hyperpolarized spins are in an out of equilibrium state, they relax

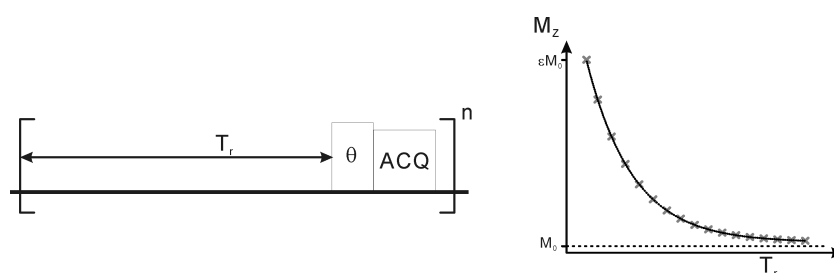


Figure 1.10: Polarization measurements with small flip angle α (left) as well as the magnetization recovery along the Z direction (right) back to thermal equilibrium M_0 .

towards their thermal equilibrium with a time constant corresponding to T_1 . To determine the relaxation time small flip angle RF pulses are used to measure the magnetization every TR which can thus be written as,

$$M = M_0^P (e^{-T_r/T_1}) \cdot \sin\theta, \quad (1.46)$$

where M_0^P represents the initial DNP-enhanced magnetization. Let us assume that the initial enhancement of liquid-state pyruvate following dissolution DNP is 16500 (13% polarization level) and that the longitudinal relaxation time T_1 is around 50 s. It will take around 490 s for the polarization to return back to thermal equilibrium according to the equation 1.46. In practice the measurement time for this experiment is less than 490 s due to the polarization loss from the RF pulses and the sensitivity limit of the spectrometer associated with the typically low concentration of hyperpolarized substrates. By applying a series of small flip angle RF pulses with the same repetition time TR , the T_1 can be determined in one measurement. To obtain the correct T_1 value, it is necessary to correct for the effect of the RF pulses. The unperturbed magnetization can be recalculated from,

$$M'(n \cdot TR) = M(n \cdot TR) / (\cos\theta)^{n-1}. \quad (1.47)$$

References

- [1] F. Bloch, W. W. Hansen, and M. Packard. Nuclear induction. *Physical Review*, 69(3-4):127–127, 1946.
- [2] N. Bloembergen, E. M. Purcell, and R. V. Pound. Relaxation effects in nuclear magnetic resonance absorption. *Physical Review*, 73(7):679–712, 1948.
- [3] I. Solomon. Relaxation processes in a system of 2 spins. *Physical Review*, 99(2):559–565, 1955.
- [4] L. Helm. Relaxivity in paramagnetic systems: Theory and mechanisms. *Progress in Nuclear Magnetic Resonance Spectroscopy*, 49(1):45–64, 2006.
- [5] W. Zhang and D. G. Cory. First direct measurement of the spin diffusion rate in a homogenous solid. *Physical Review Letters*, 80(6):1324–1327, 1998.

Chapter 1. Basics about NMR and DNP

- [6] G. S. Boutis, D. Greenbaum, H. Cho, D. G. Cory, and C. Ramanathan. Spin diffusion of correlated two-spin states in a dielectric crystal. *Physical Review Letters*, 92(13), 2004.
- [7] A. W. Overhauser. Polarization of nuclei in metals. *Physical Review*, 91(2):476–476, 1953.
- [8] T. R. Carver and C. P. Slichter. Polarization of nuclear spins in metals. *Physical Review*, 92(1):212–213, 1953.
- [9] A. Abragam. Overhauser effect in nonmetals. *Physical Review*, 98(6):1729–1735, 1955.
- [10] K. H. Hausser and D. Stehlik. Dynamic nuclear polarization in liquids. *Adv. Magn. Reson.*, 3:79–139, 1968.
- [11] W. T. Wenckebach. Dynamic nuclear polarization using strong microwave fields, 2012.
- [12] W. T. Wenckebach. The solid effect. *Applied Magnetic Resonance*, 34(3-4):227–235, 2008.
- [13] S. T. Goertz. The dynamic nuclear polarization process. *Nuclear Instruments & Methods in Physics Research Section a-Accelerators Spectrometers Detectors and Associated Equipment*, 526(1-2):28–42, 2004.
- [14] M. Goldman. Overview of spin temperature, thermal mixing and dynamic nuclear polarization. *Applied Magnetic Resonance*, 34(3-4):219–226, 2008.
- [15] A. Abragam and M. Goldman. Principles of dynamic nuclear-polarization. *Reports on Progress in Physics*, 41(3):395–467, 1978.
- [16] M. S. Albert, G. D. Cates, B. Driehuys, W. Happer, B. Saam, C. S. Springer, and A. Wishnia. Biological magnetic-resonance-imaging using laser polarized xe-129. *Nature*, 370(6486):199–201, 1994.
- [17] H. Middleton, R. D. Black, B. Saam, G. D. Cates, G. P. Cofer, R. Guenther, W. Happer, L. W. Hedlund, G. A. Johnson, K. Juvan, and J. Swartz. Mr-imaging with hyperpolarized he-3 gas. *Magnetic Resonance in Medicine*, 33(2):271–275, 1995.
- [18] X. J. Chen, H. E. Moller, M. S. Chawla, G. P. Cofer, B. Driehuys, L. W. Hedlund, and G. A. Johnson. Spatially resolved measurements of hyperpolarized gas properties in the lung in vivo. part i: diffusion coefficient. *Magn Reson Med*, 42(4):721–8, 1999.
- [19] X. J. Chen, H. E. Moller, M. S. Chawla, G. P. Cofer, B. Driehuys, L. W. Hedlund, J. R. MacFall, and G. A. Johnson. Spatially resolved measurements of hyperpolarized gas properties in the lung in vivo. part ii: T*(2). *Magn Reson Med*, 42(4):729–37, 1999.
- [20] A. K. Venkatesh, L. Zhao, D. Balamore, F. A. Jolesz, and M. S. Albert. Evaluation of carrier agents for hyperpolarized xenon mri. *Nmr in Biomedicine*, 13(4):245–52, 2000.
- [21] A. Bifone, Y. Q. Song, R. Seydoux, R. E. Taylor, B. M. Goodson, T. Pietrass, T. F. Budinger, G. Navon, and A. Pines. Nmr of laser-polarized xenon in human blood. *Proc Natl Acad Sci U S A*, 93(23):12932–6, 1996.
- [22] B. M. Goodson, Y. Song, R. E. Taylor, V. D. Schepkin, K. M. Brennan, G. C. Chingas, T. F. Budinger, G. Navon, and A. Pines. In vivo nmr and mri using injection delivery of laser-polarized xenon. *Proc Natl Acad Sci U S A*, 94(26):14725–9, 1997.
- [23] G. Duhamel, P. Choquet, E. Grillon, L. Lamalle, J. L. Leviel, A. Ziegler, and A. Constantinesco. Xenon-129 mr imaging and spectroscopy of rat brain using arterial delivery of hyperpolarized xenon in a lipid emulsion. *Magn Reson Med*, 46(2):208–12, 2001.
- [24] J. Wolber, D. J. McIntyre, L. M. Rodrigues, P. Carnochan, J. R. Griffiths, M. O. Leach, and A. Bifone. In vivo hyperpolarized 129xe nmr spectroscopy in tumors. *Magn Reson Med*, 46(3):586–91, 2001.
- [25] B. Driehuys, H. E. Moller, Z. I. Cleveland, J. Pollaro, and L. W. Hedlund. Pulmonary perfusion and xenon gas exchange in rats: Mr imaging with intravenous injection of hyperpolarized 129xe. *Radiology*, 252(2):386–93, 2009.

- [26] B. Driehuys, S. Martinez-Jimenez, Z. I. Cleveland, G. M. Metz, D. M. Beaver, J. C. Nouls, S. S. Kaushik, R. Firszt, C. Willis, K. T. Kelly, J. Wolber, M. Kraft, and H. P. McAdams. Chronic obstructive pulmonary disease: safety and tolerability of hyperpolarized ^{129}Xe mr imaging in healthy volunteers and patients. *Radiology*, 262(1):279–89, 2012.
- [27] M. M. Spence, S. M. Rubin, I. E. Dimitrov, E. J. Ruiz, D. E. Wemmer, A. Pines, S. Q. Yao, F. Tian, and P. G. Schultz. Functionalized xenon as a biosensor. *Proc Natl Acad Sci U S A*, 98(19):10654–7, 2001.
- [28] M. M. Spence, E. J. Ruiz, S. M. Rubin, T. J. Lowery, N. Winssinger, P. G. Schultz, D. E. Wemmer, and A. Pines. Development of a functionalized xenon biosensor. *J Am Chem Soc*, 126(46):15287–94, 2004.
- [29] G. K. Seward, Q. Wei, and I. J. Dmochowski. Peptide-mediated cellular uptake of cryptophane. *Bioconjug Chem*, 19(11):2129–35, 2008.
- [30] J. M. Chambers, P. A. Hill, J. A. Aaron, Z. Han, D. W. Christianson, N. N. Kuzma, and I. J. Dmochowski. Cryptophane xenon-129 nuclear magnetic resonance biosensors targeting human carbonic anhydrase. *J Am Chem Soc*, 131(2):563–9, 2009.
- [31] D. M. Dennison. A note on the specific heat of the hydrogen molecule. *Proceedings of the Royal Society of London Series a-Containing Papers of a Mathematical and Physical Character*, 115(771):483–486, 1927.
- [32] K. F. Bonhoeffer and P. Harteck. Experiments on para-hydrogen and ortho-hydrogen. *Naturwissenschaften*, 17:182–182, 1929.
- [33] S. B. Duckett and N. J. Wood. Parahydrogen-based nmr methods as a mechanistic probe in inorganic chemistry. *Coordination Chemistry Reviews*, 252(21-22):2278–2291, 2008.
- [34] C. R. Bowers and D. P. Weitekamp. Para-hydrogen and synthesis allow dramatically enhanced nuclear alignment. *Journal of the American Chemical Society*, 109(18):5541–5542, 1987.
- [35] E. Y. Chekmenev, J. Hovener, V. A. Norton, K. Harris, L. S. Batchelder, P. Bhattacharya, B. D. Ross, and D. P. Weitekamp. Pasadena hyperpolarization of succinic acid for mri and nmr spectroscopy. *Journal of the American Chemical Society*, 130(13):4212–+, 2008.
- [36] Niki M. Zacharias, Henry R. Chan, Napapon Sailasuta, Brian D. Ross, and Pratip Bhattacharya. Real-time molecular imaging of tricarboxylic acid cycle metabolism in vivo by hyperpolarized 1- ^{13}C diethyl succinate. *Journal of the American Chemical Society*, 134(2):934–943, 2011.
- [37] R. W. Adams, J. A. Aguilar, K. D. Atkinson, M. J. Cowley, P. I. P. Elliott, S. B. Duckett, G. G. R. Green, I. G. Khazal, J. Lopez-Serrano, and D. C. Williamson. Reversible interactions with para-hydrogen enhance nmr sensitivity by polarization transfer. *Science*, 323(5922):1708–1711, 2009.
- [38] Lyrelle S. Lloyd, Ralph W. Adams, Michael Bernstein, Steven Coombes, Simon B. Duckett, Gary G. R. Green, Richard J. Lewis, Ryan E. Mewis, and Christopher J. Sleight. Utilization of sabre-derived hyperpolarization to detect low-concentration analytes via 1d and 2d nmr methods. *Journal of the American Chemical Society*, 134(31):12904–12907, 2012.

2 *In vivo* DNP-enhanced MR experiment protocol

Abstract

In vivo hyperpolarized MR via dissolution DNP necessitates the transfer of the hyperpolarized solutions from the DNP polarizer to the imager prior to *in vivo* measurements. This process leads to unavoidable losses in polarization which are difficult to evaluate once the solution is infused into the animal. We propose a method to measure the polarization of the hyperpolarized solutions inside the imager bore at the time of the infusion and quantify the concentration after infusion. This *in situ* calibration allows for decoupling potential problems linked to the hyperpolarization and transfer processes from *in vivo* acquisition issues and can lead to accurate analyses of *in vivo* SNR. In addition, we propose a method to scavenge the radicals a few seconds following the dissolution in order to minimize the losses due to the presence of polarizing agent in the infusate.

Partially adapted from:

T. Cheng, M. Mishkovsky, J. Bastiaansen, O. Ouari, P. Hautle,
P. Tordo, B. van den Brandt and A. Comment

*Methods to minimize and monitor in situ the polarization losses in hyperpolarized
biomolecules prior to in vivo NMR experiments*

Manuscript submitted

2.1 Standard experimental protocol for dissolution DNP

2.1.1 Dissolution DNP setup

The complexity of dissolution DNP, which includes cryogenics, microwaves and magnetic resonance technique makes the DNP experimental setup quite sophisticated. The dissolution DNP method and its associated instrumentation was first introduced by Ardenkjaer-Larsen et al¹. Unlike the commercially available polarizer HypersenseTM, the polarizer used in the frame of this work is based on a separate cryostat sitting inside the bore of a standard room-temperature wide-bore superconducting magnet^{2;3}. To achieve a working temperature of 1 K, a 3-stage pump system with a total pumping volume of 1000 m³ is connected to the cryostat. The cryostat is cooled and refilled from an external helium dewar which can be replaced weekly without stopping operation. To allow continuous operations, a donut-shaped separator is placed between the external helium dewar and sample space to separate the liquid helium from the helium gas. The separated gas is pumped out through a membrane pump and is used to keep the central tube of the cryostat cold. To position the sample in the isocenter of the magnet, a main insert equipped with a NMR circuit is used. A commercially available 140 GHz millimeter wave source (VCOM-06/140/0.5/50-DD, ELVA-1, St. Petersburg, Russia) with a maximum power output of 60 mW is coupled to a waveguide inserted inside the main insert and designed to saturate ESR transition of the unpaired electron spins incorporated inside the sample.

The principle of dissolution DNP is to quickly bring the ultra-cold DNP-enhanced sample to room temperature and therefore to allow for liquid-state or *in vivo* NMR experiments. This is accomplished by warming up a solvent, typically water, under high pressure to a temperature between 180 °C and 200 °C. Afterwards the hyperpolarized solution containing dissolved polarized sample is pushed out from the cryostat by highly pressurized helium gas and transferred into a home-built separator/infusion pump for collection. The pump is located inside the MR scanner dedicated for MRS and 4 m away from the polarizer.

DNP polarizers usually operate at 3.35 T, but recent studies showed that at higher magnetic field the maximum achievable polarization is larger^{3;4}. On the other hand, lower operating temperature also leads to an increasing polarization. The lowest reported temperature used for dissolution DNP is around 0.8 K, achieved by using a closed-cycle sorption pump cryostat. Note that in this thesis all the studies were performed using a DNP polarizer operating at 5 T, i.e. 140 GHz, and 1.05 K. Detailed information about the polarizer hardware can be found in previous dissertations and will not be discussed here^{5;6}.

2.1.2 NMR probes

Low temperature solid-state NMR probes For low-temperature solid-state NMR measurements, a probe containing two sets of capacitors connected through a stainless steel coaxial cable (for low thermal conductivity) was implemented: The low-temperature coil was tuned

2.1. Standard experimental protocol for dissolution DNP

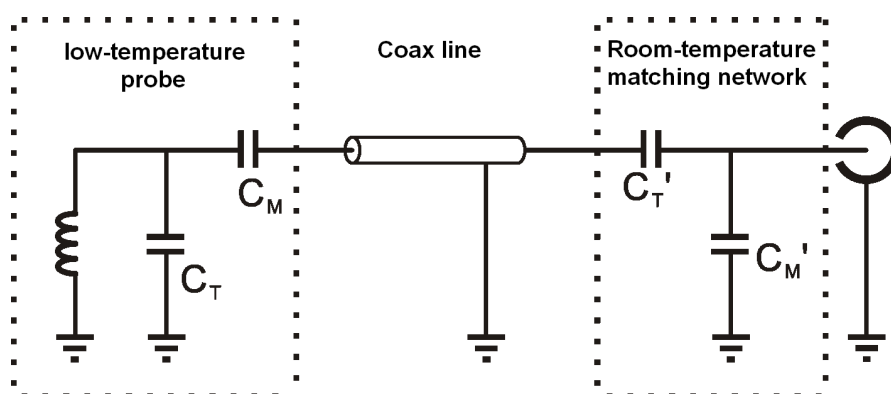


Figure 2.1: NMR probe on the main insert including a low-temperature probe ($\sim 1\text{K}$) and a remote room-temperature tuning/matching network.

and matched close to the desired frequency with the first capacitor set and as the second set a remote room-temperature tuning and matching network was used to fine tune the coil (see figure 2.1).

The coil used for NMR detection is a saddle coil with an inner diameter of 18.9 mm and an optimized geometry for creating a strong B_1 field⁷. Due to the reduced capacitance of the fixed capacitors (100B, American Technical Ceramics, New York, USA) at very low temperature inside helium bath, the coil is pre-tuned and pre-matched to the frequency around 2% lower than the target frequency. The low-temperature circuit extends outside of the cryostat through a stainless steel coax cable fixed on the main insert and connected to the serial matching network consisting of two tunable 60 pF capacitors (NMHTM64C, Voltronics, USA). Note that the number of the coil windings was selected such as to maintain the fixed tuning capacitor value for the low-temperature probe around 10 pF so that the 60 pF variable capacitor of the room-temperature matching network have a large enough effect on the whole circuit to change the NMR resonance in a wide range.

Separator/infusion pump and *in vivo* NMR probes Compared to the design presented in an earlier publication², the new all-plastic separator/infusion pump has two vent ports instead of three. It was modified to allow very fast transfer between the polarizer and the pump. The wall thickness of the main compartment in which the liquid is collected inside the separator/infusion pump (cylinder volume) was also reduced to 1.5 mm in order to place NMR coils with maximized filling factor ($V_{\text{sample}}/V_{\text{coil}} = 0.7$). Two coaxial solenoidal coils with an identical diameter of 19 mm were wound around the main compartment (see figure 2.2): one coil was tuned to ^{13}C frequency and the other one, interleaved with the ^{13}C coil, was tuned to ^1H frequency. The ^{13}C probe quality factor was set to a low-enough value (200) in order to minimize its sensitivity to coil loading, in particular with respect to the sample salt concentration that may vary between experiments. The separator/infusion pump, which was screwed on the NMR insert next to the animal holder, was placed at a horizontal distance Δ away from the isocenter of a 31 cm horizontal bore actively shielded 9.4 T imager (Magnex

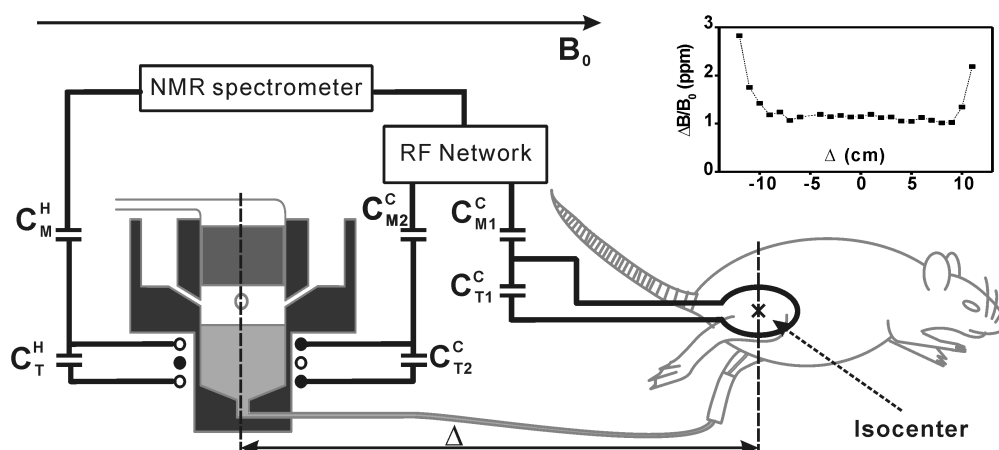


Figure 2.2: Sketch of the experimental setup inside the 31 cm diameter magnet bore. The distance between the axis of the ^{13}C coil wound around the pump (filled circles) and the animal ^{13}C surface coil center was set to $\Delta=6$ cm for *in vivo* skeletal muscle metabolic studies. A ^1H coil (hollow circles) was added to perform the shimming procedure required to reduce the magnetic field inhomogeneity inside the separator/infusion pump. The field homogeneity $\Delta B/B_0$ inside the pump as a function of the distance from the magnet isocenter is shown in the inset. The ^1H coils used for shimming the volume of interest of the animal are not drawn for simplicity.

Scientific, Abingdon, UK) coupled to a Direct Drive spectrometer (Agilent, Palo Alto, CA, USA) (see figure 2.2). To determine the maximum distance Δ at which the field homogeneity $\Delta B/B_0$ was high enough to perform NMR measurements inside the pump, the insert was moved along the magnet bore axis and the ^{13}C signal of a 1 M $[1-^{13}\text{C}]$ acetate solution (2.5 mL) was measured each 1 cm for values between -12 and +12 cm. The field homogeneity over the volume of interest was determined from the ^{13}C spectral line width and it was observed that it is nearly constant for all Δ between -8 and +8 cm (see figure 2.2 inset). For larger Δ it was not possible to adequately compensate the field inhomogeneity within the volume of interest with the imager shim coils.

The *in vivo* measurements were performed with a home-built dual $^1\text{H}/^{13}\text{C}$ probe consisting of two 13 mm diameter ^1H coils in quadrature and a 10 mm diameter ^{13}C coil placed over the area of interest of the rodent which is placed at the isocenter of the imager. Details about the probe designed for *in vivo* applications are given in Chapter 5.

^{13}C probes switching scheme The goal was to design a setup allowing to perform consecutive ^{13}C NMR measurements on two different probes with a single low-band channel spectrometer. Both ^{13}C probes are connected to the same spectrometer channel via a RF network allowing switching between the probe located on the separator/infusion pump for *in vitro* measurements and the probe placed on the animal for *in vivo* measurements (see figure 2.3). A highly-isolated TTL-triggered RF broadband switch (Type ZX80-DR230-S+, Minicircuits, Munich, Germany) is connected to the low-band transmitter output of the spectrometer and

2.1. Standard experimental protocol for dissolution DNP

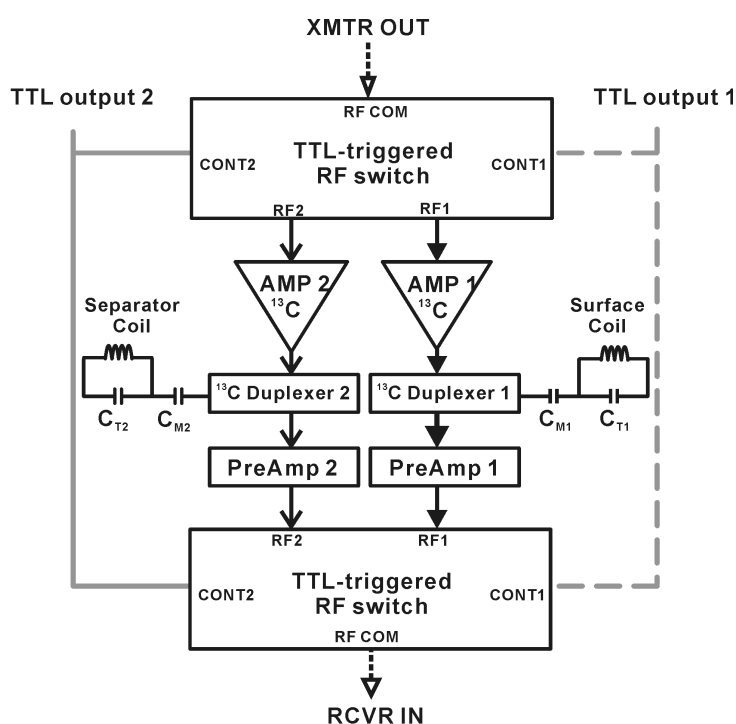


Figure 2.3: Home-built RF network to switch between two ^{13}C probes connected to a single low-band channel spectrometer (Varian, Palo Alto, CA, USA)

placed in front of the two power amplifiers used to generate the high-power RF pulses for the animal coil (350 W amplifier; Varian, Palo Alto, CA, USA) and for the pump coil (100 W amplifier; Tomco, Australia). The NMR signals are preamplified through two separated 30 dB low-noise amplifiers (Varian, Palo Alto, CA, USA) before being fed into the spectrometer receiver through a second identical TTL-triggered RF switch. The time required to switch the electronics paths from one probe to the other is less than $5\ \mu\text{s}$. Due to the switches insertion losses (0.8 dB at 100.67 MHz) and the losses in the additional coaxial cables (1-2 dB), RF pulses power has to be adjusted for both coils following the insertion of the RF network. The high isolation level (-78 dB) of the RF switches strongly limited signal contamination between the two ^{13}C electronics paths.

2.1.3 DNP sample preparation

DNP samples usually consist of three parts: substrates containing nuclear spins of interest, radicals used as a source of unpaired electron spins and solvent mixture (usually water mixed with a glassy agent such as ethanol or glycerol) to dissolve the substrates and radicals. The prepared solution may need to be warmed up and has to be visually checked for unwanted precipitation.

The radicals used for DNP can be classified into two categories: the stable free radicals and radiation induced radicals (note that photo-excited triplet states have also been used as source of electron spins in pentacene and naphthalene). The commercially available stable radicals include TEMPO (2,2,6,6-Tetramethyl-1-piperidinyloxy) with its derivatives and trityl

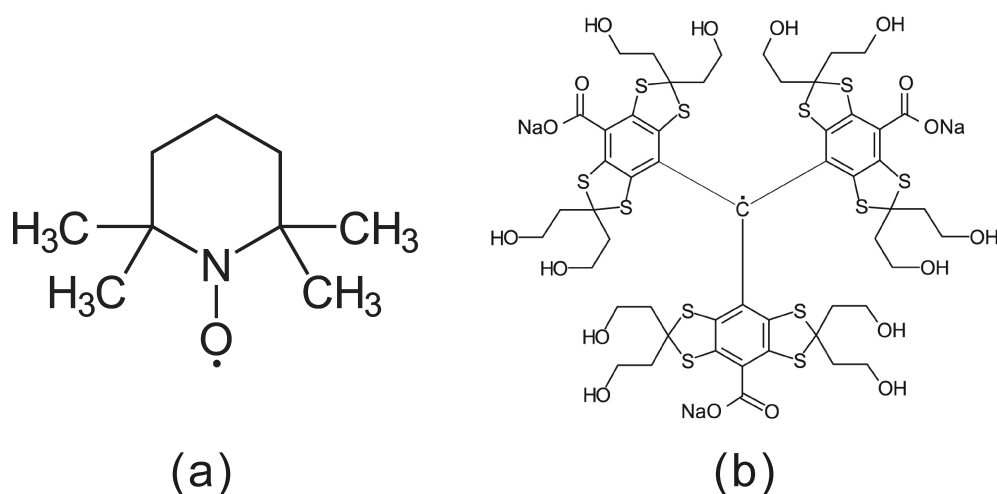


Figure 2.4: Chemical structures of (a)TEMPO radical and (b)trityl radical OX063.

radicals as OX063 as well as Finland (chemical structures see figure 2.4). The radiation induced radicals are defects produced inside a frozen sample by soft and hard x-rays. This technique was used for creating polarized targets with alcohols⁸. Both radical species have their own advantages and disadvantages. For stable radicals, it is easy to control their concentration in the sample, but they are potentially toxic to the biological tissues even at low concentration and their paramagnetism shortens the nuclear spins relaxation time. On the contrary, the radiation-induced radicals recombine themselves once the frozen samples are melted, but the numbers, structures and production efficiency of the radicals are difficult to control. In this thesis nitroxyl radicals were used in most of the experiments and some results related to x-ray induced radicals are summarized in the appendix B.

Several solvent mixtures matrices can be chosen for preparing DNP samples including deuterated or protonated water/EtOD as well as water/glycerol. The criteria for selecting optimal solvent mixture includes the solubility of the substrate and the radicals, the amount of glassy agent needed for the preparation and the deuteration level of the solvents. Regarding to the polarization time increased magnetic field and deuteration level lead to larger build up time constant; on the contrary, increased concentration of either nuclear spins or radicals leads to shorten build up time.

The solution containing the substrate is usually frozen into small transparent beads by plunging droplets in liquid nitrogen using a syringe and a needle. The main advantages of preparing beads as compared to a large block of sample are: first, to ensure good absorption of microwave by reducing the sample size over skin depth ratio; second, to ensure good cooling performance by the helium bath around 1 K and last but not least, also to ensure a large contact surface to hot water for the dissolution procedure. After mixing all the compound check the transparency of the beads and store them in a labeled sample container. The bead volume can be adjusted by using different size of needle and is normally around 10-15 μL .

2.1.4 DNP experiment protocol

Hyperpolarization process, transfer, and in vitro measurements 300 μL of sample in the form of glassy frozen beads are loaded and dynamically polarized at 5 T and 1.02 ± 0.03 K using the hardware described in section 2.1.1. The ^{13}C solid-state polarization is then monitored by applying a 5° flip angle pulse every 5 minutes using the probe for low temperature solid-state NMR described in section 2.1.2. Reasonably small flip angles and long time intervals are chosen to avoid large polarization losses due to the RF pulses (more analyses is shown in appendix D). Once the polarization level has reached plateau, the sample will be rapidly dissolved in 5 mL of superheated D_2O . Immediately after dissolution, a pressure differential is created for 2 s across a 5 m long and 2 mm inner diameter PTFE tube using pressurized helium gas. The optimal pressure for the transfer has been determined to be 6 bar. With this pressure, maximal 2.4 ± 0.1 mL is transferred through 5 m of tube in 2 s. The hyperpolarized solution is then collected in the separator/infusion pump connected at the end of the tube and positioned inside the imager bore. A 1 s delay between the end of the application of the high-pressure gas and the injection is set to allow the solution to settle at the bottom of the pump, where the ^{13}C coil and the injection port are located (see figure 2.2). The ^{13}C signal from the hyperpolarized solution is then measured inside the separator/infusion pump. To determine T_1 , series of 5° pulses are applied with a repetition time of 3s. For *in vivo* experiments, a single 5° flip angle pulse is applied at the time the infusion started, i.e., 3 s after dissolution.

***in vivo* measurements protocol** Once the animal is positioned inside the imager magnet, 10 image slices in axial direction with 1 mm thickness are acquired using a gradient echo sequence (TR = 50 ms, TE = 3 ms, field of view = 30×30 mm², matrix = 128×128 , flip angle = 30° from the selected volume of interest (VOI). The static magnetic field is homogenized in a 600 μL ($6 \times 10 \times 10$ mm³) voxel to reduce the localized proton line width to 20 Hz using the FASTESTMAP shimming protocol⁹. A pre-selected volume of the dissolved hyperpolarized solution through combining various limit rings is injected within 9 s. Series of single-pulse ^{13}C acquisitions are sequentially recorded starting 12 s after dissolution using 30° adiabatic RF pulses (BIR4) applied every 3 s with ^1H decoupling during acquisition (WALTZ) (a typical spectrum is shown in figure 2.7C). The adiabatic pulses offset and power are set such as to ensure a homogeneous 30° excitation of substrate and metabolite resonances within the entire VOI. Since the pump and the animal are located at a distance Δ from one to another, two different sets of shim parameters determined and saved prior the dissolution and injection are used to perform the consecutive NMR measurements in the pump and *in vivo* respectively. The shim current values are changed during the injection (this is performed in a few seconds by the imager control electronics).

2.2 Method to minimize and monitor in situ the polarization losses

To quantify and possibly minimize the polarization losses, it is necessary to accurately measure the polarization following the transfer from the polarizer to the imager. The *in vivo*

signal enhancement is however difficult to estimate since the thermal equilibrium signal needed to determine the polarization is too small to be detected once the solution has been injected. Measuring the polarization *ex situ* by inserting part of the hyperpolarized solution in a dedicated NMR setup (sometimes referred to as "polarimeter") is also inaccurate since the hyperpolarized solution is subject, during the transfer between polarizer and imager on one side, and polarizer and polarimeter on the other, to unequal dramatic time variations in magnetic field which may strongly affect nuclear spin relaxation. A precise quantification of the polarization at the time of the injection would allow for distinguishing between signal modulations related to variations in the nuclear polarization prior to injection and signal modulations related to physiological processes such as tissue perfusion.

It has already been shown that nitroxyl radicals that are used for DNP can be scavenged by ascorbate¹⁰, but the proposed method leads to strongly reduced concentrations of hyperpolarized molecules following dissolution since the frozen droplets of ascorbate solution placed inside the polarizer take a large part of the available sample space. It is thus not optimal for biomedical applications. Note that an additional proposed solution to reduce the nuclear spin polarization losses due to relaxation is to create singlet states which have a much longer life time but it can only be applied to specific types of molecules¹¹⁻¹⁵.

This study was performed using DNP sample containing 4.5 M sodium [1-¹³C]acetate and 33 mM TEMPO radicals. The solvent mixture was a combination of D₂O and EtOD in a ratio of 2:1. This method was applied to *in vivo* metabolic studies of rat skeletal muscle.

Scavenging nitroxyl radicals inside the separator/ infusion pump The nitroxyl radicals scavenging process took place inside the separator/infusion pump at the bottom of which 1 mL of L-ascorbate sodium (NaAsc) or L-ascorbic acid (AA) (Sigma-Aldrich, Buchs, Switzerland) aqueous (D₂O) solution at different concentrations was loaded prior to dissolution. The temperature inside the separator/infusion pump was monitored and maintained by blowing hot air into the imager bore. The concentration of the vitamin C (NaAsc and AA) aqueous (D₂O) solutions introduced inside the separator/infusion pump prior to dissolution experiments ranged from 0.1 M to 2 M. The temperature of the separator/infusion pump was stabilized at 33 °C. Following the transfer of the hyperpolarized solution and after rapid mixing with the aqueous solution introduced inside the pump, the final vitamin C concentration of the infusate was ranging from 40 mM to 800 mM. It was observed that the temperature of the infusate is always within 5 °C of the pump temperature at the end of the transfer and consecutively stabilizes at the pump temperature within 3 ± 0.5 minutes. The longitudinal relaxation times of [1-¹³C]acetate were deduced from fitting the ¹³C signal decays measured in the infusion pump with a mono-exponential decaying function after having corrected for the effect of the RF pulses on the signal intensities. The ¹³C values were measured for several vitamin C infusate concentrations (hollow symbols in figure 2.5).

The ¹³C T₁ of thermally polarized 0.2 M sodium [1-¹³C]acetate aqueous (D₂O) solutions containing various concentrations of vitamin C were independently measured on a vertical

2.2. Method to minimize and monitor in situ the polarization losses

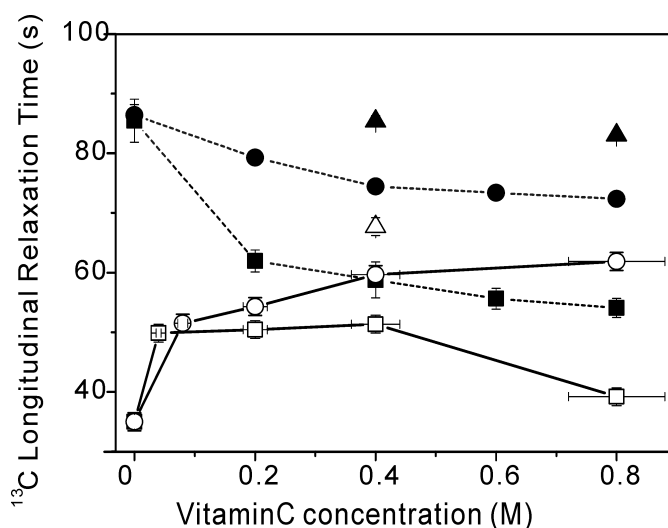


Figure 2.5: In vitro ^{13}C T_1 measurements of sodium $[1-^{13}\text{C}]$ acetate in aqueous (D_2O) solutions at 33°C as a function of NaAsc (circles), AA (squares), or deuterated NaAsc (triangles) concentration. Experiments with 0.25 ± 0.05 M hyperpolarized acetate solutions containing 2 ± 0.3 mM TEMPO were performed following dissolution and mixing with vitamin C in the separator/infusion pump placed in the 9.4 T imager (hollow symbols). The vertical errors bars originate from the 5°C uncertainty on the solutions temperature. The thermally polarized 0.2 M acetate solutions (without added nitroxyl radicals) were measured in a vertical 9.4 T high-resolution system (full symbol).

9.4 T high-resolution system (Bruker BioSpin SA, Fallanden, Switzerland) using a standard saturation recovery pulse sequence (full symbols in figure 2.5). The solutions did not contain nitroxyl radicals and they were deoxygenated by bubbling nitrogen gas at the bottom of the 5 mm NMR tubes for 15 minutes.

Partially deuterated L-NaAsc was prepared by lyophilizing a solution containing normal sodium ascorbate and D_2O placed in a dark environment for at least two weeks. The ^1H spectra of natural abundance and partially deuterated sodium ascorbate solutions (1 M) in D_2O were compared to determine the deuteration level in the extracted salt. 30 minutes after having dissolved the natural abundance salt in D_2O , most of the four exchangeable protons from the ascorbate hydroxyl groups were substituted by deuterons leading to a large H_2O signal. The H_2O signal integral was compared to the one measured in the partially deuterated sodium ascorbate solution. The result showed that 89% of the exchangeable protons had been replaced by deuterons in the partially deuterated sodium ascorbate salt. The ^{13}C T_1 of sodium $[1-^{13}\text{C}]$ acetate in aqueous (D_2O) solutions containing 0.4-0.8 M of partially deuterated NaAsc are also determined through both a dissolution DNP experiment, including a nitroxyl scavenging step inside the separator/infusion pump as described above, and a standard saturation recovery experiment performed in a vertical 9.4 T high-resolution MR system. The resulting T_1 values are reported in figure 2.5 (triangles). The ^{13}C signal integral decay measured in a 0.4 M deuterated NaAsc solution after the dissolution DNP experiment is reported in

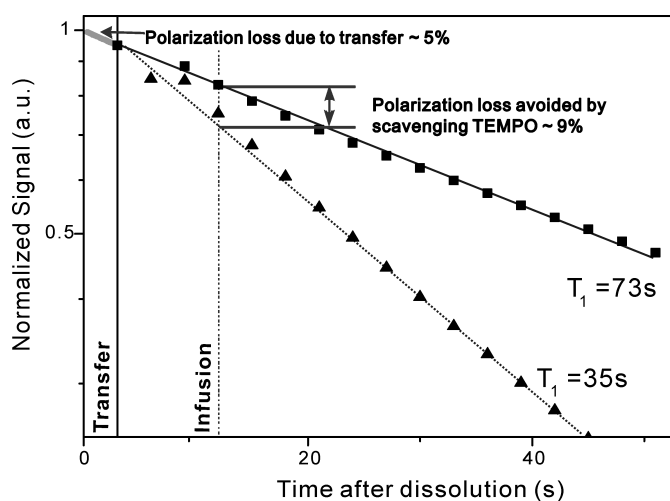


Figure 2.6: ^{13}C signal decay of hyperpolarized sodium $[1-^{13}\text{C}]$ acetate with (■) and without (Δ) deuterated NaAsc (1 M); the polarization was about 9% larger at the end of the infusion when the nitroxyl radicals were scavenged inside the pump as proposed herein.

figure 2.6 along with the ^{13}C signal integral decay measured following a dissolution DNP experiment performed without radical scavenging molecules. A loss of polarization resulting from the transfer between the polarizer and the imager is unavoidable but our fast transfer scheme limits it to 2 – 5% for hyperpolarized $[1-^{13}\text{C}]$ acetate solutions. Once the solution has been transferred into the imager bore, the polarization losses can be strongly reduced by scavenging the radicals inside the separator/infusion pump. In the case of hyperpolarized $[1-^{13}\text{C}]$ acetate, we showed that, if the pump was pre-filled with a 1 M deuterated NaAsc solution, we could reduce the ^{13}C polarization losses by roughly 1% per second corresponding to a gain of about 9% of polarization by the end of the 9 s-long injection (see figure 2.6). Note that the substantial gain in polarization also leads to an extension of the time window available for *in vivo* measurements.

***In situ* polarization quantification and *in vivo* measurements** The ^{13}C polarization after 2 hours of microwave irradiation was estimated to be $12 \pm 1\%$ in all experiments ($n=5$) by comparing the polarized ^{13}C signal with the 1 K ^{13}C thermal equilibrium signal of the same sample measured separately. The ^{13}C solid-state DNP polarization build-up time constant of $[1-^{13}\text{C}]$ acetate was 1900 ± 50 s. The liquid-state polarization was determined by comparing the hyperpolarized signal (figure 2.7B) with either the signal from a thermally polarized reference sample of known concentration when the solution was injected, or the thermal equilibrium signal when the solution was kept inside the pump to perform T_1 measurements. We measured an enhancement factor of 15500 ± 1000 , which corresponds to a polarization of $12 \pm 1\%$. The *in vivo* acquisition started 3 s after the beginning of the 9 s-long injection. The large $[1-^{13}\text{C}]$ acetate signal was readily detected and, in agreement with Jensen et al.¹⁶, we observed the formation of the metabolic product $[1-^{13}\text{C}]$ acetylcarnitine 8.7 ppm upfield (see figure 2.7C). A characteristic *in vivo* decay time of around 16 ± 1 s was determined for acetate

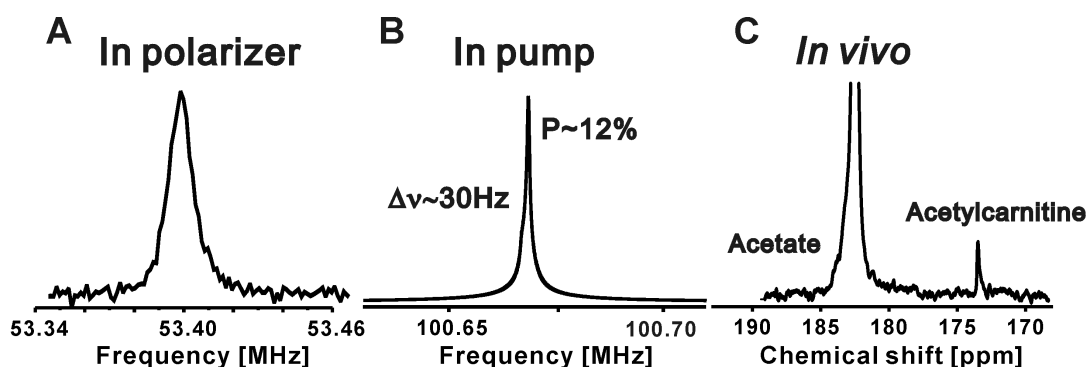


Figure 2.7: Three consecutive single-shot low-flip angle ^{13}C measurements during a metabolic study: A. 5 T/1 K solid-state signal in the polarizer B. Liquid-state signal inside the pump at the time the infusion started C. *in vivo* $[1-^{13}\text{C}]$ acetate and $[1-^{13}\text{C}]$ acetylcarnitine signals in the rat skeletal muscle.

and the *in vivo* metabolite acetylcarnitine in the skeletal muscle was observed over a time period of 30 s.

2.3 Discussion

In-line in situ polarization measurements Throughout the *in vivo* hyperpolarized NMR experiments presented herein, the ^{13}C signal of the same polarized $[1-^{13}\text{C}]$ acetate sample was measured at three different stages (see figure 2.7): in the solid-state, about 1 min prior to dissolution, in the liquid-state, 3 s after dissolution after having been transferred inside the imager bore, and finally *in vivo* in skeletal muscle, a few seconds after the injection started. Since the *in vitro* liquid-state measurement is performed at the beginning of the injection, lasts less than 1 s, and can be performed with a very low flip-angle RF pulse, it has no substantial effect on the *in vivo* measurements. Most notably, this additional NMR measurement does not increase the delay between dissolution and injection and negligibly affect the *in vivo* signals intensity.

Accurately measuring the nuclear polarization prior to injection can greatly facilitate the interpretation of *in vivo* results. In case the *in vivo* signals intensity in a specific experiment is substantially different from the average value, the polarization measurement will provide a way to decouple issues linked to the hyperpolarization and transfer processes from problems related to the injection or animal physiology. The variations in substrate and metabolites signals intensity are linked to differences in tissue perfusion and a quantitative comparison across subjects should be possible if the intensities are rescaled by the polarization level measured at the time of the injection. Accurate in situ polarization measurements are also of great importance when several substrates are polarized and injected at the same time¹⁸. To be meaningful, the relative intensities between the different substrates and their metabolites have to be weighted by the polarization level at the time of infusion. This is particularly

Chapter 2. *In vivo* DNP-enhanced MR experiment protocol

essential if the low-field T_1 is dramatically different for the different substrates as is the case for $[1-^{13}\text{C}]$ pyruvic acid and $[1-^{13}\text{C}]$ urea.

We demonstrated the applicability of our method to *in vivo* hyperpolarized NMR experiments in the framework of a skeletal muscle metabolic study. The method is also compatible with other types of *in vivo* applications such as cerebral or cardiac metabolic studies although the pump might have to be placed farther away from the isocenter due to the animal and surface coil location. The field homogeneity in the 9.4 T imager used for the present studies was sufficient up to about 10 cm away from the isocenter and additional shim coils could be added around the separator if larger distances were required.

Radicals scavenging The strong influence of TEMPO on the ^{13}C carboxyl T_1 of acetate has already been determined in a previous publication¹⁹. Therefore, as expected¹⁰, the addition of vitamin C in $[1-^{13}\text{C}]$ acetate aqueous (D_2O) solutions containing 2 ± 0.3 mM TEMPO led to an increase in ^{13}C T_1 (see figure 2.5, filled symbols). To increase the kinetics of the scavenging process, large concentrations (M range) need to be used. The increase in ^{13}C T_1 with increasing vitamin C concentration observed in the dissolution DNP experiments indeed demonstrate the strong influence of the scavenger concentration on the kinetics and the near-unity R values ($R > 0.999$) observed for all vitamin C concentrations larger than 0.2 M (see example on figure 2.6) show that a large fraction of the radicals are rapidly scavenged. However, the concentrations used in our dissolution DNP experiments do not seem to be large enough to completely cancel out the effect of the radicals on the ^{13}C relaxation since even with the largest concentrations (0.8 M) the observed T_1 's do not quite match the values measured in thermally polarized solutions (see figure 2.5). Our results also show that the addition of large quantities of vitamin C lead to a substantial shortening of the ^{13}C T_1 's. The effect was clearly more pronounced with AA than with NaAsc as confirmed by the T_1 measurements performed on thermally polarized solutions (see figure 2.5, hollow symbols). Following the observation that T_1 was not substantially affected by the pH of the solution (data not shown), we deduced from the comparison between the ^{13}C longitudinal relaxation obtained in solutions containing either AA, NaAsc, deuterated AA (data not shown), or deuterated NaAsc that the concentration of exchangeable protons added to the solutions through the incorporation of vitamin C was the cause of the additional relaxation. This was confirmed by measuring the ^{13}C T_1 of $[1-^{13}\text{C}]$ acetate in aqueous (D_2O) solutions (0.2 M) containing either 1 M AA and 1 M NaCl or 1 M NaAsc and 1M HCl (both solutions had the same pH of 3.4). The carboxyl ^{13}C T_1 of acetate was identical in both solutions (45 ± 1 s). As was already observed in $[1-^{13}\text{C}]$ glycine aqueous solutions²⁰, the stronger dipolar fields induced by protonated water as compared to deuterated water strongly reduce the long T_1 of the carboxyl ^{13}C spins. Since vitamin C is a diprotic acid with pKa values of 4.21 and 11.79, the amount of protons exchanged with the solvent within the time course of an experiment is much larger in AA solutions than in NaAsc solutions (see figure 2.8).

We deduced that the optimal aqueous (D_2O) scavenging solution to be inserted inside the separator/infusion pump should contain 1-2 M of deuterated NaAsc (much higher con-

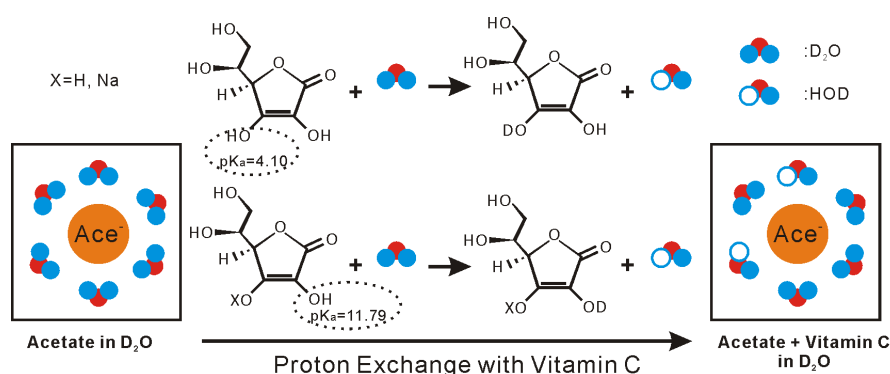


Figure 2.8: Effect of proton exchange between vitamin C and water molecules on the magnetic environment of acetate molecules in aqueous (D₂O) solutions.

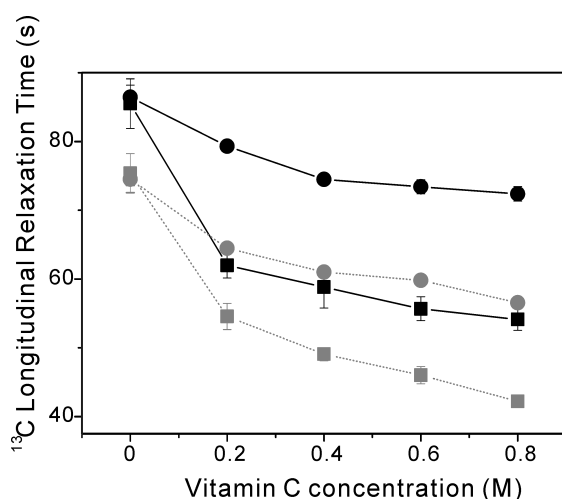


Figure 2.9: In vitro ¹³C T₁ measurements of [1-¹³C]sodium acetate in aqueous (D₂O) solutions at 33°C (black) and 17°C (grey) as a function of NaAsc (circles) or AA (squares) concentration. No aminoxyl radicals were added to the solutions.

centrations are not possible due to the solubility threshold of sodium ascorbate in D₂O (2.5 M at 25°C), which corresponds to a final infusate concentration of 0.4-0.8 M. A signal intensity gain of 9% was observed at the end of the 9 s infusion in a 0.4 M solution. The gain in signal would be even larger for longer injection times. Similar T₁ measurements were performed at 17°C, which is the base temperature of the separator/infusion pump inside the imager if the hot air is turned off. Although the same behavior was observed when the concentration of vitamin C is increased (see figure 2.9), it showed that the T₁ values are significantly lower at 17°C. Besides the significant increase in T₁, two additional reasons lead to the use of hot air to maintain the infusion pump at 33°C: first, the scavenging reaction kinetics is faster at higher temperature and second, the temperature of the hyperpolarized solution is nearly at body temperature at the time of injection since it is within 5°C of the pump temperature after its transfer into the pump.

In summary, the method presented herein allows (a) to precisely determine the infusate ¹³C polarization inside the imager at the time of the injection without additional delay between dissolution and injection, (b) to scavenge the radicals used as polarizing agents without the

cost of reducing the final infusate concentration, and (c) to start the injection of hyperpolarized solutions into live animals as rapidly as 3 s following dissolution. This automated protocol leads to highly reproducible experiments and can facilitate the quantitative analysis of *in vivo* hyperpolarized NMR experiments while minimizing the signal losses.

References

- [1] J. H. Ardenkjaer-Larsen, B. Fridlund, A. Gram, G. Hansson, L. Hansson, M. H. Lerche, R. Servin, M. Thaning, and K. Golman. Increase in signal-to-noise ratio of > 10,000 times in liquid-state nmr. *Proceedings of the National Academy of Sciences of the United States of America*, 100(18):10158–10163, 2003.
- [2] A. Comment, B. van den Brandt, K. Uffmann, F. Kurdzesau, S. Jannin, J. A. Konter, P. Hautle, W. T. H. Wenckebach, R. Gruetter, and J. J. van der Klink. Design and performance of a dnp prepolarizer coupled to a rodent mri scanner. *Concepts in Magnetic Resonance Part B-Magnetic Resonance Engineering*, 31B(4):255–269, 2007.
- [3] S. Jannin, A. Comment, F. Kurdzesau, J. A. Konter, P. Hautle, B. van den Brandt, and J. J. van der Klink. A 140 ghz prepolarizer for dissolution dynamic nuclear polarization. *Journal of Chemical Physics*, 128(24), 2008.
- [4] H. Johanneson, S. Macholl, and J. H. Ardenkjaer-Larsen. Dynamic nuclear polarization of [1-c-13]pyruvic acid at 4.6 tesla. *Journal of Magnetic Resonance*, 197(2):167–175, 2009.
- [5] S. Jannin. *Dynamic nuclear polarization techniques for magnetic resonance imaging and particles targets experiments*. PhD thesis, 2009.
- [6] F. Kurdzesau. *Some methods of dynamic nuclear polarization for use in metabolic imaging*. PhD thesis, 2009.
- [7] D. M. Ginsberg and M. J. Melchner. Optimum geometry of saddle shaped coils for generating a uniform magnetic field. *Review of Scientific Instruments*, 41(1):122–123, 1970.
- [8] S. T. Goertz, J. Harmsen, J. Heckmann, C. Hess, W. Meyer, E. Radtke, and G. Reicherz. Highest polarizations in deuterated compounds. *Nuclear Instruments & Methods in Physics Research Section a-Accelerators Spectrometers Detectors and Associated Equipment*, 526(1-2):43–52, 2004.
- [9] R. Gruetter. Automatic, localized in vivo adjustment of all first- and second-order shim coils. *Magnetic Resonance in Medicine*, 29(6):804–11, 1993.
- [10] P. Mieville, P. Ahuja, R. Sarkar, S. Jannin, P. R. Vasos, S. Gerber-Lemaire, M. Mishkovsky, A. Comment, R. Gruetter, O. Ouari, P. Tordo, and G. Bodenhausen. Scavenging free radicals to preserve enhancement and extend relaxation times in nmr using dynamic nuclear polarization. *Angewandte Chemie-International Edition*, 49(43):7834–7834, 2010.
- [11] M. Carravetta, O. G. Johannessen, and M. H. Levitt. Beyond the t-1 limit: Singlet nuclear spin states in low magnetic fields. *Physical Review Letters*, 92(15), 2004.
- [12] P. R. Vasos, A. Comment, R. Sarkar, P. Ahuja, S. Jannin, J. P. Ansermet, J. A. Konter, P. Hautle, B. van den Brandt, and G. Bodenhausen. Long-lived states to sustain hyperpolarized magnetization. *Proceedings of the National Academy of Sciences of the United States of America*, 106(44):18469–18473, 2009.
- [13] W. S. Warren, E. Jenista, R. T. Branca, and X. Chen. Increasing hyperpolarized spin lifetimes through true singlet eigenstates. *Science*, 323(5922):1711–1714, 2009.
- [14] M. C. Tayler, I. Marco-Rius, M. I. Kettunen, K. M. Brindle, M. H. Levitt, and G. Pileio. Direct enhancement of nuclear singlet order by dynamic nuclear polarization. *J Am Chem Soc*, 134(18):7668–71, 2012.

- [15] C. Laustsen, G. Pileio, M. C. Tayler, L. J. Brown, R. C. Brown, M. H. Levitt, and J. H. Ardenkjaer-Larsen. Hyperpolarized singlet nmr on a small animal imaging system. *Magnetic Resonance in Medicine*, 2012.
- [16] P. R. Jensen, T. Peitersen, M. Karlsson, R. In 't Zandt, A. Gisselsson, G. Hansson, S. Meier, and M. H. Lerche. Tissue-specific short chain fatty acid metabolism and slow metabolic recovery after ischemia from hyperpolarized nmr in vivo. *J Biol Chem*, 284(52):36077–82, 2009.
- [17] M. Mishkovsky, A. Comment, and R. Gruetter. In vivo detection of brain krebs cycle intermediate by hyperpolarized magnetic resonance. *J Cereb Blood Flow Metab(accepted)*, 2012.
- [18] D. M. Wilson, K. R. Keshari, P. E. Larson, A. P. Chen, S. Hu, M. Van Criekinge, R. Bok, S. J. Nelson, J. M. Macdonald, D. B. Vigneron, and J. Kurhanewicz. Multi-compound polarization by dnp allows simultaneous assessment of multiple enzymatic activities in vivo. *Journal of Magnetic Resonance*, 205(1):141–7, 2010.
- [19] A. Comment, J. Rentsch, F. Kurdzesau, S. Jannin, K. Uffmann, R. B. van Heeswijk, P. Hautle, J. A. Konter, B. van den Brandt, and J. J. van der Klink. Producing over 100 ml of highly concentrated hyperpolarized solution by means of dissolution dnp. *Journal of Magnetic Resonance*, 194(1):152–5, 2008.
- [20] H. Pearson, D. Gust, I. M. Armitage, H. Huber, J. D. Roberts, R. E. Stark, R. R. Vold, and R. L. Vold. Nuclear magnetic resonance spectroscopy: reinvestigation of carbon-13 spin-lattice relaxation time measurements of amino acids. *Proc Natl Acad Sci U S A*, 72(4):1599–601, 1975.

3 Producing radical-free hyperpolarized solutions for *in vivo* MR

Abstract

Dissolution DNP allows achieving tremendous gain in SNR in NMR experiments. Once the polarized sample is dissolved, the stable radicals used as polarizing agents become undesirable since their presence is an additional source of nuclear spin relaxation and their toxicity might be an issue. We demonstrate here that by using spin-labeled thermoresponsive hydrophilic polymer networks it is possible to prepare hyperpolarized solutions free of stable radicals immediately after dissolution. We applied this method to hyperpolarize ^{13}C -labeled *tert*-butanol which has been recently shown to be a promising contrast agent for perfusion imaging.

Partially adapted from:

T. Cheng, M. Mishkovsky, J. N. Junk, D. Hinderberger
K. Muennemann and A. Comment

Producing radical-free hyperpolarized solutions for in vivo magnetic resonance
Manuscript in preparation

3.1 Introduction

Dissolution DNP has become the most attractive technique for enhancing the sensitivity of NMR and its associated imaging methods because of its versatility. The nuclear polarization of protons, ^{13}C and ^{15}N spins can be enhanced by 3 to 4 orders of magnitude to give tremendous gain in SNR in *in vivo* NMR experiments. To perform DNP, it is necessary to introduce paramagnetic centers inside the sample containing the nuclear spins to be polarized. For liquid-state NMR, MRS and MRI, there are two main issues linked to the presence of stable radicals in the samples: (a) for *in vivo* applications in animals or humans, radical species have to be filtered out for toxicity issues; due to this procedure, the time delay between preparation and injection of the hyperpolarized molecules is increased and lead to losses in polarization as a consequence of nuclear spin relaxation. It also introduces the risk of contamination and thus requires pharmacological tests that further increase the delay; (b) the radicals have an adverse effect on the lifetime of the DNP-enhanced nuclear polarization through nuclear spin relaxation, both in the solid-state and in the liquid-state. It is thus necessary to rapidly warm up and dilute the sample to transform the frozen samples containing about 10-100 mM of stable radicals into a liquid with a largely reduced radical concentration, typically less than 1 mM.

Most dissolution DNP studies performed with the commercial DNP polarizer HyperSense™ used trityl radicals, OX063, Finland and their derivatives, as polarizing agents. These radicals have an extremely narrow ESR linewidth and they were shown to efficiently polarize ^{13}C -labeled biomolecules, especially pyruvic acid¹⁻³ for *in vivo* small animal experiments^{4,5}. It has been reported that trityl radicals can be removed by using mechanical filter and a final radical concentration after filtering can be controlled around $1\mu\text{M}$ ⁶ which is far lower than the median lethal dose (LD_{50}) value of 7mmol/Kg ⁷ for OX063.

The other type of polarizing agent currently used in dissolution DNP is the nitroxyl radicals including TEMPO and its derivatives. Unlike the trityl radicals, nitroxyl radicals usually have a broad ESR inhomogeneous line width. The maximum ^{13}C polarization at a given field and temperature is thus usually lower than with trityl radicals, but all nuclear spins can be polarized, in particular protons⁸⁻¹⁰. Due to the large LD_{50} value of $\sim 600\text{ mg/Kg}$, nitroxyl radicals were also used for *in vivo* DNP studies¹¹⁻¹³. Another advantage of nitroxyl radical which has been extensively discussed in chapter 2, is that it is feasible to scavenge them to a non-paramagnetic molecule using vitamin C.

Radiation-induced radicals created in solid samples at low temperature were reported to be highly efficient for polarizing specific nuclei in polarized targets^{14,15}. Unlike stable radicals, radiation-induced radicals are quenched through recombinations when the sample is melted and therefore no radical is left in the liquid-state sample. The drawback of this technique is that several types of radicals are created and if the sample is composed of several compounds the ESR line width will become prohibitively large. Instead of radiolysis, Kumada et al. showed the possibility of using precursor molecules transformed in radicals through UV photolysis for

DNP¹⁶. Similarly to radiation-induced radicals, UV-induced radicals will recombine during the warming process of the sample. Moreover, the yield of radical creation can be several folds higher by accelerating the photolysis process through addition of a photosensitizer.

The idea of producing radical-free DNP-enhanced molecules was developed for Overhauser DNP techniques. The immobilization of radicals using water-soluble polymer networks, on which stable radicals are chemically bound, was successfully implemented^{17;18}. Since Overhauser DNP takes place at room-temperature, this strategy makes steady-state injection and detection of polarized tracer possible and attractive for further development and potential clinical applications. Recently, a similar type of polymer network named thermoresponsive spin-labeled hydrophilic polymer networks (SL-hydrogel) was developed to polarize ¹H spins¹⁹. In this study we used the same kind of hydrogel to hyperpolarize ¹³C in samples via dissolution DNP. We demonstrate that by using spin-labeled thermoresponsive hydrogel, it is possible to prepare hyperpolarized solutions free of stable radicals immediately after dissolution.

3.2 Materials and Methods

3.2.1 Thermoresponsive spin-labeled hydrogel

A thermoresponsive hydrogel is a special polymer network soluble in water and contains temperature sensitive part and radical-linked part. Upon heating, the hydrogel quickly shrinks and the solvent is expelled from the polymer network (see figure 3.1). Since the radicals are covalently bound to the hydrogel and therefore immobilized in the gel, the extracted hyperpolarized solutions do not contain stable radicals. Thermoresponsive spin-labeled hydrogel is synthesized through polymerization of N,N-ethylmethacrylamids (EMAAM) and amino-functionalized nitroxide linked Methacrylic acid (MAA). The former is working as thermoresponsive unit which can bear a critical solution temperature of 63°C and the percentage of the latter in a sample determines the average radical concentration under swollen state.

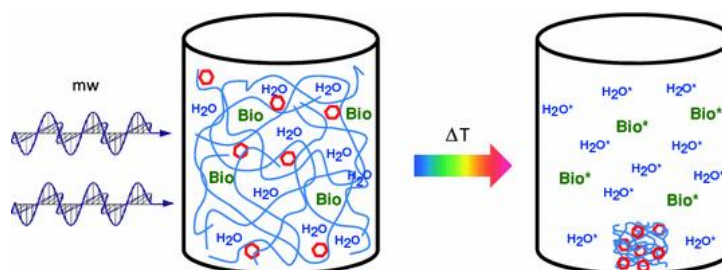


Figure 3.1: Principle of how a thermoresponsive SL-hydrogel works²⁰.

3.2.2 DNP procedure

d_{10} -*tert*-butanol (99%, Sigma-Aldrich, Switzerland) was mixed with D_2O in a ratio of 9:1(v/v) and then 500 μL of the solvent mixture was mixed with 35 mg of 15% SL-hydrogel to achieve an equivalent radical concentration of 6.8 mM. Due to the high viscosity all the samples were loaded directly into sample cup and rapidly frozen in liquid nitrogen. The frozen sample was then transferred in a 5 T custom-designed DNP polarizer²¹ and dynamically polarized at 1 ± 0.05 K by irradiating microwave at 140.18 GHz with a power of 35 mW. The solid-state polarization build-up was monitored by applying a 5° pulse in the RF saddle coil placed around the sample every 5 minutes. Once the polarization reached maximum after about 5 hours, the sample was rapidly dissolved with 5 mL D_2O heated up to 9 bars and transferred within 2 s into a home-built separator/infusion pump located in the isocenter of the in-house 9.4 T scanner. The characteristic decay time of the $1-^{13}C$ signal of *tert*-butanol was measured using a custom-built solenoid probe installed around the separator/infusion pump (see chapter 2). RF pulses with a small flip angle of 5° were applied every 3 s. For comparison, samples prepared with the same solvent mixture were polarized using 33 mM TEMPOL instead of SL-hydrogel, dissolved and measured in the same conditions.

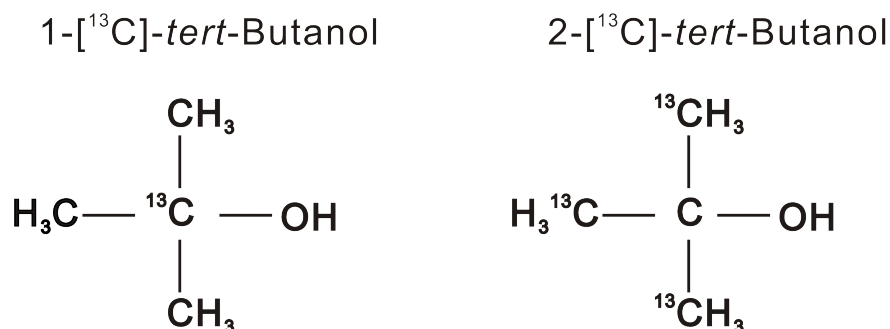


Figure 3.2: Chemical structure and labeling of *tert*-butanol

3.2.3 balanced Steady State Free Precession (b-SSFP) sequence

With the rapid development of the dissolution DNP technique, hyperpolarized ^{13}C magnetic resonance spectroscopic imaging has become more and more interesting for acquiring metabolic information. Although the magnetic field gradient requirements for ^{13}C imaging limits the maximal spatial image resolution by a factor of 4 compared to 1H imaging due to the gyromagnetic ratio difference, the low image background noise, large chemical shift distribution, and the large SNR enhancement provide a solid basis for imaging hyperpolarized ^{13}C -labeled substrates.

Due to the relatively long T_1 of hyperpolarized ^{13}C labeled substrates, different metabolic imaging strategies have been used in practice, which include chemical shift imaging^{22;23}, compressed sensing accelerated imaging²⁴⁻²⁷ and imaging with multiband spectral-spatial

RF excitation pulse²⁸. The first two methods are usually used for single time point image of metabolites as the imaging time is relatively long. The latter one uses selective RF pulse to excite the metabolites of interest with various flip angles so that the SNR of the metabolites can be greatly improved. Another approach is the use of balanced SSFP based sequence with single- or multi-echo readout^{29;30}. Several overviews of imaging sequences used with hyperpolarized substrate can be found elsewhere^{31;32}.

With the extraordinary long *in vitro* and *in vivo* T_1 and T_2 reported for hyperpolarized *tert*-butanol used for *in vivo* brain perfusion experiment³³, b-SSFP method has been chosen for *in vivo* perfusion imaging using radical-free hyperpolarized ^{13}C -labeled *tert*-butanol. The b-SSFP sequence was prepared by modifying a standard 3D gradient echo (GE3D) sequence by adding a preparation pulse with a flip angle of $\alpha/2$ and $\text{TR}/2$ away from the first excitation pulse with a flip angle of α , alternating the phase of the excitation pulses for each TR (α and $-\alpha$), and balancing all the gradients after the readout (see figure 3.3). The main purpose of adding a preparation pulse was to directly bring the magnetization close to its steady state position and thus strongly reduce the magnetization fluctuations caused by the upcoming excitation pulses³⁴. The balanced gradient refocuses the spins back together so that the net transverse magnetization was maximized and recycled in the beginning of each TR as opposed to conventional gradient echo sequence. In order to reduce the RF depletion, after the whole 3D image acquisition a flip back pulse with a flip angle of $\alpha/2$ was added so that the magnetization can be preserved in the Z direction. The *in vivo* images were acquired using the modified b-SSFP sequence ($\alpha = 60^\circ$ FA, 5 mm slice thickness, $\text{TR}/\text{TE} = 10/5$ ms, axial FOV: $30 \times 30 \times 15 \text{ mm}^3$, $64 \times 64 \times 2$ matrix).

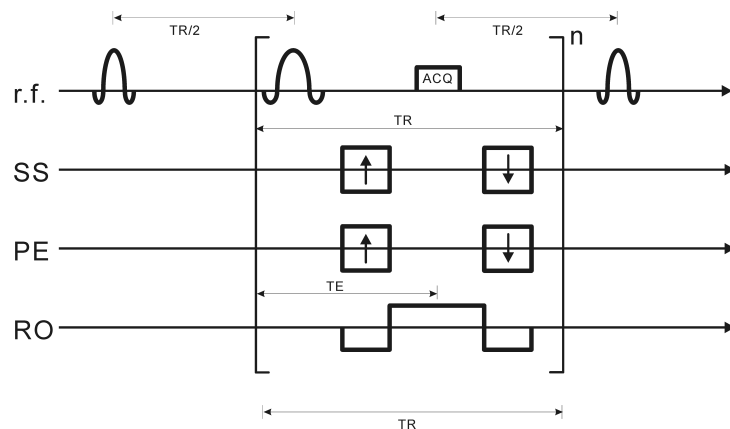


Figure 3.3: b-SSFP sequence based on a 3D gradient echo sequence with a $\alpha/2$ preparation pulse.

3.3 Results

The characteristic ^{13}C solid-state build-up time constant was measured to be 5600 ± 290 s in samples ($n=2$) polarized with SL-hydrogel matrices. The solid-state enhancement was 20 ± 1 for all samples, corresponding to a room-temperature liquid-state enhancement of 6000 ± 300 . The ^{13}C longitudinal relaxation time of both ^{13}C labeling (see figure 3.2) was deduced from the decay of the signal as a function of time (see figure 3.4). The $[1-^{13}\text{C}] T_1$ of 112 ± 2 s and $[2-^{13}\text{C}] T_1$ of 28 ± 1 s was determined for natural abundance *tert*-butanol polarized with the SL-hydrogel. For comparison, samples containing TEMPO radicals were polarized (τ_{Buildup} time of 2200 s) and the dissolution results showed a much shorter $[1-^{13}\text{C}] T_1$ of 29 ± 0.1 s (not shown here).

To test the b-SSFP sequence image series of the separator/infusion pump were taken after the hyperpolarized $[1-^{13}\text{C}]$ acetate solution was transferred into the pump (see figure 3.5). A maximum image SNR of 120 was detected. Strong banding artifacts were observed in the image in addition.

3.4 Discussion

The fact that the ^{13}C polarization buildup in *tert*-butanol samples prepared with SL-hydrogel was much slower than in the samples prepared with nitroxyl radicals can be explained by the fact that the radical concentration was suboptimal and that the ^{13}C spin concentration was low (~ 0.1 M). The usage of ^{13}C -labeled *tert*-butanol should increase the polarization speed.

A large T_1 difference between $[1-^{13}\text{C}]$ - and $[2-^{13}\text{C}]$ - d_{10} -*tert*-butanol measured in the DNP experiments (shown in 3.4) was observed. To explain this the dipolar interaction of C-H bond in the methyl group of *tert*-butanol cannot be neglected. The $[1-^{13}\text{C}] T_1$ of d_{10} -*tert*-butanol was also measured in thermally polarized (degassed and non-degassed) 9:1 d_{10} -*tert*-butanol / D_2O (v/v) samples in a high-resolution 9.4T (Bruker) system using a saturation recovery pulse sequence (see figure 1.9). The long T_1 s acquired from the high-resolution NMR measurements not only confirmed that the solution localized in the infusion/separator pump and ready to be infused is free of stable radical, but also demonstrated that the solution is free of any paramagnetic species and in particular dissolved oxygen in the solution.

The choice of *tert*-butanol for testing ^{13}C polarization was made by considering both the perspectives of *in vivo* applications and the good compatibility with the hydrogel. Note that the hydrogel collapses if mixed with salt even at very low concentration. Due to the spin labeling with nitroxyl radicals and their instability in low pH solutions, the typical pure acids used in DNP applications such as pyruvic acid are not suitable for the hydrogel sample preparation. Taking all these considerations into account, our current method is only suitable with alcohols as substrate. Similar experiments were also performed using d_6 -EtOD. An *in vitro* $[1-^{13}\text{C}] T_1$ of 90 s was measured and fit to the T_1 value measured with degassed d_6 -EtOD in high

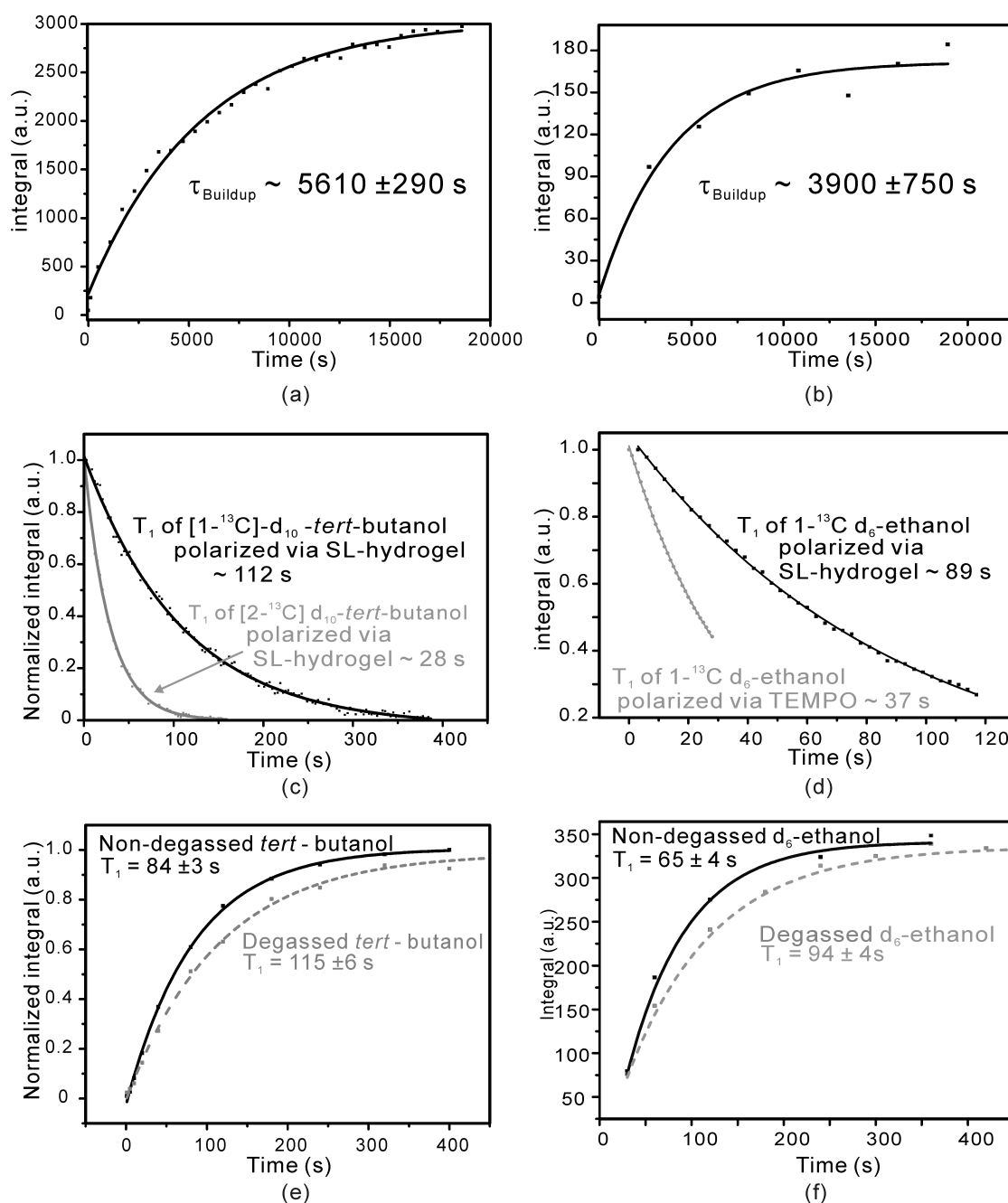


Figure 3.4: (a) Low temperature (1 K) buildup of ^{13}C polarization signal from natural ^{13}C abundance d_{10} -butanol; (b) Low temperature (1 K) buildup of ^{13}C polarization signal from natural ^{13}C abundance d_6 -ethanol; (c) *in vitro* relaxation signal of hyperpolarized $[1-^{13}\text{C}]$ (black) and $[2-^{13}\text{C}]$ (grey) of d_{10} -butanol using hydrogel preparation; (d) *in vitro* relaxation signal of hyperpolarized $[1-^{13}\text{C}]$ d_6 -ethanol using hydrogel preparation (black) and TEMPO preparation (grey); T_1 measurements at 25°C using saturation recovery of d_{10} -*tert*-butanol (e) and d_6 -ethanol (f) in D_2O solute with degassing shows that the hyperpolarized solutions was free of paramagnetic impurities.

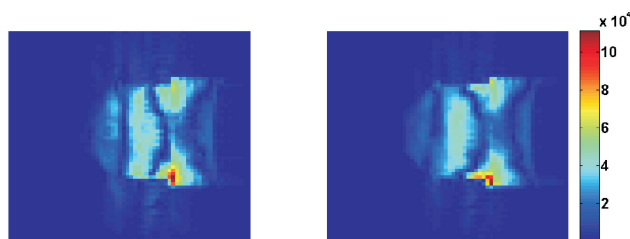


Figure 3.5: ^{13}C images of separator/infusion pump taken by b-SSFP sequence. Strong banding artifacts were observed in the images.

resolution NMR at the same magnetic field (see figure 3.4). One of the advantages of ethanol lies in the fact that it can be dissolved at relatively low temperature since ethanol has a low melting point of -90°C . Mixture of ethanol and water can thus be easily melt at temperature close to room-temperature. A dissolution pressure of 8 bars allowed for recollection and reuse of the SL-hydrogel.

The inhomogeneous ^{13}C signal distribution in the images detected by b-SSFP sequence was mainly originated from the inhomogeneous B_1 field in the vertical direction created by the ^{13}C solenoid coil on the pump. The observed strong banding artifacts is known for b-SSFP sequence since b-SSFP sequence is very sensitive to the T_2^* , or the magnetic field inhomogeneity in other words. This effect is especially strong in ultra high magnetic field. To reduce the banding effect in the DNP-enhanced MRI it is suggested to have a $\alpha/2$ pulse at the end of readout such that the spins could be flipped back to Z direction and thus the images would be more T_2 sensitive instead of T_2^* sensitive. The preliminary test of the b-SSFP sequence contained a lot of information which could help for improving the sequence performance and more tests have been scheduled for preparing the imaging experiments involved with SL-hydrogel.

3.5 Conclusion

We demonstrated that spin-labeled thermoresponsive hydrogel allows for producing radical-free hyperpolarized solutions via dissolution DNP. This method has a high potential for future clinical applications of DNP since it not only leads to reduce polarization losses but it also directly solve the question of toxicity linked to the presence of radicals in the hyperpolarized solutions. We applied this method to hyperpolarize ^{13}C -labeled *tert*-butanol which has been recently shown to be a promising contrast agent for *in vivo* perfusion imaging³³.

References

- [1] J. H. Ardenkjaer-Larsen, B. Fridlund, A. Gram, G. Hansson, L. Hansson, M. H. Lerche, R. Servin, M. Thaning, and K. Golman. Increase in signal-to-noise ratio of > 10,000 times in liquid-state nmr. *Proceedings of the National Academy of Sciences of the United States of America*, 100(18):10158–10163, 2003.
- [2] J. H. Ardenkjaer-Larsen, S. Macholl, and H. Johannesson. Dynamic nuclear polarization with trityls at 1.2 k. *Applied Magnetic Resonance*, 34(3-4):509–522, 2008.
- [3] H. Johannesson, S. Macholl, and J. H. Ardenkjaer-Larsen. Dynamic nuclear polarization of [1-c-13]pyruvic acid at 4.6 tesla. *Journal of Magnetic Resonance*, 197(2):167–175, 2009.
- [4] S. E. Day, M. I. Kettunen, F. A. Gallagher, D. E. Hu, M. Lerche, J. Wolber, K. Golman, J. H. Ardenkjaer-Larsen, and K. M. Brindle. Detecting tumor response to treatment using hyperpolarized 13c magnetic resonance imaging and spectroscopy. *Nat Med*, 13(11):1382–7, 2007.
- [5] F. A. Gallagher, M. I. Kettunen, and K. M. Brindle. Biomedical applications of hyperpolarized (13)c magnetic resonance imaging. *Progress in Nuclear Magnetic Resonance Spectroscopy*, 55(4):285–295, 2009.
- [6] J. H. Ardenkjaer-Larsen, A. M. Leach, N. Clarke, J. Urbahn, D. Anderson, and T. W. Skloss. Dynamic nuclear polarization polarizer for sterile use intent. *Nmr in Biomedicine*, 24(8):927–932, 2011.
- [7] M. C. Krishna, S. English, K. Yamada, J. Yoo, R. Murugesan, N. Devasahayam, J. A. Cook, K. Golman, J. H. Ardenkjaer-Larsen, S. Subramanian, and J. B. Mitchell. Overhauser enhanced magnetic resonance imaging for tumor oximetry: Coregistration of tumor anatomy and tissue oxygen concentration. *Proceedings of the National Academy of Sciences of the United States of America*, 99(4):2216–2221, 2002.
- [8] M. Pluckthun, C. Bradtke, H. Dutz, R. Gehring, S. Goertz, J. Harmsen, P. Kingsberry, W. Meyer, and G. Reicherz. Polarization measurements of tempo-doped butanol targets. *Nuclear Instruments & Methods in Physics Research Section a-Accelerators Spectrometers Detectors and Associated Equipment*, 400(1):133–136, 1997.
- [9] A. Comment, S. Jannin, J. N. Hyacinthe, P. Mieville, R. Sarkar, P. Ahuja, P. R. Vasos, X. Montet, F. Lazeyras, J. P. Vallee, P. Hautle, J. A. Konter, B. van den Brandt, J. P. Ansermet, R. Gruetter, and G. Bodenhausen. Hyperpolarizing gases via dynamic nuclear polarization and sublimation. *Physical Review Letters*, 105(1):018104, 2010.
- [10] A. B. Barnes, G. De Paepe, P. C. A. van der Wel, K. N. Hu, C. G. Joo, V. S. Bajaj, M. L. Mak-Jurkauskas, J. R. Sirigiri, J. Herzfeld, R. J. Temkin, and R. G. Griffin. High-field dynamic nuclear polarization for solid and solution biological nmr. *Applied Magnetic Resonance*, 34(3-4):237–263, 2008.
- [11] R. B. van Heeswijk, K. Uffmann, A. Comment, F. Kurdzesau, C. Perazzolo, C. Cudalbu, S. Jannin, J. A. Konter, P. Hautle, B. van den Brandt, G. Navon, J. J. van der Klink, and R. Gruetter. Hyperpolarized lithium-6 as a sensor of nanomolar contrast agents. *Magn Reson Med*, 61(6):1489–93, 2009.
- [12] C. Cudalbu, A. Comment, F. Kurdzesau, R. B. van Heeswijk, K. Uffmann, S. Jannin, V. Denisov, D. Kirik, and R. Gruetter. Feasibility of in vivo 15n mrs detection of hyperpolarized 15n labeled choline in rats. *Physical Chemistry Chemical Physics*, 12(22):5818–23, 2010.
- [13] M. Mishkovsky, A. Comment, and R. Gruetter. In vivo detection of brain krebs cycle intermediate by hyperpolarized magnetic resonance. *J Cereb Blood Flow Metab(accepted)*, 2012.
- [14] S. Goertz, C. Bradtke, H. Dutz, R. Gehring, W. Meyer, M. Pluckthun, G. Reicherz, K. Runkel, and A. Thomas. Investigations in high-temperature irradiated (lih)-li-6,7 and (lid)-li-6, its dynamic nuclear-polarization and radiation-resistance. *Nuclear Instruments & Methods in Physics Research Section a-Accelerators Spectrometers Detectors and Associated Equipment*, 356(1):20–28, 1995.

Chapter 3. Producing radical-free hyperpolarized solutions for *in vivo* MR

- [15] S. T. Goertz, J. Harmsen, J. Heckmann, C. Hess, W. Meyer, E. Radtke, and G. Reicherz. Highest polarizations in deuterated compounds. *Nuclear Instruments & Methods in Physics Research Section a-Accelerators Spectrometers Detectors and Associated Equipment*, 526(1-2):43–52, 2004.
- [16] T. Kumada, Y. Noda, T. Hashimoto, and S. Koizumi. Dynamic nuclear polarization study of uv-irradiated butanol for hyperpolarized liquid nmr. *Journal of Magnetic Resonance*, 201(2):115–120, 2009.
- [17] E. R. McCarney and S. Han. Spin-labeled gel for the production of radical-free dynamic nuclear polarization enhanced molecules for nmr spectroscopy and imaging. *Journal of Magnetic Resonance*, 190(2):307–15, 2008.
- [18] B. C. Dollmann, A. L. Kleschyov, V. Sen, V. Golubev, L. M. Schreiber, H. W. Spiess, K. Munnemann, and D. Hinderberger. Spin-labeled heparins as polarizing agents for dynamic nuclear polarization. *Chemphyschem*, 11(17):3656–63, 2010.
- [19] B. C. Dollmann, M. J. Junk, M. Drechsler, H. W. Spiess, D. Hinderberger, and K. Munnemann. Thermoresponsive, spin-labeled hydrogels as separable dnp polarizing agents. *Physical Chemistry Chemical Physics*, 12(22):5879–82, 2010.
- [20] Matthias J N. Junk. Thermoresponsive spin-labeled hydrogels as separable dnp polarizing agents. In *Assessing the Functional Structure of Molecular Transporters by EPR Spectroscopy*, Springer Theses, pages 133–148. Springer Berlin Heidelberg, 2012.
- [21] A. Comment, B. van den Brandt, K. Uffmann, F. Kurdzesau, S. Jannin, J. A. Konter, P. Hautle, W. T. Wenckebach, R. Gruetter, and J. J. van der Klink. Principles of operation of a dnp prepolarizer coupled to a rodent mri scanner. *Applied Magnetic Resonance*, 34(3-4):313–319, 2008.
- [22] K. Golman, R. in't Zandt, and M. Thaning. Real-time metabolic imaging. *Proceedings of the National Academy of Sciences of the United States of America*, 103(30):11270–11275, 2006.
- [23] Alessandra Flori, Francesca Frijia, Vincenzo Lionetti, JanH Ardenkjaer-Larsen, Vincenzo Positano, Giulio Giovannetti, RolfF Schulte, Florian Wiesinger, FabioA Recchia, Luigi Landini, MariaF Santarelli, Massimo Lombardi, and Luca Menichetti. Dnp methods for cardiac metabolic imaging with hyperpolarized [1-13c]pyruvate large dose injection in pigs. *Applied Magnetic Resonance*, 43(1-2):299–310, 2012.
- [24] P. E. Z. Larson, R. Bok, A. B. Kerr, M. Lustig, S. Hu, A. P. Chen, S. J. Nelson, J. M. Pauly, J. Kurhanewicz, and D. B. Vigneron. Investigation of tumor hyperpolarized [1-c-13]-pyruvate dynamics using time-resolved multiband rf excitation echo-planar mrsi. *Magnetic Resonance in Medicine*, 63(3):582–591, 2010.
- [25] S. Hu, M. Lustig, A. P. Chen, J. Crane, A. Kerr, D. A. C. Kelley, R. Hurd, J. Kurhanewicz, S. J. Nelson, J. M. Pauly, and D. B. Vigneron. Compressed sensing for resolution enhancement of hyperpolarized c-13 flyback 3d-mrsi. *Journal of Magnetic Resonance*, 192(2):258–264, 2008.
- [26] M. Lustig, D. Donoho, and J. M. Pauly. Sparse mri: The application of compressed sensing for rapid mr imaging. *Magnetic Resonance in Medicine*, 58(6):1182–1195, 2007.
- [27] P. E. Z. Larson, S. Hu, M. Lustig, A. B. Kerr, S. J. Nelson, J. Kurhanewicz, J. M. Pauly, and D. B. Vigneron. Fast dynamic 3d mr spectroscopic imaging with compressed sensing and multiband excitation pulses for hyperpolarized c-13 studies. *Magnetic Resonance in Medicine*, 65(3):610–619, 2011.
- [28] P. E. Z. Larson, A. B. Kerr, A. P. Chen, M. S. Lustig, M. L. Zierhut, S. Hu, C. H. Cunningham, J. M. Pauly, J. Kurhanewicz, and D. B. Vigneron. Multiband excitation pulses for hyperpolarized c-13 dynamic chemical-shift imaging. *Journal of Magnetic Resonance*, 194(1):121–127, 2008.
- [29] J. Svensson, S. Mansson, E. Johansson, J. S. Petersson, and L. E. Olsson. Hyperpolarized c-13 mr angiography using truefisp. *Magnetic Resonance in Medicine*, 50(2):256–262, 2003.
- [30] J. Leupold, O. Wieben, S. Mansson, O. Speck, K. Scheffler, J. S. Petersson, and J. Hennig. Fast chemical shift mapping with multiecho balanced ssfp. *Magnetic Resonance Materials in Physics Biology and Medicine*, 19(5):267–273, 2006.

- [31] R. E. Hurd, Y. F. Yen, A. Chen, and J. H. Ardenkjaer-Larsen. Hyperpolarized ^{13}C metabolic imaging using dissolution dynamic nuclear polarization. *Journal of Magnetic Resonance Imaging*, 36(6):1314–1328, 2012.
- [32] K. M. Brindle, S. E. Bohndiek, F. A. Gallagher, and M. I. Kettunen. Tumor imaging using hyperpolarized ^{13}C magnetic resonance. *Magnetic Resonance in Medicine*, 66(2):505–519, 2011.
- [33] A. K. Grant, E. Vinogradov, X. E. Wang, R. E. Lenkinski, and D. C. Alsop. Perfusion imaging with a freely diffusible hyperpolarized contrast agent. *Magnetic Resonance in Medicine*, 66(3):746–755, 2011.
- [34] K. Scheffler and S. Lehnhardt. Principles and applications of balanced ssfp techniques. *European Radiology*, 13(11):2409–2418, 2003.

4 Preliminary results on ^{15}N and ^{89}Y labeled tracers for *in vivo* hyperpolarized NMR

Abstract

Extraordinarily long T_1 's were measured in molecules containing either a ^{15}N -labeled quaternary ammonium ion or a ^{89}Y nuclear spin. After having optimized the preparation of hyperpolarized ^{15}N -labeled choline and hyperpolarized $^{89}\text{Y}(\text{DOTA})^-$ complexes by performing solid-state DNP studies and *in vitro* measurements, *in vivo* measurements were carried out in the rat brain and kidney. A non-negligible amount of choline was taken up by the brain during the time window of the experiment showing that it should be possible to detect its downstream metabolites and possibly use hyperpolarized ^{15}N -choline as a biomarker for cancer research. Bio-compatible hyperpolarized ^{89}Y solutions for *in vivo* experiments were prepared using $^{89}\text{Y}(\text{DOTA})^-$ complexes and it was shown for the first time that ^{89}Y can be detected *in vivo*.

4.1 Introduction

So far, most *in vivo* studies performed with DNP-enhanced solutions have been done using ^{13}C -labeled molecules, and in particular with ^{13}C -labeled pyruvate. Carboxyl ^{13}C s usually have a long longitudinal relaxation time, even *in vivo* (about 30-50 seconds). We aimed at implementing *in vivo* hyperpolarized NMR experiments with substrates labeled with very long T_1 nuclear spins.

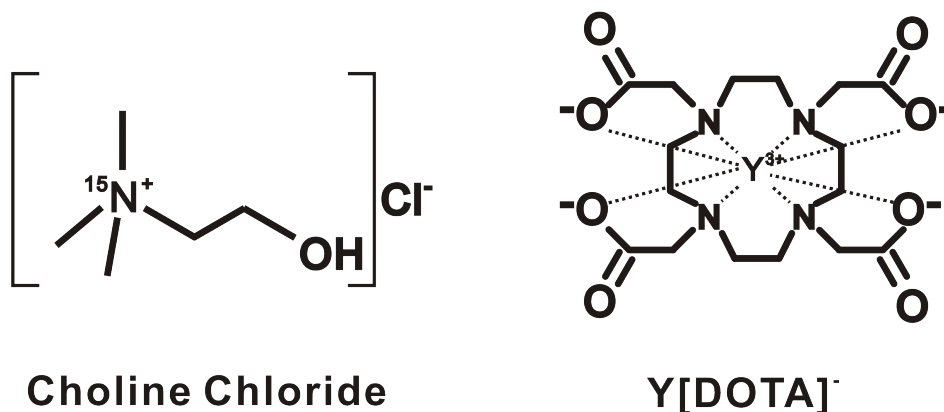


Figure 4.1: Chemical structure of choline chloride (left) and $\text{Y}[\text{DOTA}]^-$ (right).

Nitrogen is a common and essential element in biological tissues that is found in amino acid and thus proteins and in deoxyribonucleic and ribonucleic acids. Both nitrogen isotopes are NMR active but the most abundant, ^{14}N , has a spin 1 and cannot be highly polarized due to the large line width at higher magnetic field. ^{15}N , a spin-1/2 element with a natural abundance of 0.4%, can have an extremely longitudinal relaxation time (T_1), up to several hundreds of seconds, in room-temperature liquids if it is not directly bound to protons. It is the case in molecules containing a quaternary ammonium ion like carnitine and choline^{1;2}. These molecules are suitable for hyperpolarized NMR and can be used as substrates to study the dynamics of essential metabolic pathways. It has been observed that in many cancer cells the total choline level increases. Choline (see figure 4.1) is thus an important biomarker that is attractive for tumor diagnosis and treatment response via MRS³. Already several *in vitro* DNP experiments have been performed with ^{15}N -choline in cell culture^{4;5}. We know from previous studies that hyperpolarized ^{15}N -choline can be detected *in vivo* and that the observed T_1 is on the order of 100 s⁶. The signal was detected in the rat brain but no metabolites could be detected and improved polarization levels would be greatly beneficial for such studies. One of the open issues was whether the observed ^{15}N choline signal was originating from blood or from brain tissue. In the first section of this chapter, an *in vivo* protocol was designed to investigate the spatial origin of hyperpolarized ^{15}N choline signal in the rat brain by selectively acquiring localized spectra from different spatial locations in the brain.

The yttrium isotope ^{89}Y has a spin-1/2 and a natural abundance of 100%. Its NMR

sensitivity is unfortunately quite low since ^{89}Y has a very small gyromagnetic ratio, about 20 times smaller than proton. It however turns out that ^{89}Y in Y^{3+} complexes also has an unusually long longitudinal relaxation time (up to about 500s in *ex vivo* $\text{Y}(\text{DOTA})^{-7}$) (see figure 4.1). One of its attractive features is that it has the same valence as gadolinium and can therefore substitute Gd^{3+} in FDA-approved contrast agents such as $\text{Gd}(\text{DOTA})^{-}$ (the radioactive yttrium isotope ^{90}Y based complex $^{90}\text{Y}(\text{DOTATOC})$ is also a FDA-proven PET tracer that is being tested for detecting somatostatin receptor positive tumor⁸). Moreover, the resonance of ^{89}Y is quite sensitive to its surroundings through its large chemical shift range, and could hence bring information on the local environment of the hyperpolarized molecules. Various Y^{3+} complexes have been tested by our collaborators from the UT Southwestern Medical Center (Dallas, Texas), which is one of the world leading MRI research centers in the field of contrast agents⁷, and they designed $\text{Y}(\text{DOTA})^{-}$ probes with a very large dependence of the pH on the ^{89}Y chemical shift⁹. Recently, ^{89}Y signal enhancement over 60,000 were reported for optimized samples containing $\text{Y}(\text{DOTA})^{-}$ complexes¹⁰. These results demonstrate the great potential of these complexes for probing the pH of diseased tissues *in vivo*.

In this chapter, preliminary DNP and hyperpolarized MR experiments including *in vivo* results obtained with ^{15}N -labeled choline and $^{89}\text{Y}(\text{DOTA})^{-}$ will be presented.

4.2 ^{15}N choline

The samples were prepared in the form of frozen beads from a 6M ^{15}N labeled choline chloride solution in $\text{D}_2\text{O}/\text{d}_8$ – glycerol 2:3(v/v) doped with 50mM TEMPO radicals. A dozen of beads ($\sim 50\mu\text{L}$) were polarized in the 5T polarizer at 140.18GHz and $1.05 \pm 0.05\text{K}$. The DNP parameters such as the microwave power and frequency were kept identical to those used to polarize ^{13}C -labeled substrates (this was motivated by the fact that the ESR linewidth of TEMPO is much larger than the nuclear resonance frequency of ^{15}N). A buildup time constant τ_{Buildup} for ^{15}N at 5 T of 3812 ± 55 s was determined by monitoring the NMR signal every 10 minutes with calibrated 10° RF pulses (see figure 4.2) and a maximal ^{15}N solid-state polarization of about 5% was achieved after 3.5 hours of microwave irradiation. Following dissolution, the concentration of ^{15}N choline in the hyperpolarized aqueous solutions was around 90 mM, as confirmed by high-resolution NMR measurements performed subsequently.

A liquid-state ^{15}N polarization level of 5% was determined through *in vitro* experiments performed on hyperpolarized choline solutions injected into a phantom placed underneath the ^{15}N surface coil used for *in vivo* experiments. Since all nuclear spins should reach the same spin temperature at the end of the solid-state DNP process, such polarization level is consistent with the typical maximum ^{13}C polarization we observed taking into account the fact that the gyromagnetic ratio of ^{15}N is 2.5 times lower than the one of ^{13}C .

Following the preliminary *in vitro* measurements, ^{15}N -labeled choline chloride samples were used for *in vivo* localized ^{15}N MRS experiments to confirm that the major contribution to

Chapter 4. Preliminary results on ^{15}N and ^{89}Y labeled tracers for *in vivo* hyperpolarized NMR

the signal measured in the rat brain was coming from brain tissue rather than from the blood pool. Two voxels were selected on the proton anatomical images of the rat brain, one with a size of $5 \times 8 \times 8\text{mm}^3$ ($n=5$) and the other with a size of $3 \times 4 \times 6\text{mm}^3$ ($n=2$). The major brain blood vessels were excluded from the voxels of interest. After having carefully homogenized the static magnetic field in the two voxels using the shim coils and the FASTESTMAP protocol, a bolus of 2 mL of 90 mM choline chloride solution was injected in one of the rat femoral veins. The signal localization was done using an outer volume suppression sequence (SIRENE) which was calibrated with a reference bubble containing ^{15}N -labeled urea and placed on top of the surface coil to avoid signal contamination from the surrounding tissue. *In vivo* hyperpolarized signals in the rat brain were acquired with a 3 ms BIR4.10 pulse and a repetition time of 3 s.

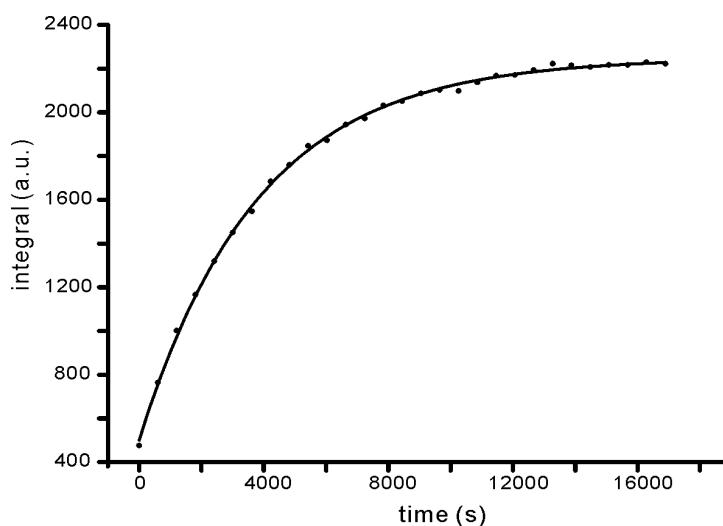


Figure 4.2: Buildup of polarized ^{15}N -choline signal.

As expected the *in vivo* SNR measured in the smaller voxels were lower than the ones measured in the larger voxels. In all measurements, the localized characteristic signal decay exhibited a bi-exponential distribution composed of a very fast component ($11 \pm 5\text{s}$) dominating the signal during the first ~ 10 seconds superimposed to a slowly decaying signal ($83 \pm 12\text{s}$). This observation is consistent with the results previously measured in a similar *in vivo* study performed using a 3.35 T polarizer⁶. The fast decaying signal was assigned to the contribution of the blood pool (small capillaries) to the signal and the slowly decaying to the signal originating from the brain. Unfortunately, a precise determination of tissue choline uptake could not be estimated from the data so far. These results, however, confirm that a non-negligible amount of choline was taken up by the brain during the time window of the experiment and that it should be possible to detect downstream metabolites and possibly use hyperpolarized ^{15}N -choline as a biomarker for cancer research.

4.3 ^{89}Y chloride and DOTA

Yttrium DNP experiments were first performed with water-soluble yttrium chloride, YCl_3 , in order to determine the appropriate polarization parameters. Due to its strong hydrophilic properties, yttrium chloride (Sigma-Aldrich, Switzerland) was rapidly mixed under the ventilated laboratory hood with a $\text{D}_2\text{O}/\text{d}_6 - \text{EtOD}$ 2:1(v/v) solvent mixture doped with 50 mM TEMPO radicals. To prevent the formation of yttrium hydroxide, a few drops of 1M hydrochloric acid (HCl) were added into the solution. The final ^{89}Y concentration of the DNP sample was calculated to be around 2.5 M. For solid-state DNP experiments, a volume of 350 μL of the yttrium chloride solution was carefully introduced into a sample cup and then quickly frozen in liquid nitrogen as a block instead of the standard beads to avoid toxicity issues. The sample was then loaded and polarized in the 5 T polarizer at 140.18 GHz and 1.05 ± 0.05 K. The build-up of the polarized NMR signal detected at 10.40 MHz was monitored by applying a 25° pulse every 45 minutes (a low-frequency short-ringing time coil had to be designed to performed these measurements). The build-up time constant was determined to be around 16'000 s, which is almost 8 times longer than the standard build-up times measured on ^{13}C . The solid-state yttrium signal consisted of a sharp single resonance with a FWHM of 1.5 kHz, a linewidth that is only one tenth of the average width observed on ^{13}C . This implies that the solid-state ^{89}Y T_2 in these samples is unusually long (T_1 was also prohibitively long to be measured in a reasonable time at 5 T and 1 K).

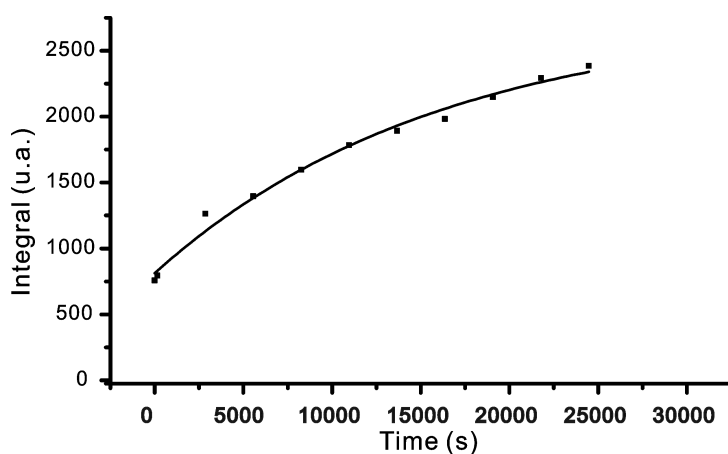


Figure 4.3: Buildup of polarized ^{89}Y signal

Bio-compatible hyperpolarized ^{89}Y solutions for *in vivo* experiments were prepared using $^{89}\text{Y}[\text{DOTA}]^-$ complexes provided by our collaborators from the UT Southwestern Medical Center (Dallas, Texas). The concentration of the initial frozen solution was 0.183M in $\text{D}_2\text{O}/\text{d}_6 - \text{EtOD}$ 2:1(v/v). To accelerate the polarization process, the radical concentration (TEMPO) was increased from our standard value of 33 mM to 50 mM. Frozen beads were polarized and dissolved using the standard protocol used for ^{13}C -labeled samples (see chapter 2). A dedicated dual $^1\text{H}/^{89}\text{Y}$ probe with a 13mm diameter ^{89}Y surface coil based on the design described in chapter 5 was designed and built for this study. A hollow glass sphere reference

Chapter 4. Preliminary results on ^{15}N and ^{89}Y labeled tracers for *in vivo* hyperpolarized NMR

bubble containing 120 μL of saturated YCl_3 solution and doped with 5 mM of Dotarem contrast agent to reduce the T_1 of the solution to about 10 s was used as a reference for the ^{89}Y signal. The pulses were calibrated using the reference and a phantom containing yttrium chloride placed underneath the surface coil.

In vivo experiments were performed by placing the surface coil on the rat right flank, just above the kidney (see figure 4.4). Following dissolution, 2.4 mL of hyperpolarized $^{89}\text{Y}[\text{DOTA}]^-$ solution was injected into the rat femoral vein using the protocol described in chapter 2. Signal acquisition started 1s after the end of the injection and a series of consecutive ^{89}Y spectra were acquired with a repetition time of 14 s using adiabatic BIR4 10° pulses. The ^{89}Y enhancement was determined to be at least 3250 by comparing the hyperpolarized signal to accumulated thermal equilibrium signals. The *in vivo* signal decay measured in the rat kidney was around $50 \pm 10\text{s}$, which is shorter than the T_1 values measured *in vitro* (around 70 s) and much shorter than the T_1 of pure YCl_3 (typically 600 s). A possible explanation for this discrepancy could be the residual radical concentration accumulated in the kidney which leads to a dramatically shortened T_1 . Another possibility is that since the Q value of the coil was very large, a small change of the coil loading during the experiment, possibly due to animal motion, led to a change in the coil performance.

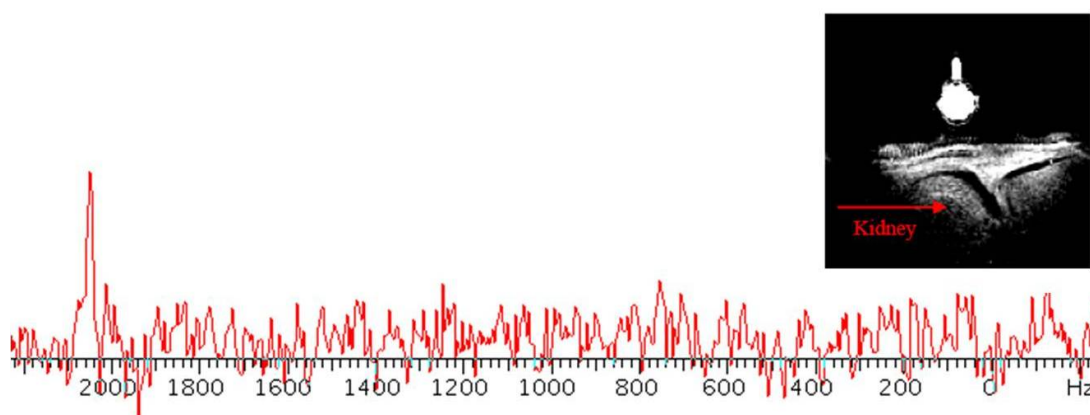


Figure 4.4: *In vivo* ^{89}Y spectrum measured in the rat kidney area following a 10° adiabatic pulse (left) and decay of the hyperpolarized ^{89}Y signal in rat kidney (right). The measured *in vivo* T_1 is much shorter than the one measured *in vitro*. We suspect that it is because of the radicals which accumulate in the kidney and shorten T_1 .

Although many improvements will have to be made to be able to perform pH imaging using hyperpolarized $^{89}\text{Y}[\text{DOTA}]^-$, these preliminary results showed for the first time that ^{89}Y can be detected *in vivo*.

References

- [1] C. Gabellieri, S. Reynolds, A. Lavie, G. S. Payne, M. O. Leach, and T. R. Eykyn. Therapeutic target metabolism observed using hyperpolarized ^{15}N choline. *J Am Chem Soc*, 130(14):4598–9, 2008.
- [2] R. Sarkar, A. Comment, P. R. Vasos, S. Jannin, R. Gruetter, G. Bodenhausen, H. Hall, D. Kirik, and V. P. Denisov. Proton nmr of n- 15 -choline metabolites enhanced by dynamic nuclear polarization. *Journal of the American Chemical Society*, 131(44):16014–+, 2009.
- [3] K. Glunde and N. J. Serkova. Therapeutic targets and biomarkers identified in cancer choline phospholipid metabolism. *Pharmacogenomics*, 7(7):1109–23, 2006.
- [4] H. Allouche-Arnon, M. H. Lerche, M. Karlsson, R. E. Lenkinski, and R. Katz-Brull. Deuteration of a molecular probe for dnp hyperpolarization—a new approach and validation for choline chloride. *Contrast Media Mol Imaging*, 6(6):499–506, 2011.
- [5] H. Allouche-Arnon, A. Gamliel, C. M. Barzilay, R. Nalbandian, J. M. Gomori, M. Karlsson, M. H. Lerche, and R. Katz-Brull. A hyperpolarized choline molecular probe for monitoring acetylcholine synthesis. *Contrast Media Mol Imaging*, 6(3):139–47, 2011.
- [6] C. Cudalbu, A. Comment, F. Kurdzesau, R. B. van Heeswijk, K. Uffmann, S. Jannin, V. Denisov, D. Kirik, and R. Gruetter. Feasibility of in vivo ^{15}N mrs detection of hyperpolarized ^{15}N labeled choline in rats. *Physical Chemistry Chemical Physics*, 12(22):5818–23, 2010.
- [7] M. E. Merritt, C. Harrison, Z. Kovacs, P. Kshirsagar, C. R. Malloy, and A. D. Sherry. Hyperpolarized γ -89 offers the potential of direct imaging of metal ions in biological systems by magnetic resonance. *Journal of the American Chemical Society*, 129(43):12942–+, 2007.
- [8] M. de Jong, R. Valkema, F. Jamar, L. K. Kvols, D. J. Kwekkeboom, W. A. P. Breeman, W. H. Bakker, C. Smith, S. Pauwels, and E. P. Krenning. Somatostatin receptor-targeted radionuclide therapy of tumors: Preclinical and clinical findings. *Seminars in Nuclear Medicine*, 32(2):133–140, 2002.
- [9] A. K. Jindal, M. E. Merritt, E. H. Suh, C. R. Malloy, A. D. Sherry, and Z. Kovacs. Hyperpolarized γ -89 complexes as ph sensitive nmr probes. *Journal of the American Chemical Society*, 132(6):1784–+, 2010.
- [10] L. Lumata, A. K. Jindal, M. E. Merritt, C. R. Malloy, A. D. Sherry, and Z. Kovacs. Dnp by thermal mixing under optimized conditions yields > 60 000-fold enhancement of γ -89 nmr signal. *Journal of the American Chemical Society*, 133(22):8673–8680, 2011.

5 MR probes for *in vivo* MRS and MRI at ultra high magnetic field

Abstract

An essential feature of MR probes for magnetic resonance spectroscopy and imaging is the ability to generate uniform B_1 excitation in a volume of interest. When the magnetic field strength is increased, leading to an increase in resonance frequency, the constraints on the MR probes size, the sample size and the associated radiation losses caused by conductor elements are higher. In this chapter, concepts and RF designs of custom-designed surface coils and volume coils tested in ultra high magnetic field are produced. Bench tests and imaging obtained with surface coils and birdcage coils operating at 9.4 T and 14.1 T were carried out and analyzed.

Partially adapted from:
Tian Cheng, Jennifer Jung, Arnaud Comment, Hongxia Lei
Arthur W. Magill and Rolf Gruetter
Performance Comparison of Birdcage Coils at 9.4 T and 14.1 T
Manuscript in preparation

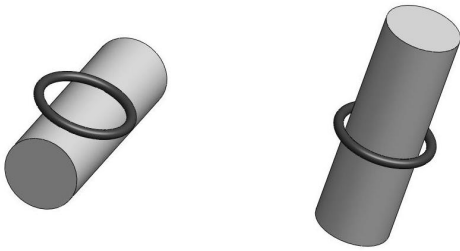


Figure 5.1: An inductive loop (dark gray) positioned as a surface coil (left) or a volume coil (right) to probe the same sample (light gray) with a different geometry.

5.1 Introduction

MRI is one of the most powerful non-invasive biomedical imaging method which plays an increasingly important role in clinical and research environments. To create high resolution anatomical images in a limited time period, RF coils have to be designed and optimized.

The signal-to-noise (SNR) ratio measured by a RF coil is proportional to¹,

$$SNR \propto \frac{B_1 V_S}{\sqrt{P_T T_n}}, \quad (5.1)$$

where B_1 represents the transverse rotating magnetic field, V_S is the effective volume of the sample, P_T is the transmitter power and T_n is the temperature at which the thermal noise is defined. It is obvious that by decreasing the coil temperature the noise is reduced and the SNR will be enhanced. This led to the development of cryocoils often used for room-temperature high-resolution NMR^{2;3}. For given values of P_T , T_n and V_S , the B_1 field generated by a RF coil is the only factor influencing the SNR and therefore determines the sensitivity of a coil as expressed in the reciprocity theorem.

The simplest form of a RF coil is a closed loop tuned to the Larmor frequency of the nuclear spins of interest, ω_0 . Depending on the position of the sample, the coil can be treated as a surface coil or a volume coil, the two common geometries of RF coils used in MRI and MRS (see figure 5.1). The internal volume of a volume coil is usually larger than the sample in order to entirely excite and probe the sample. When the volume of interest is small compared to the sample, the large distance between the coil and the volume of interest as well as the large noise induced by the whole sample and picked up by the coil might strongly reduce the SNR measured by a volume coil. In addition, high excitation energy is necessary due to the larger coil size. A surface coil is usually smaller than the sample itself and is placed in contact or in close proximity with the sample. This configuration leads to larger SNR from the volume of interest.

Images acquired by volume coils are uniform due to the homogeneous B_1 field generated in the coil center and can offer detailed morphological information over the entire sample volume. Solenoid coils were the most common used volume coils for NMR research in the early days. They were used in conjunction with electromagnets because this type of coil is easy to

build and can be oriented such as to have a B_1 field direction orthogonal to main magnetic field B_0 . The most important advantage is that the B_1 field generated in the solenoid coil is relatively strong and homogeneous⁴. With the development of high-field superconducting magnets the solenoid coil was gradually substituted by another type of commonly used volume coil, the saddle coil. The saddle coil is geometrically open and consists in two sets of solenoids creating a magnetic field in the same direction as the Helmholtz coil. Saddle coils are widely used in conjunction with superconducting magnets due to the orthogonality between the B_1 field and the opening of the coil which is convenient for sample loading. But their drawbacks include the B_1 field inhomogeneity generated in the effective volume of the coil and their relatively poor SNR^{4,5}. To improve the SNR associated with volume coils, the focus has been placed on the reduction of the electrical losses, i.e. the reduction of the coil inductance. A good example is the Alderman-Grant (AG) coil, which is similar to the saddle coil and was introduced in high-field MR mainly for solving heating problem created by lossy samples during decoupling⁶. As its coil inductance is low, the AG design is usually used for solid-state ^1H MRS and limited to heteronuclear applications. Apart from the solenoid coil, the saddle coil and the AG coil, the birdcage (BC) coil developed by Hayes et al⁷ initially for low-field MRI is another widely used coil, especially for *in vivo* MRI. Several theoretical analyses were described elsewhere⁸⁻¹⁰ to highlight the different resonance modes and the field homogeneities of the birdcage coil. A great challenge when building birdcage coil for ultra high magnetic field is the low capacitance required for generating high-frequency resonances. Transverse electromagnetic (TEM) coils based on microstrip technology were recently developed to transceive RF signal through shielded microstrips and showed remarkable results for human applications at high magnetic field up to 8 T¹¹⁻¹⁴. Theoretically TEM coils can work at very high frequency, but the complexity of the data acquisition and image reconstruction procedures as well as the compact resonance spectrum at high magnetic field limits the applications for small animal MR research. A common problem of volume coils operating at ultra high magnetic field is the dielectric resonance effect which leads to an inhomogeneous B_1 field in the sample when the sample size is comparable to the wavelength¹⁵, and the radiation losses caused by the coil conductive elements when their size is comparable to the wavelength.

Compared with a volume coil, the B_1 field of a surface coil is highly inhomogeneous and decreases dramatically as distance to the sample increases¹⁶. This characteristics of the surface coil leads to a limited view of the sample in the acquired image. But unlike a volume coil, the sensitivity in the VOI close to a surface coil increases greatly due to a larger B_1 field, larger filling factor and moreover less noise related to the small FOV. Surface coils are mainly used in localized MRS with small animal. To compensate for B_1 inhomogeneity, adiabatic RF pulses are often used in conjunction with surface coils¹⁷.

Single-loop surface coils can also be arranged with some specific geometry as a coil array, usually called phase array coil¹⁸⁻²⁰. To be able to measure the MR signal, all the single-loop elements are inductively or capacitively decoupled by adjusting the overlapping area among them. The main advantage of the phase array coil is the large covered VOI of the sample combined with the high sensitivity associated with the use of surface coils. This property

makes the phase array coil a highly performant receiving coil.

To greatly improve the SNR and reduce power deposition, two linearly polarized coils are positioned orthogonal to each other and driven by currents of same intensity but with 90 degrees phase shift (quadrature-driven mode)^{21;22}. With this arrangement a SNR enhancement of $\sqrt{2}$ is theoretically expected. The main issues related to ultra high magnetic field RF coils, are the low capacitance value needed for tuning the coil and the short wavelength causing more radiation.

In this chapter, surface and volume coils designed and tested for DNP-enhanced MRS and MRI experiments, especially the $^1\text{H}/^{13}\text{C}$ surface coil and the ^1H birdcage coil, will be introduced and discussed.

5.2 Surface coil

As started in the reciprocity theorem²³, the sensitivity of a coil is dependent on the generated B_1 field. The larger the B_1 field, the more sensitive the coil. Assuming that the surface coil has a radius of a , the transverse magnetic field B_1 can be described according to the Biot-Savart law as^{16;24},

$$B_1 = \frac{\mu_0 I}{2} \frac{a^2}{(d^2 + a^2)^{3/2}}, \quad (5.2)$$

where d is the distance along the coil main axis between the loop center and the plan containing the point of interest inside the sample. This formula shows that first, for a constant current I , B_1 field reduces dramatically as the distance to the coil plane increases; second, B_1 field decreases when the loop size a increases; last but not least, with a fixed coil size B_1 field can be enhanced by injecting more currents into the coil, either by using a more powerful RF amplifier or using superconducting wires to reduce the wire resistance at low temperature and therefore increase the coil-driving current²⁵⁻²⁸. Since the thermal noise is proportional to \sqrt{T} , cooling the coil will also reduce the noise. Recently several *in vivo* MRS and MRI applications with cryocoils showed that it is possible to obtain a strong B_1 field and improve the SNR^{29;30}.

Another aspect influencing the RF coil performance is the noise created by the sample. The sample resistance in a circular surface coil can be expressed as,

$$r = g \cdot \omega_0^2 \cdot f(a) \propto \omega_0^2 \cdot a^3, \quad (5.3)$$

where g is the sample resistivity, ω_0 the operating frequency of the scanner, and $f(a)$ is a function related to the coil radius a ($f(a)$ increases as the radius increases)³¹. When the operating frequency increases and the coil size becomes larger, the sample resistance picked up by the surface coil increases and dominates the noise contribution at ultra high magnetic field. After combining the two equations above it is easy to find out that the coil size and current in the coil are the two most important factor influencing the coil performance.

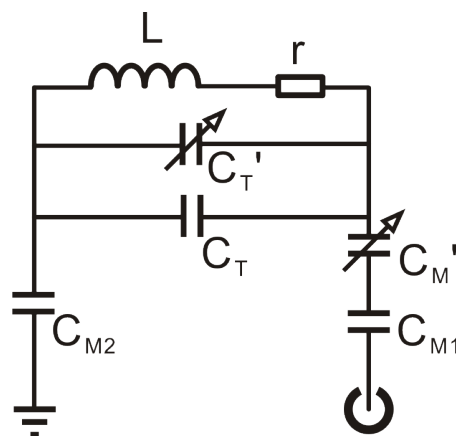


Figure 5.2: Schematics of the ^{13}C surface coil used for small animal MRS experiment.

Table 5.1: Summary of surface coils built for *in vivo* experiments. Unloaded quality factors are shown in parenthesis.

Nuclei I	ν_I [MHz]	C_T [pF]	C_{M1} [pF]	C_{M2} [pF]	Q	$P_{\pi/2}$ [dB]
^1H	400.22	-	2	1	49(65)	46
^{13}C	100.67	6.8	10	6.8	69(86)	46
^{89}Y	19.519	35	10	6.8	169(247)	42

5.2.1 Design of the surface coil

The schematics of a typical surface coil used in this thesis is presented in figure 5.2 where L represents the inductance of the loop, r is the sample loading and the coil intrinsic resistance, C_T and C_M the fixed tuning and matching capacitors, C_T' and C_M' the variable tuning and matching capacitors, respectively. To balance the circuit, matching capacitance is divided into two parts so that electrical impedance is symmetric from both sides³². To effectively tune and match the circuit with selected non-magnetic variable capacitors (NMKJ10HV, Voltronics, USA), the winding of the coil was determined by using C_T with a value close to half of the maximal capacitance of variable tuning capacitors. The capacitor values of all built surface coils are shown in table 5.1.

Surface coils used in experiments were usually equipped with dual channels including both ^1H and another heteronucleus since ^1H was very useful for positioning the sample and decoupling for the heteronucleus. Depending on the requirements of the experiment, one of the two channels can be operated in quadrature mode. Here only the surface coil with single loop ^{13}C and quadrature ^1H will be introduced and for other nuclei the coil can be deduced by analogy.

The circuit structure for three channels (two for ^1H and one for ^{13}C) was designed in EAGLE software (Cadsoft computer GmbH, Germany) and then printed on a PCB board (1.6 mm FR4, 12 μm Cu). A large common ground plate for all three channels was integrated into the board to reduce the influence of eddy currents. To reduce RF power for all channels,

the loops of surface coil were limited to a diameter of 13 mm and ^1H and ^{13}C loops had 1- and 3-turns winding, respectively. Fixed capacitors C_T and C_M for all three channels were determined by tuning and matching the circuits to targeted frequencies: $\nu(^1\text{H}) = 400.2\text{MHz}$ and $\nu(^{13}\text{C}) = 100.7\text{MHz}$ with a -30dB level. To minimize the coupling of the loops two ^1H loops are inductively decoupled by adjusting overlapping area and the angle formed between both loops till the coupling decreases at least to -15dB level.

The quality factor of a coil with equivalent parallel RLC circuit is given by,

$$Q = \frac{r}{\omega_0 L} \quad (5.4)$$

where r is the coil resistance, ω_0 the nuclear frequency and L the loop inductance. Quality factors (also called Q-values) were measured on the bench with and without loading a saline phantom (0.5 M NaCl solution prepared in D_2O) by dividing the central frequency by the bandwidth measured with a network analyzer (4096B, Agilent, USA) at -7 dB after tuning and matching the coil³³. The quality factor of the $^1\text{H}/^{13}\text{C}$ coil with 13 mm diameter is shown in 5.1.

To test the coil performance with adiabatic pulse, a phantom containing 0.2 M [^{13}C] acetate sodium and 0.5 mM Gd^{3+} contrast agent was positioned under the coil. After tuning and matching the coil, the minimum RF power required to reach the plateau in signal intensity was determined by performing unlocalized single pulse acquisition with 3 ms BIR4.90 pulse.

5.2.2 Results

In table 5.1 all the capacitor values, quality factors measured on the bench and calibrated RF power by performing localized MRS with hard pulses for different surface coils are shown. It is known that for a loop with a radius of R , its inductance is proportional to R^2 and its resistance is proportional to R . If the dimensions of the loop are kept unchanged, tuning to higher frequency leads to a drop of the quality factor. This is evidenced by the Q-value change measured with the surface coils (shown in table 5.1). Smaller coils (down to 8 mm diameter) were also developed and tested for *in vivo* mouse experiments. A 60% improvement in unloaded Q-value for ^1H and ^{13}C (to around 90 and 145 respectively) proved that reducing the coil size increases the Q-value. In practice, a compromise should be made between a high Q-value and a large FOV as a function of the experimental requirements. To evaluate the RF coil sensitivity, unloaded Q-values were also measured on the bench. Through comparing the loaded and unloaded Q-values, one can also determine if the resistivity of the RF coil was comparable to the resistivity of the phantom. Therefore, in the practice, a RF coil with a large loaded to unloaded Q-value ratio is preferred.

5.3 Birdcage coil

The birdcage coil was first developed to acquire homogeneous whole body human images at relatively low magnetic field (1.5 T) several decades ago⁷. Since then high-pass (HP) and low-pass (LP) types birdcage coil have already been studied with different theoretical models^{8;34;35} and are widely used in MR research. With the recent advent of ultra high magnetic field magnets the design of HP and LP birdcage coils have become more technically challenging since the proton resonance frequency increases and the required capacitor value decreases. On the other hand, the wavelength of the RF signal becomes shorter in air, and even shorter in biological tissue due to its high dielectric constant, which leads to a bright spot in the middle of the image when the sample size is comparable to the wavelength. This is called the dielectric resonance effect^{15;36;37}. RF radiation losses can also not be neglected anymore due to a comparable conductor length to a fraction of corresponding wavelength (normally $\lambda/20$)²³. Band-pass (BP, also called hybrid) type, a mixture of HP and LP types, has capacitors implemented both on rungs and end rings which practically breaks down the conductor length and becomes an alternative choice for UHF applications^{38;39}. In this study two HP type and one BP type birdcage coils with same dimensions adapted for small animal MRI at 9.4 T and 14.1 T were simulated, constructed and tested both *in vitro* and *in vivo*. After RF power calibration, B_1^+ field mapping and SNR measurements were carried out to characterize the coils. *In vivo* mouse brain images were acquired using all coils and then compared.

5.3.1 Resonance modes of the birdcage coil

Birdcage coils are classified into three different types according to the position of the capacitors and distribution of their resonance mode: HP type when the capacitors are only on the end rings, LP type when the capacitors are only on the rungs and BP type when the capacitors are located on both the end rings and the rungs. To analyze the resonance mode of the birdcage coil with $2n$ rungs, a classic simple way is to treat the birdcage coil as a RF circuit containing $2n$ meshes of lumped elements with a current distribution on the $2n$ rungs in a way of cosine function,

$$I_m = I_0 \cos(\theta_m + \phi), \quad (5.5)$$

where θ_m is the relative angle position of m -th rung and is given by,

$$\theta_m = m\pi/N. \quad (5.6)$$

B_1 field in the center of the coil can be calculated and given by⁴⁰,

$$B_1 = \frac{2\mu_0 I_0}{\pi d} \frac{l}{\sqrt{l^2 + d^2}} \zeta \quad (5.7)$$

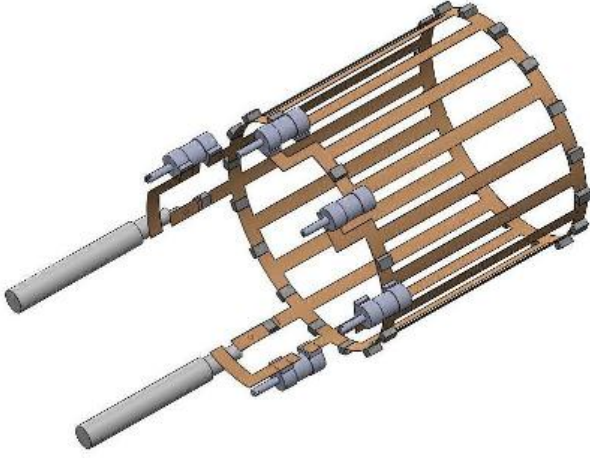


Figure 5.3: HP resonator of the coil with tuning and matching network.

where d and l is the diameter and length of the coil, respectively and ζ is the geometry factor dependent on the number of the rungs. Note that this calculation is performed without considering the return current through the rungs. By applying Kirchhoff law with equation 5.5 and RLC tank circuit equation to all $2n$ cells the resonance frequency of m -th mode is given by,

$$(\omega_m^{HP})^2 = \frac{1}{4LC \sin^2(m\pi/2n)}, m \in (0, 2n - 1) \quad (5.8)$$

for HP birdcage coil and

$$(\omega_m^{LP})^2 = \frac{4 \sin^2(m\pi/2n)}{LC}, m \in (0, 2n - 1) \quad (5.9)$$

for LP birdcage coil. A birdcage coil with $2n$ rungs has $n + 1$ modes in total and the distribution of the modes is symmetric as birdcage is symmetric. For MR, only one mode of the birdcage coil ($m = 1$) is able to generate a homogeneous B_1 field. In case of HP coil, since the mode $m = 0$ is actually the resonance of the two end rings, the next mode $m = 1$ has the second largest resonance frequency and also the most homogeneous field distribution which is useful for MR imaging. The same argument for LP coil is also that the useful mode is $m = 1$ and has in this case the lowest frequency since mode $m=0$ has a null frequency. The resonance modes of bandpass birdcage coils are sophisticated in comparison with HP or LP birdcage coils. Tropp pointed out that the resonance modes of BP are concentrated in a certain frequency range and the ratio between end ring capacitor and rung capacitor determines the degeneracy of resonance modes³⁸.

5.3.2 RF design of HP birdcage coil

RF design and simulations of HP birdcage coils for small animal use

The birdcage coil was designed for imaging small animal using hyperpolarized substrates, especially in brain region, so that a coil size covering a mouse or a small rat brain was chosen. Note that from the theoretical calculation, the B_1 field becomes maximized when the ratio between length and diameter of the coil is $\sqrt{2}$ ⁴⁰, but in practice a shorter birdcage coil ($L < OD$) was considered due to the RF power limitation. A HP birdcage coil with a 16 rungs HP resonator ($OD=50$ mm, $L=32$ mm, $D_{\text{rung}}=2$ mm, $D_{\text{ring}}=3$ mm) and a RF shield ($OD=94$ mm, $L=70$ mm) was chosen.

A RF model including the HP birdcage coil shown in figure 5.3 with dimensions mentioned above and a phantom ($L=80$ mm, elec. cond. 0.5 S/m) were built: Quadrature-driven transceiver mode integrated with one variable tuning capacitor for each channel was selected to increase the sensitivity of the coil and to tune the coil to proper frequency; A variable balancing capacitor placed symmetrically between both channels was implemented to minimize the coupling between both ports; two matching capacitors (one variable and one fixed) for each channel were directly connected to the end ring and geometrically located opposite to the tuning capacitor⁴¹. After roughly calculating the tuning capacitor with Birdcage Builder⁴², the RF model was simulated in 3D EM simulation software (CST Microwave Studio, Darmstadt, Germany) to precisely approach the desired HP mode ($m = 1$) at two frequencies of interest, 400 MHz and 600 MHz, respectively. Hexahedral mesh with 60 lines per wavelength was set to simulate the electrical and magnetic field distribution of the RF model with an accuracy of -40dB in the transient solver. After fine tuning and matching both channels were decoupled at the desired frequencies by altering the balancing capacitor values. All calculated capacitor values were kept and used for building the coil prototype.

The conducting structures of the coil prototypes were manufactured from flexible PCB(0.1 mm FR4, 35 μm Cu) and then fixed on the inner support tube with an outer diameter of 50 mm (PMMA, Angst-Pfister, Switzerland). Ceramic chip capacitors (ATC-100B, American Technical Ceramics, USA) with the values properly simulated and five variable capacitors (NMKJ10HV, Voltronics, New York, USA) were used to tune birdcage coils to proper frequencies. 50 Ω coaxial cables (Huber-Suhner, Switzerland) with pre-tuned bazooka baluns⁴⁰ were attached to the matching network of the coil to transmit/receive RF signals. RF shield of the coil was constructed by printing coaxial copper strips with small gap on both sides to reduce the eddy current⁴³ and then taped inside the outer support tube with an inner diameter of 94 mm (PMMA, Angst-Pfister, Switzerland). The two support tubes were coaxially fixed by two plastic cover plates and non-magnetic screws. The whole coil holder including the animal fixation system is illustrated in figure 5.4.

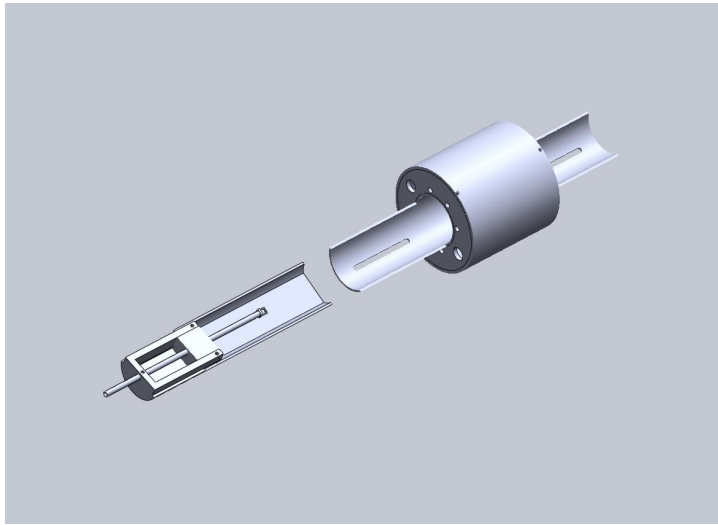


Figure 5.4: Bird cage coil holder including animal fixation system

Bench tests of HP birdcage coils

To test the bench performance of HP coils, a cylindrical phantom (OD=27 mm, L=100 mm) containing physiological saline solution (Sigma-Aldrich, USA) was fixed in the center of the coils. A plastic tube (L=250 mm, OD=120 mm) covered by copper sheet was used to cover the birdcage coil and simulate the magnet bore. Q-values were measured with a network analyzer (E5071C, Agilent, USA), with and without loading the phantom, by dividing the central frequency by the bandwidth measured at -7 dB³³ after tuning and matching two coils. Note that all the Q-values shown in this study were measured on-resonance with a -30 dB matching level.

Imaging and B_1^+ field mapping

All necessary calibrations and images were acquired on in-house 9.4 T and 14.1 T imagers (Agilent, USA) with 31 cm magnet bore. RF power calibration was carried out using STEAM sequence⁴⁴ with 2 ms Gaussian pulses. The maximum water peak intensity implied 90° power, $P_{\pi/2}$.

SNRs of the phantom images were determined by comparing the average intensity of multi-slice gradient echo (GRE) images with 90° flip angle in 5 different regions within a circle of 5 mm diameter with the noise acquired in the same areas after switching off the RF power amplifier. *In vivo* SNR maps at both field strengths were generated by using 60° GRE images through comparing the signal of each pixel to the standard deviation of noise in the artifact free corner region. Both SNR maps were rescaled by the maximum SNR value calculated. To maintain the thermal noise for both field strengths at the same level, spectral bandwidth of 69 kHz was set for both images.

To generate B_1^+ field maps, the double angle method^{46;47} was used. As the MR signal generated after a RF pulse with a flip angle θ is proportional to $\sin\theta$, the flip angle (FA) θ can be calculated through comparing the signals acquired using two different FAs, θ and 2θ , and is given by,

$$\theta = \arccos\left(\frac{I_2}{2I_1}\right) \quad (5.10)$$

where I_1 and I_2 represent the signal intensity from pixels at the same position in both images. Images for calculating B_1^+ field maps were acquired by taking axial gradient echo (GRE) images at the imager isocenter with flip angle of 60° and 120° (imaging parameters shown in table 5.2). A long enough repetition time of 20s was set to recover the proton magnetization. The region of interest (ROI) in both phantom and *in vivo* measurements were shimmed using the fastestmap method⁴⁵. Both images were post-processed using a MATLAB script which calculated the image intensity ratio from both acquisitions performed with different FAs and further determined the ratio pixel by pixel. An image mask was created by zero filling all the pixels with intensity less than 10% of the maximal pixel intensity and used to filter out noise on the B_1^+ distribution map.

5.3.3 Results and Discussions

RF simulation and bench tests

For both HP coils the capacitor values used in practice ($C_{\text{ring}} = 20.6$ pF and 8.2 pF for 9.4T and 14.1T respectively) fit to the simulated capacitor values ($C_{\text{ring}} = 20.5$ pF and 8.5 pF for 9.4 T and 14.1 T respectively) very well. The small error comes from the stray capacitance caused by the matching network which was simulated separately in the CST Design Studio and not accounted for in the CST Microwave Studio simulation. This also explains the different matching capacitor values used in practice. In figure 5.6, RF simulation of the B_1^+ field in cylindrical phantom positioned in the center of both HP coils are shown. It is apparent that the higher the frequency, the less homogeneous the B_1^+ field.

Table 5.3 shows the measured Q-values of the built HP coils and their relative sensitivities. The low relative sensitivity in small animals was related to the small size of the brain causing a relatively low loading factor. Assuming the mouse brain has a cylindrical form with a diameter of 15 mm, the filling factor is a only around $(12/50)^2 = 9\%$.

Table 5.2: MRI sequence parameters used for coil performance tests

	TR/TE [ms]	FOV [mm^2]	Resolutions
B_1^+ mapping, phantom	20,000/2.83	40×40	128×128
B_1^+ mapping, <i>in vivo</i>	20,000/3.31	20×20	128×128

The coils were driven in quadrature mode and good isolation between both channels (around -18 dB) for both loaded HP coils was determined through bench measurements.

SNR and B_1^+ field

The RF power calibration normalized to 2 ms 90° Gaussian pulse and the measured FAs are shown in table 5.3. The reason for requiring more power with the HP coil working at 14.1 T is the larger B_1^+ needed to reach the desired FA at higher magnetic field. This point can be demonstrated by looking at the difference of 30% in B_1^+ field intensity calculated in the RF simulations of both coils.

Since the SNR values depend not only on the field strength but also on the thermal noise created by the object⁴, same acquisition bandwidth and slice thickness were used to maintain the thermal noise at the same level for different images. The SNR values measured in the phantom by the 14.1 T HP coil was 1.7 times higher than the one measured by the 9.4 T HP coil (shown in table 5.3), which is slightly higher than what is expected and is mainly due to the B_1^+ field inhomogeneity. It should be mentioned that the coaxial cables used to connect the coil to the preamplifier, which is normally located on the magnet leg and 3-4 m away from the coil, led to a signal loss of 2-3 dB (according to the coaxial cable specification sheet). Similar results were obtained in *in vivo* GRE imaging and shown in the SNR maps (see figure 5.5). A 50% higher intensity was observed in the whole brain region.

B_1^+ field mapping of both HP coils in axial planes was performed with a saline phantom and *in vivo* in mouse brains both at 9.4 T and at 14.1 T. Similar to the simulated results, the B_1^+ field measured in the phantom was quite homogeneous in the HP coil at 9.4 T, but a hot spot was observed for the HP coil at 14.1 T and only the coil center had the correct FA. Taking the relative electric permittivity $\epsilon=80$ and conductivity $\sigma=0.5$ S/m from the biological tissue into account, the wavelength in the tissue is reduced to 84 mm at 9.4 T and 56 mm at 14.1 T, respectively. This implies that the hot spot was related to the dielectric resonance effect. Differences were also observed in the *in vivo* B_1^+ field maps. At 9.4 T most part of the mouse brain was uniformly excited, but at 14.1 T only the central part had the nominal FA and the rest of the brain had a smaller FA.

Table 5.3: Summary of bench measurements and in vitro calibration of unloaded/loaded birdcage coils

	$Q_{unloaded}$	Q_{loaded}	Relative sensitivity	$P_{\pi/2}$ [dB]	FA [°]	SNR
9.4T, HP	300	220	0.51	34	60 ± 1	1305 ± 39
14.1T,HP	200	176	0.35	42	51 ± 6	2207 ± 252
14.1T,BP	364	242	0.58	44	55 ± 5	2369 ± 232

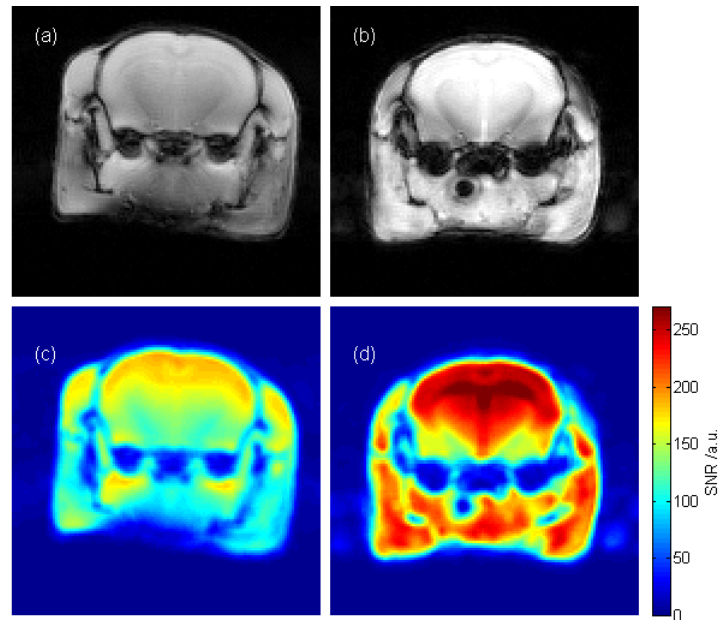


Figure 5.5: *in vivo* GRE images acquired by 9.4 T (a) and 14.1 T (b) HP birdcage coils in the isocenter with same image scale and calculated SNR maps (c) and (d), respectively.

5.3.4 Preparation of BP birdcage coil and preliminary test results

A bandpass (BP) birdcage coil with the same dimensions as the one used in the HP model was simulated and built in the same way as described above for the HP type. Due to the presence of the capacitors on the rungs in the BP model, an additional gap ($w=2$ mm) was added in the middle of the rungs. It has been reported previously that the BP mode distribution is dependent on the ratio C_{rung}/C_{ring} : when $C_{rung}/C_{ring} \gg 1$ the BP coil behaves as a HP coil; when $C_{rung}/C_{ring} \ll 1$ the BP coil tends to be a LP coil³⁸. For the intermediate case between these two extreme cases, all the modes will be compressed in the spectrum, which makes the mode differentiation difficult. Series of simulations with different values of C_{rung} were performed to understand the relationship between the frequency of the mode and the C_{rung}/C_{ring} ratio. Figure 5.7 shows the BP mode degeneracy when C_{rung}/C_{ring} is modified. In practice $C_{rung}=2$ pF was chosen for building the BP coil so that the capacitor value on the end rings could be within the range of available values.

In figure 5.8, *in vitro* B_1^+ field maps from HP and BP were compared and both coils showed typical bright spots in the center either in axial or in coronal direction. The main reasons behind the fact that the BP coil did not exhibit a large difference compared to the HP coil, are linked to the length of the coil and the sample size. As mentioned before, the constructed coils are designed for brain imaging and a normal mouse brain has a volume of $5 \times 7 \times 7$ mm³. The short distance between both end rings makes stronger field interference and, as a consequence, the shape of the B_1^+ field in both HP and BP was spherical. Other HP and BP birdcage models with long rungs were simulated and results (shown in figure 5.9)

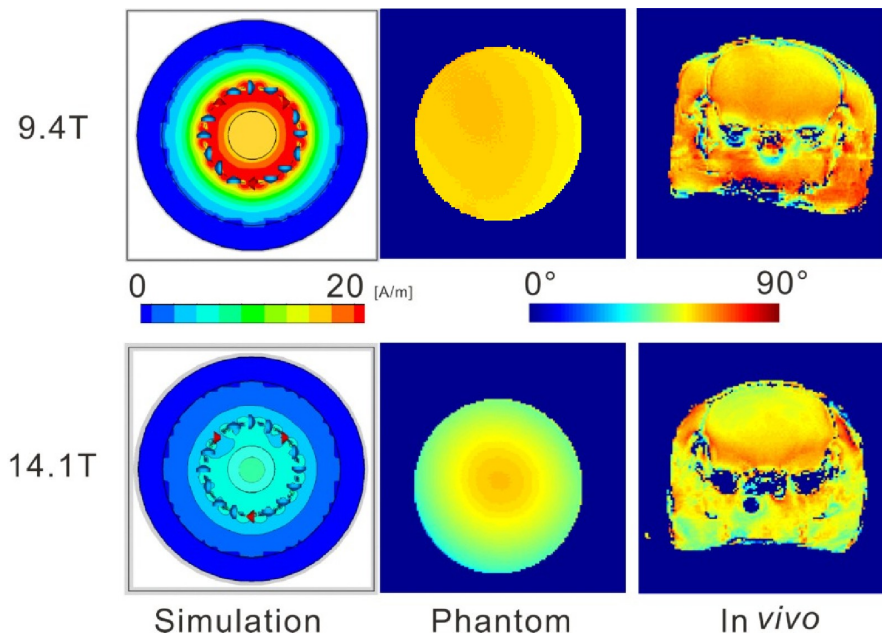


Figure 5.6: HP coil performance comparison (Results acquired at 9.4 T is shown in first row and at 14.1 T in second row): a) RF simulation (scaled from 0 to 20 A/m); b) B_1^+ mapping with a saline phantom using double angle method; c) *in vivo* B_1 mapping of mouse brains. Imaging parameters are given in table 5.2. A homogeneous B_1^+ field was measured at 9.4 T, but at 14.1 T, due to the dielectric resonance of the phantom, only the central part can be taken as homogeneous.

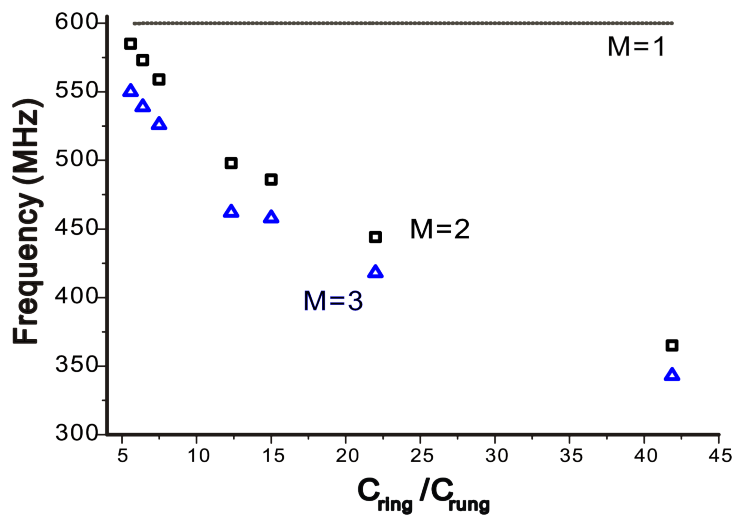


Figure 5.7: RF simulations about resonance frequency difference between required mode ($m = 1$) and other two close mode ($m = 2, 3$). BP mode $m = 1$ of all the models was tuned, matched to 600 MHz

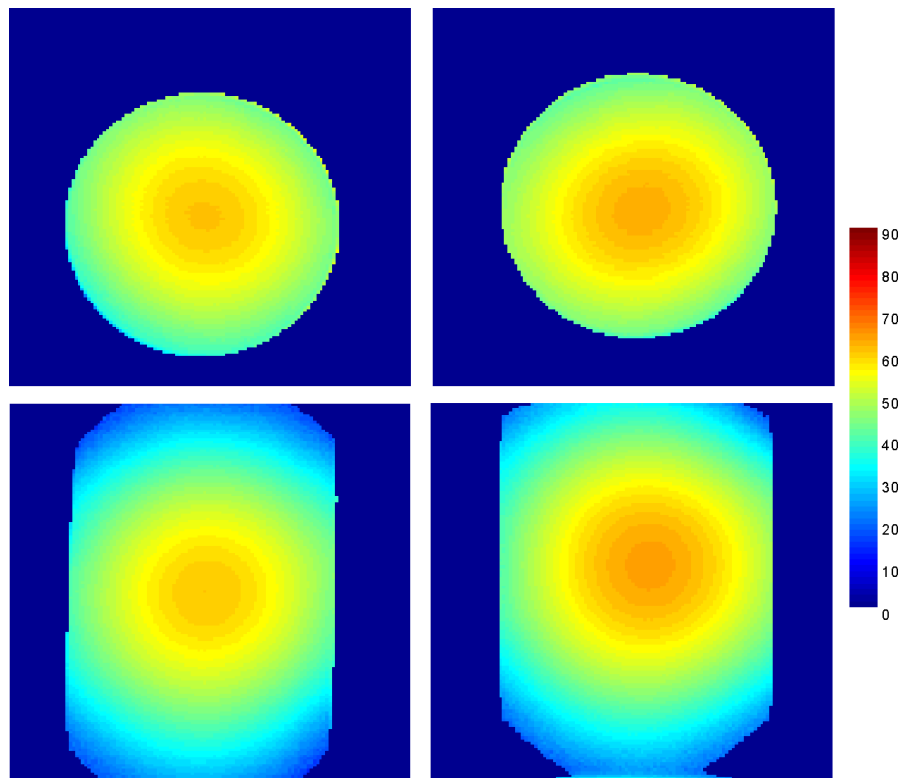


Figure 5.8: Comparison between HP (left) and BP (right) coil at 14.1T: B_1^+ mapping showed a better B_1^+ field for BP coil compared to the HP coil in spite of the bright spot acquired in the isocenter and caused by the dielectric resonance effect. This result fits to the RF simulation.

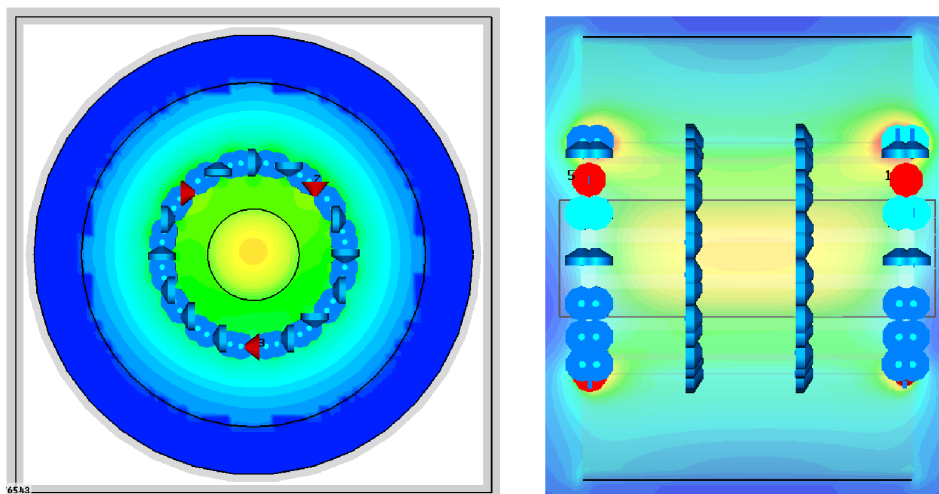


Figure 5.9: RF simulation of a BP type birdcage coil in axial (left) or coronal (right) direction at 14.1T with longer rung ($L=70$ mm): B_1^+ mapping showed a more homogeneous B_1^+ field for BP coil along coronal direction.

indicated improved B_1^+ field homogeneity than with the short ones ($L=30$ mm), but at the cost of lower B_1^+ field intensity. The dielectric resonance effect still dominated in the image acquired with the BP coil at 14.1 T, with a slightly better B_1^+ field homogeneity at the isocenter. Overall, the improved B_1^+ field generated by the BP coil indicates that, although at ultra high magnetic field the radiation losses contribute to the RF losses, the sample losses (dielectric resonance effect) are still the dominant RF losses.

5.3.5 Conclusions

In this study we demonstrated that it was possible to build transceiver birdcage coils suitable for small animal brain MRI at both 9.4 T and 14.1 T. The RF simulations proved to be a powerful tool for selecting the appropriate resonance mode and can be used for further developments of the birdcage coils. The B_1^+ homogeneity of the HP coil used at 9.4 T was better than the one of the HP coil used at 14.1 T due to the strong dielectric resonance effect in high magnetic field. This effect remained with the 14.1 T BP coil, but the field homogeneity and image SNR with the BP coil became slightly better than those obtained with the HP type as the RF radiation was minimized by more segmentation on the rungs. With the increase of the physical size and the working frequency of the coil, BP birdcage coil is an alternative for ultra high magnetic field small animal imaging, but the combination of the capacitors used on both end rings and rungs should be carefully selected to avoid mode degeneracy. In spite of the relative low sensitivity, birdcage coils are interesting for small animal imaging at ultra high magnetic field. Based on this study, birdcage coil can also be designed for imaging insensitive ^{13}C nuclei, the population of which can be highly enhanced through dissolution DNP.

References

- [1] F. D. Doty, G. Entzminger, J. Kulkarni, K. Pamarthy, and J. P. Staab. Radio frequency coil technology for small-animal mri. *Nmr in Biomedicine*, 20(3):304–325, 2007.
- [2] P. Styles, N. F. Soffe, C. A. Scott, D. A. Cragg, F. Row, D. J. White, and P. C. J. White. A high-resolution nmr probe in which the coil and preamplifier are cooled with liquid-helium. *Journal of Magnetic Resonance*, 60(3):397–404, 1984.
- [3] M. Jeroschherold and R. K. Kirschman. Potential benefits of a cryogenically cooled nmr probe for room-temperature samples. *Journal of Magnetic Resonance*, 85(1):141–146, 1989.
- [4] D. I. Hoult. The nmr receiver: A description and analysis of design. *Progress in Nuclear Magnetic Resonance Spectroscopy*, 12(1):41 – 77, 1978.
- [5] D. M. Ginsberg and M. J. Melchner. Optimum geometry of saddle shaped coils for generating a uniform magnetic field. *Review of Scientific Instruments*, 41(1):122–123, 1970.
- [6] D. W. Alderman and D. M. Grant. An efficient decoupler coil design which reduces heating in conductive samples in superconducting spectrometers. *Journal of Magnetic Resonance*, 36(3):447–451, 1979.

- [7] C. E. Hayes, W. A. Edelstein, J. F. Schenck, O. M. Mueller, and M. Eash. An efficient, highly homogeneous radiofrequency coil for whole-body nmr imaging at 1.5-t. *Journal of Magnetic Resonance*, 63(3):622–628, 1985.
- [8] J. Tropp. The theory of the bird-cage resonator. *Journal of Magnetic Resonance*, 82(1):51–62, 1989.
- [9] M. C. Leifer. Resonant modes of the birdcage coil. *Journal of Magnetic Resonance*, 124(1):51–60, 1997.
- [10] J. Tropp. Dissipation, resistance, and rational impedance matching for tem and birdcage resonators. *Concepts in Magnetic Resonance*, 15(2):177–188, 2002.
- [11] J. T. Vaughan, H. P. Hetherington, J. O. Otu, J. W. Pan, and G. M. Pohost. High frequency volume coils for clinical nmr imaging and spectroscopy. *Magn Reson Med*, 32(2):206–18, 1994.
- [12] J. T. Vaughan, M. Garwood, C. M. Collins, W. Liu, L. DelaBarre, G. Adriany, P. Andersen, H. Merkle, R. Goebel, M. B. Smith, and K. Ugurbil. 7t vs. 4t: Rf power, homogeneity, and signal-to-noise comparison in head images. *Magn Reson Med*, 46(1):24–30, 2001.
- [13] N. Zhang, M. Roos, J. Vaughan, and T. Budinger. Head coil b1 field inhomogeneity and snr performance at 8-10t. *Proceedings of the International Society for Magnetic Resonance in Medicine*, 1996(S1):252, 1996.
- [14] T. Vaughan, L. DelaBarre, C. Snyder, J. Tian, C. Akgun, D. Shrivastava, W. Liu, C. Olson, G. Adriany, J. Strupp, P. Andersen, A. Gopinath, P. F. van de Moortele, M. Garwood, and K. Ugurbil. 9.4t human mri: preliminary results. *Magn Reson Med*, 56(6):1274–82, 2006.
- [15] J. Tropp. Image brightening in samples of high dielectric constant. *Journal of Magnetic Resonance*, 167(1):12–24, 2004.
- [16] J. J. H. Ackerman, T. H. Grove, G. G. Wong, D. G. Gadian, and G. K. Radda. Mapping of metabolites in whole animals by p-31 nmr using surface coils. *Nature*, 283(5743):167–170, 1980.
- [17] R. A. Degraaf, Y. Luo, M. Terpstra, H. Merkle, and M. Garwood. A new localization method using an adiabatic pulse, bir-4. *Journal of Magnetic Resonance Series B*, 106(3):245–252, 1995.
- [18] P. B. Roemer, W. A. Edelstein, C. E. Hayes, S. P. Souza, and O. M. Mueller. The nmr phased array. *Magn Reson Med*, 16(2):192–225, 1990.
- [19] D. I. Hoult, G. Kolansky, D. Kripiakevich, and S. B. King. The nmr multi-transmit phased array: a cartesian feedback approach. *Journal of Magnetic Resonance*, 171(1):64–70, 2004.
- [20] X. Zhang and A. Webb. Design of a capacitively decoupled transmit/receive nmr phased array for high field microscopy at 14.1t. *Journal of Magnetic Resonance*, 170(1):149–55, 2004.
- [21] C. N. Chen, D. I. Hoult, and V. J. Sank. Quadrature detection coils - a further square-root2 improvement in sensitivity. *Journal of Magnetic Resonance*, 54(2):324–327, 1983.
- [22] J. S. Hyde, A. Jesmanowicz, T. M. Grist, W. Froncisz, and J. B. Kneeland. Quadrature detection surface coil. *Magn Reson Med*, 4(2):179–84, 1987.
- [23] C. N. Chen and D. I. Hoult. *Biomedical magnetic resonance technology*. Hilger, 1989.
- [24] U. S. Inan and A. S. Inan. *Engineering electromagnetics*. Addison-Wesley, Menlo Park, Calif., 1999.
- [25] A. S. Hall, N. M. Alford, T. W. Button, D. J. Gilderdale, K. A. Gehring, and I. R. Young. Use of high-temperature superconductor in a receiver coil for magnetic-resonance-imaging. *Magnetic Resonance in Medicine*, 20(2):340–343, 1991.
- [26] R. D. Black, T. A. Early, P. B. Roemer, O. M. Mueller, A. Mogrocampero, L. G. Turner, and G. A. Johnson. A high-temperature superconducting receiver for nuclear-magnetic-resonance microscopy. *Science*, 259(5096):793–795, 1993.

Chapter 5. MR probes for *in vivo* MRS and MRI at ultra high magnetic field

- [27] R. D. Black, T. A. Early, and G. A. Johnson. Performance of a high-temperature superconducting resonator for high-field imaging. *Journal of Magnetic Resonance Series A*, 113(1):74–80, 1995.
- [28] J. C. Ginefri, L. Darrasse, and P. Crozat. High-temperature superconducting surface coil for *in vivo* microimaging of the human skin. *Magnetic Resonance in Medicine*, 45(3):376–382, 2001.
- [29] A. C. Wright, H. K. Song, and F. W. Wehrli. *In vivo* mr micro imaging with conventional radiofrequency coils cooled to 77 degrees k. *Magnetic Resonance in Medicine*, 43(2):163–169, 2000.
- [30] D. Ratering, C. Baltes, J. Nordmeyer-Massner, D. Marek, and M. Rudin. Performance of a 200-mhz cryogenic rf probe designed for mri and mrs of the murine brain. *Magnetic Resonance in Medicine*, 59(6):1440–1447, 2008.
- [31] M. D. Harpen. Sample noise with circular surface coils. *Medical Physics*, 14(4):616–8, 1987.
- [32] Joseph Murphy-Boesch and Alan P. Koretsky. An *in vivo* nmr probe circuit for improved sensitivity. *Journal of Magnetic Resonance (1969)*, 54(3):526–532, 1983.
- [33] A. Haase, F. Odoj, M. Von Kienlin, J. Warnking, F. Fidler, A. Weisser, M. Nittka, E. Rommel, T. Lanz, B. Kalusche, and M. Griswold. Nmr probeheads for *in vivo* applications. *Concepts in Magnetic Resonance*, 12(6):361–388, 2000.
- [34] R. J. Pascone, B. J. Garcia, T. M. Fitzgerald, T. Vullo, R. Zipagan, and P. T. Cahill. Generalized electrical analysis of low-pass and high-pass birdcage resonators. *Magn Reson Imaging*, 9(3):395–408, 1991.
- [35] T. S. Ibrahim, R. Lee, B. A. Baertlein, and P. M. L. Robitaille. B-1 field homogeneity and sar calculations for the birdcage coil. *Physics in Medicine and Biology*, 46(2):609–619, 2001.
- [36] P. Roschmann. Radiofrequency penetration and absorption in the human-body - limitations to high-field whole-body nuclear-magnetic-resonance imaging. *Medical Physics*, 14(6):922–931, 1987.
- [37] J. W. Carlson. Radiofrequency field propagation in conductive nmr samples. *Journal of Magnetic Resonance*, 78(3):563–573, 1988.
- [38] J. Tropp. The hybrid bird cage resonator. *Proceedings of the International Society for Magnetic Resonance in Medicine*, 1992(Supplement S2):4009, 1992.
- [39] P. Pimmel and A. Briguet. A hybrid bird cage resonator for sodium observation at 4.7-t. *Magnetic Resonance in Medicine*, 24(1):158–162, 1992.
- [40] J. Mispelner, M. Lupu, and A. Briguet. *NMR probeheads for biophysical and biomedical experiments: theoretical principles & practical guidelines*. Imperial College Press, London, 2006.
- [41] J. Murphy-Boesch. Double-tuned birdcage coils: Construction and tuning. In *Encyclopedia of Magnetic Resonance*. John Wiley & Sons, Ltd, 2007.
- [42] C. L. Chin, C. M. Collins, S. Z. Li, B. J. Dardzinski, and M. B. Smith. Birdcagebuilder: Design of specified-geometry birdcage coils with desired current pattern and resonant frequency. *Concepts in Magnetic Resonance*, 15(2):156–163, 2002.
- [43] G. X. Shen. Double-sided stripline rf shield. In *Proceedings of the International Society for Magnetic Resonance in Medicine*, volume 1992, page 4048, 1992.
- [44] J. Frahm, K. D. Merboldt, and W. Hanicke. Localized proton spectroscopy using stimulated echoes. *Journal of Magnetic Resonance*, 72(3):502–508, 1987.
- [45] R. Gruetter. Automatic, localized *in vivo* adjustment of all first- and second-order shim coils. *Magnetic Resonance in Medicine*, 29(6):804–11, 1993.
- [46] R. Stollberger, P. Wach, G. McKinnon, E. Justich, and F. Ebner. Rf-field mapping *in vivo*. In *Proceedings of the International Society for Magnetic Resonance in Medicine*, volume 1988, page 106, San Francisco, 1988.
- [47] E. K. Insko and L. Bolinger. B1 mapping. In *Proceedings of the International Society for Magnetic Resonance in Medicine*, volume 1992, page 4302, 1992.

Conclusions and future perspectives

Methods to minimize the polarization losses and related hardware designs

^{13}C labeled sodium acetate was successfully polarized at 5 T and after dissolution a liquid-state polarization level of 13% was measured just before the injection for *in vivo* studies in rodents. By using a home-built RF switching network the *in vitro* polarization determination and *in vivo* experiment can be successively carried out without delaying the *in vivo* injection. The solenoid coil around the separator/infusion pump tuned to ^{13}C frequencies not only facilitates the longitudinal relaxation time measurements inside the magnet bore, but it also extends the function of the separator/infusion pump. This setup can of course also be tuned to other nuclear resonance frequencies, e.g. ^{15}N and ^{89}Y so that the longitudinal relaxation time determination and a liquid-state polarization transfer from highly polarized nuclear spins to low- γ nuclear spins can be realized in the future. To extend the longitudinal relaxation time of ^{13}C spins, we used sodium ascorbate to scavenge nitroxyl radicals, but a decrease in T_1 with increasing sodium ascorbate concentration indicated that the protons attached to the ascorbate molecules influence the T_1 of ^{13}C spins. After having partially deuterated sodium ascorbate, the observed dramatic T_1 extension from 35 s to 73 s shows that deuterated ascorbate can help extending the time measurement window in hyperpolarized NMR experiments.

Radical-free hyperpolarized alcohol via SL-hydrogel

In the pilot study performed with SL-hydrogel, we managed to get a ^{13}C polarization of 0.05% in natural ^{13}C abundance deuterated *tert*-butanol. The most important result was that the ^{13}C signal decay measured in the hyperpolarized sample following dissolution was as long as the longitudinal relaxation time measured in degassed pure *tert*-butanol at thermal equilibrium in a high-resolution NMR spectrometer. Similar results were obtained with deuterated ethanol. These results demonstrated that the hyperpolarized solution after dissolution of the solid sample polarized via SL-hydrogel was radical free.

Due to the hydrophilic characteristics of the hydrogel only water or alcohols which

Conclusions and future perspectives

are liquid at ambient temperature can be hyperpolarized using this method. *Tert*-butanol was considered as an interesting candidate due to the possible application for perfusion imaging. To improve the signal enhancement of *tert*-butanol for *in vivo* applications, ^{13}C spin concentration can be increased by using ^{13}C labeled *tert*-butanol. It has indeed already been reported that a higher spin concentration in the solid sample leads to improved ^{13}C spin diffusion and therefore to higher ^{13}C polarization. It would also be necessary to increase the radical labeling concentration in the hydrogel.

DNP of long- T_1 nuclear spins

For *in vivo* MRS study of choline brain uptake, a liquid-state ^{15}N polarization level of 5% was obtained after 4h of polarization with the same microwave settings as for ^{13}C labeled substrates. The long polarization time is consistent with the fact that ^{15}N has a very low- γ . We expect that polarization transfer methods will play an important role in future improvement of hyperpolarized ^{15}N metabolic studies. A ^1H – ^{15}N double tuned coil should be considered for solid-state cross polarization to reduce the polarization time of ^{15}N spins and increase its polarization level. In addition, *in situ* ^{15}N – ^1H polarization transfer could enhance the *in vivo* ^1H MRS signal of choline metabolites while keeping the long time window offered by the long T_1 of ^{15}N .

Due to the low solubility of $\text{Y}[\text{DOTA}]^-$, solid-state calibrations of DNP-enhanced ^{89}Y was carried out with concentrated water soluble yttrium chloride samples. After 7 hours of solid-state polarization, hyperpolarized ^{89}Y signals from $\text{Y}[\text{DOTA}]^-$ complexes polarized using TEMPO radicals were readily detected. As mentioned before, from the general observation that all nuclear spins eventually reach the same spin temperature, we could have expected a ^{89}Y polarization of 1.3%, which is almost four times higher than what we obtained in our *in vitro* tests. To improve the ^{89}Y DNP, a big obstacle lies in the low ^{89}Y concentration in the $\text{Y}[\text{DOTA}]^-$ sample (0.18 M in our case), which is much lower than the ^{13}C concentration in typical samples used for hyperpolarized ^{13}C NMR experiments. A possible way to improve the ^{89}Y polarization would be to transfer the polarization from highly polarizable nuclear spins such as ^1H or ^{13}C to ^{89}Y spins, either in the solid-state or in the liquid-state.

Birdcage coil for *in vivo* MRI

Birdcage coils are very useful to homogeneously excite the spins in MRI experiments, but their intrinsic low sensitivity due to the large volume and associated low filling factor make them unpopular for *in vivo* MRS. Thanks to the tremendous SNR increase obtained using dissolution DNP, the sensitivity of NMR experiments is increased but complex fast sequences have to be developed and although surface coils are still preferred for detection, birdcage coils are a good choice for spin excitation. In this thesis two high-pass birdcage coils working at 9.4 T and 14.1 T and one bandpass birdcage coil working at 14.1 T were designed, simulated and

built for small animal ^1H imaging. The calculated B_1^+ field for the 9.4 T high-pass coil was much more homogeneous than that for the 14.1 T high-pass coil. This reflects the strongly dominant dielectric resonance effect at higher magnetic field. Meanwhile the relative low sensitivity of all three coils (~ 0.5) shown in bench tests and the simulated results of the high-pass coil with long rungs (80 mm) show that the sample losses and radiation losses are not the dominant losses for the high field birdcage coils. After considering all these issues, bandpass coil built for 14.1 T showed a slightly improved B_1^+ field due to the possible reduced radiation losses.

The birdcages were originally designed for *in vivo* DNP-enhanced MRS/MRI experiments. Due time constraints and the lack of a proper setup to hold the animals inside the coil, we did not manage to perform any DNP experiment using these coils. We however expect that there should not be any major problems to run such experiments using hyperpolarized ^1H (in partially deuterated water) in the future after having properly addressed the problem linked to animal positioning and defined the associated injection protocol for hyperpolarized substrates. Another interesting improvement, already highlighted in chapter 5, could be to build and test a birdcage coil with longer rungs for improved B_1^+ field homogeneity in the coronal direction (this was found through simulations). A further development would be the implementation of a ^{13}C birdcage coil for hyperpolarized NMR experiments since the most promising applications are *in vivo* metabolic studies using hyperpolarized ^{13}C -labeled substrates.

A DNP performance of biradicals

Solutions for solid-state samples were composed of 1-¹³C acetate dissolved in a mixture of d₆-ethanol and D₂O (1:2 v/v) containing biradicals provided by Dr. Oliver Quari and Prof. Paul Tordo from the Universités d'Aix-Marseille. Since the solubility in D₂O of some of the biradicals tested was poor, the mixing ratio of the solvent between d₆-ethanol and D₂O was increased to 2:1 for most samples. Two test samples (sample B and C) containing two different nitroxyl biradicals, bTbK and dCdO (chemical structure is shown in the figure A.1), were prepared as described above. All DNP experiments on all samples were performed at 140 GHz using 40 mW power and the NMR signals were acquired with the detection parameters described in 2.1. The enhancement factor was determined by calculating the ratio between polarized signal at 1K and thermal equilibrium signal at 3.2K. The results are summarized in table A.1 along with the results obtained on a reference sample (sample A) containing the mononitroxyl TEMPO. Note that TEMPO can lead to even higher enhancement if the ethanol to water ratio is further reduced, in agreement with a previous study. The larger the biradical concentration is, the faster the polarization builds up. As shown in a comparable study related to trityl biradicals, TEMPO-based biradicals are not more efficient than the TEMPO monoradicals in DNP experiments performed at liquid helium temperature.

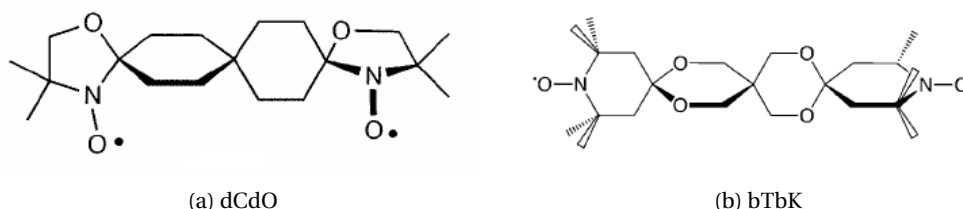


Figure A.1: Molecular structure of the two biradicals used in the present study: dCdO and bTbk.

Appendix A. DNP performance of biradicals

Table A.1: Property and DNP results of each measured samples: A: 2M $1\text{-}^{13}\text{C}$ NaAc + TEMPO + ethanol/ D_2O (2:1 v/v); B: 2M $1\text{-}^{13}\text{C}$ NaAc + dCdO + ethanol/ D_2O (2:1 v/v); C: 2M $1\text{-}^{13}\text{C}$ NaAc + bTbK + ethanol/ D_2O (2:1 v/v)

Sample	Radical conc. [mM]	e-e distance [Å]	Buildup time constant [s]	ϵ	T_1
A	30	-	2252±64	75	18164±5
B	30	8.23	1625±59	24	10498±802
B	15	8.23	9126±1433	-	-
C	30	12.95	1485±78	20	4798±452
C	15	12.95	1733±135	16	6000
C	7.5	12.95	3064±237	10	9000

B X-ray induced radicals

Radiation-induced radicals were introduced in chapter 2. To test the creation efficiency of radiation-induced radicals in biologically compatible samples, a new radiation experimental setup based on x-ray source with maximal intensity of 40 kV was built to irradiate frozen sample. Those samples were prepared in bead form and contained 3M sodium acetate dissolved in a solvent mixture of ethanol and distilled water. For each experiment, 20-25 beads were collected and placed on a custom-designed sample cup made of copper ($3 \times 3\text{cm}^2$) with continuously cooling of liquid nitrogen (see Figure B.1(a)). The distance between the sample cup and the source was kept constant (3 cm) during the entire irradiation process and to avoid x-ray absorption no liquid nitrogen was kept inside the sample cup. To check that the temperature of the sample stayed around 100K, a calibrated temperature probe (thermal couple) was fixed on the copper sample cup.

Samples with different ethanol/ D_2O ratios were irradiated several hours and afterwards 9 beads were quickly loaded into a pre-cooled 5mm ESR tube for the ESR measurements. The main reason of not preparing 100% EtOH beads and with small fraction of D_2O instead

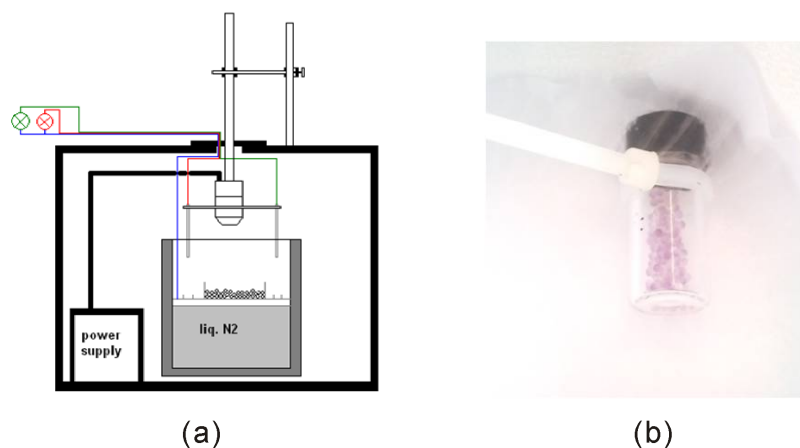


Figure B.1: (a) X-ray irradiation setup;(b) Luminescence of the EtOH sample doping with LiCl

Appendix B. X-ray induced radicals

Table B.1: Summary of parameters used for x-ray irradiated samples

No.	Sample	Time [h]	Ratio(D_2O /EtOH)	Radical density [$\cdot 10^{17} spins/cm^3$]
1	TEMPO (liq.)	-	2:1	-
2	Ethanol (liq.)	-	2:1	-
3	TEMPO (beads)	-	2:1	180
4	Ethanol (beads)	5h	2:1	1.82
4	Ethanol (beads)	10h	2:1	2.17
4	Ethanol (beads)	2nd day	2:1	1.90
5	Ethanol (beads)	4h	1:2	4.36
5	Ethanol (beads)	6h	1:2	3.45

of the H_2O is due to the low melting temperature of EtOH and the strong x-ray attenuation of protonated water. Immediately after irradiation, all samples had turned light purple (see Figure B.1(b)) and the color bleached after 5-10 minutes. ESR spectra were acquired at 100 K on a commercial X-band spectrometer (Bruker). The radical concentration created was obtained by comparing the peak integral between the sample and a reference containing 30mM TEMPO and weighing the beads to normalize the radical density. The radical concentration for all samples is shown in the Table B.1. We concluded that after an average irradiation time of about 4 h, the maximum achievable radical concentration was reached and a higher EtOH to water ratio led to increased radical concentration. The biggest radical concentration created in this type of sample was around $4.36 \cdot 10^{17} / cm^3$. After having stored the samples in liquid nitrogen for about 12 h, no significant radical recombination was observed. To demonstrate that the x-ray induced radicals will be eliminated after dissolution, beads were melted in the ESR tube and room-temperature ESR measurements (liquid state) were performed. The results showed that in all cases there was no radical left.

C Optimization of dissolution parameters

The separator/infusion pump was designed to achieve automatic quick transfer of hyperpolarized liquids from the polarizer to the scanner, and precise injection of the liquids to the animals used for *in vivo* MR experiments in a relatively short time period without the influence of personnels. The critical part which needs to be controlled is actually the minimized transfer time and reproducible injection volume (or concentration). To achieve this goal several parameters can be optimized. The schematics of a typical dissolution procedure is shown in figure C.1 and detailed explanation of the whole protocol has been introduced in chapter 2. To reduce the dimension of the optimization processes, the dissolution time $T_{dissolution}$, delay time T_{delay} and injection time $T_{injection}$ were fixed with previous experience to 0.8s, 1s and 8.6s, respectively. This means the optimization processes were carried out in the section of sample transfer by altering the transferring pressure P_{push} and transferring time T_{push} to get maximum volume of liquids. The optimization was performed by using similar samples and exact same experimental condition as for *in vivo* experiments with various combination of P_{push} ranged from 4 to 6 bar and T_{push} from 1.9s up to 3.6s. The results in figure C.1(right) showed, first, a maximum volume of 2.45mL hyperpolarized liquids could be gathered in the infusion pump; second, with the increase of the transferring pressure up to 6bar the transferring time was able to be reduced to 1.9s, but the dynamic range for obtaining a stable liquid volume was strongly reduced due to the turbulent flow created by the high pressure helium gas through the long thin plastic tube used as transfer line. As fast transfer time and stable liquid volume are the two vital requirements for the *in vivo* experiments, the combination of transferring pressure of 6bar and transferring time of 2s has been chosen to be part of standard parameters in the dissolution protocol.

Appendix C. Optimization of dissolution parameters

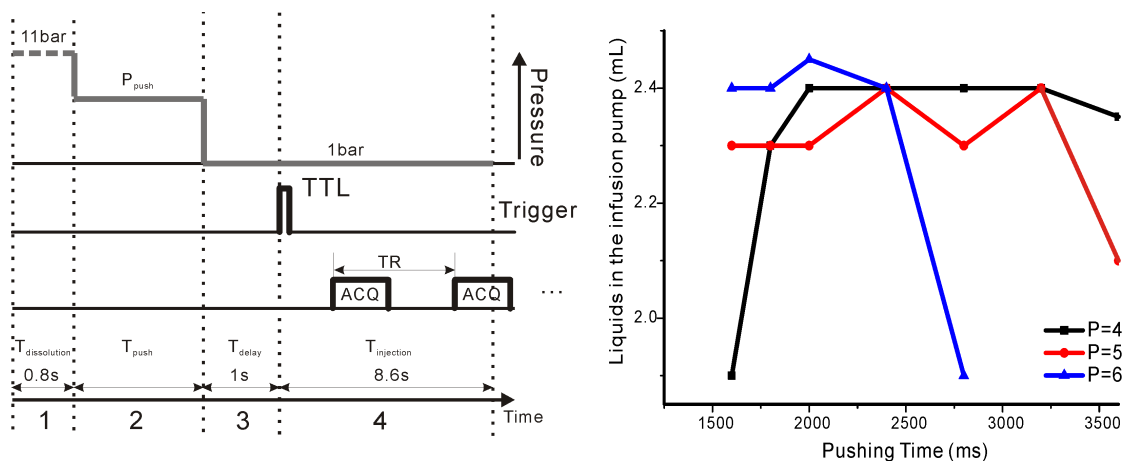


Figure C.1: Dissolution parameter optimization. Left side: Schematics of dissolution procedures including dissolution(1), transfer(2), settling(3) and infusion(4); Right side: Test results of transferred liquid volume measured inside the infusion pump by altering pressure and duration of the helium gas.

D Polarization level determination

D.1 Classical polarization determination

In in vivo MR studies, metabolites' concentration is usually in μM range. To precisely detect such a tiny concentration in one-shot experiment like DNP highest possible polarization is necessary. For a specific tracer in vitro polarization calibration becomes important before applied for in in vivo measurements. Polarization level of a specific nuclear spin is determined by the product of the enhancement factor ϵ and the thermal polarization $P_{thermal}$ described as,

$$P = P_{thermal} \cdot \epsilon \quad (\text{D.1})$$

Table D.1 shows the thermal polarization of ^{13}C nuclei at several typical magnetic field used for DNP procedure. The enhancement factor, either in liquid-state or in solid-state, is given by the ratio between the polarized signal S_{DNP}^T and the thermal signal $S_{thermal}$ at certain temperature T, apart from the noise N^T ,

$$\epsilon = \frac{S_{DNP}^T - N^T}{S_{thermal}^T - N^T}. \quad (\text{D.2})$$

Note that both signals and noise used for determining enhancement factor ϵ need to be measured under same circumstances, e.g. by same RF coil at same temperature T and with

Table D.1: Thermal polarization of ^{13}C at different magnetic fields

Temperature [K]	Polarization				
	@3.35T	@5T	@7T	@9.4T	@14.1T
1.05	8.21E-4	1.23E-3	1.72E-3	2.30E-3	3.46E-3
4	2.05E-4	3.06E-4	4.29E-4	5.76E-4	8.64E-4
300	2.87E-6	4.29E-6	6E-6	8.06E-6	1.21E-6

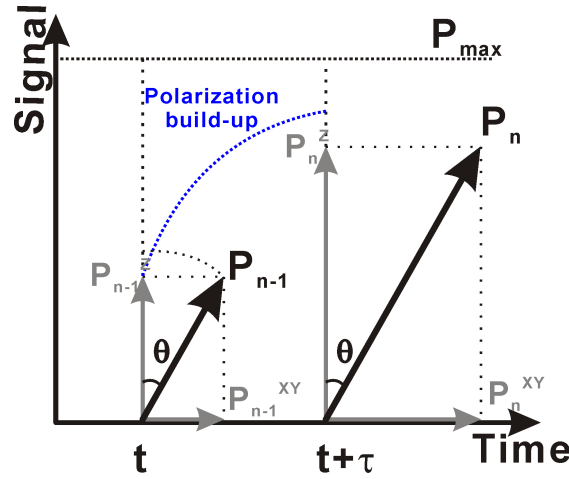


Figure D.1: Description of the polarization build-up within time interval of τs from P_{n-1} to P_n . The measurable parts of the polarization are its projection on XY plane after RF pulse with a flip angle of θ .

the same RF pulse.

D.2 Polarization build-up simulation

In this paragraph we are going to discuss the solid-state polarization build-up process under the influence of different RF pulse parameters which is shown figure D.1. The solid-state polarization signal P_n at the time point $t = n \cdot \tau$ monitored by using single pulse with a fixed flip angle θ is given by,

$$P_n = (P_{\max} - P_{n-1} \cos\theta) \cdot (1 - e^{-\tau/T_{\text{build-up}}}) + P_{n-1} \cdot \cos\theta, \quad (\text{D.3})$$

where P_{n-1} is the measured polarization at time point $t' = (n-1) \cdot t$ and $T_{\text{build-up}}$ the true build-up time constant of the sample without any RF perturbations. Replacing the equation above with $P_1 = P_{\max} \cdot (1 - e^{-\tau/T_{\text{build-up}}})$, we can get

$$P_n = P_1 + P_{n-1} \cdot \cos\theta \cdot e^{-\tau/T_{\text{build-up}}}. \quad (\text{D.4})$$

After the simplification of the equation with parameter $k = \cos\theta \cdot e^{-\tau/T_{\text{build-up}}}$ and the calculation of the geometric progression the polarization P_n can be expressed as,

$$P_n = \frac{k^n - 1}{k - 1} \cdot P_1 = \frac{k^n - 1}{k - 1} \cdot P_{\max} \cdot (1 - e^{-\tau/T_{\text{build-up}}}), \quad (\text{D.5})$$

D.3. Polarization calculation through build-up

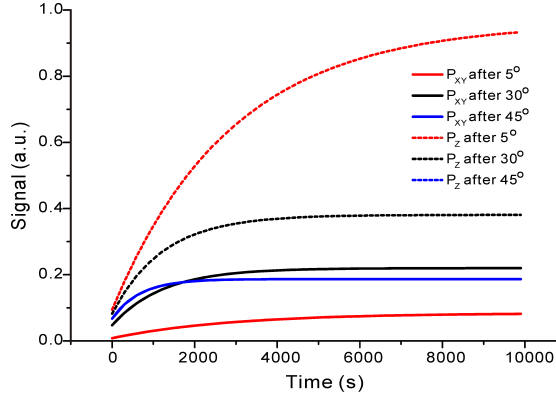


Figure D.2: Simulation of the DNP build-up by applying various RF pulses with different flip angles: 5° , 30° , 45°

and the polarization on the longitudinal direction, P_n^Z , and transversal direction, P_n^{XY} , can be easily deduced from the equation above and written as ,

$$\begin{aligned} P_n^{XY} &= \frac{k^n - 1}{k - 1} \cdot P_1 \cdot \sin\theta = \frac{k^n - 1}{k - 1} \cdot P_{max} \cdot (1 - e^{-\tau/T_{build-up}}) \cdot \sin\theta \\ P_n^Z &= \frac{k^n - 1}{k - 1} \cdot P_1 \cdot \cos\theta = \frac{k^n - 1}{k - 1} \cdot P_{max} \cdot (1 - e^{-\tau/T_{build-up}}) \cdot \cos\theta \end{aligned} \quad (D.6)$$

As the meaning in the NMR, P_n^{XY} represents the measurable polarization which diminishes through T2 relaxation and P_n^Z the reserved polarization which will be kept and undergo the T1 relaxation. Assume that $P_{max} = 1$, $\tau = 300s$ and $T_{build-up} = 3000s$, the simulation of DNP build up curve with different monitoring flip angle θ is shown in figure D.2. From the results several information can be obtained: a) With large flip angle θ more measurable polarization can be used for monitoring and at certain angle the measurable polarization decreases; b) With large flip angle θ the final steady state polarization can be actually reached much faster than expected and the reserved polarization decreases; c) The build-up time is always shorter than the real build-up time of the spin with the RF perturbations. In summary small flip angle pulse is more suitable to monitor the solid-state polarization.

D.3 Polarization calculation through build-up

Since the solid-state relaxation time of nuclear spins at liquid helium temperature (4.2K) is still reasonable short (~ 20 mins for ^{13}C) enhancement factor ϵ can be easily determined in several hours. But the thermal polarization becomes hard to measure when the experimental temperature drops to 1K and the solid-state relaxation time dramatically increases to 10ks range. To calculate the maximal polarization P_{max} and $T_{build-up}$, we can measure final polarization by varying different parameters (flip angle θ or monitoring time interval τ) and then compare the signals to deduce the polarization level and the real build-up time constant.

Appendix D. Polarization level determination

D.3.1 varying flip angle

Consider two experiments performed with different flip angle θ_1 and θ_2 and assume that the experiments long enough ($n > 50$) so that $k^n \ll 1$,

$$\begin{aligned} P_n^1 &= \frac{\sin\theta_1}{(1-k_1)} \cdot P_{max} \cdot (1 - e^{-\tau/T_{build-up}}) \\ P_n^2 &= \frac{\sin\theta_2}{(1-k_2)} \cdot P_{max} \cdot (1 - e^{-\tau/T_{build-up}}) \end{aligned} \quad (D.7)$$

After comparing the two equations above, an equation only dependent on $T_{build-up}$ can be obtained,

$$\frac{P_n^2}{P_n^1} = \frac{\sin\theta_2}{\sin\theta_1} \cdot \frac{1-k_1}{1-k_2}. \quad (D.8)$$

The real build-up time can be rewritten as,

$$T_{build-up} = -\frac{\tau}{\ln \frac{P_n^1 \sin\theta_2 - P_n^2 \sin\theta_1}{P_n^1 \sin\theta_2 \cos\theta_1 - P_n^2 \sin\theta_1 \cos\theta_2}}, \quad (D.9)$$

and the maximal polarization is then,

$$P_{max} = \frac{P_n^1 (1-k_1)}{\sin\theta_1 (1 - e^{-\tau/T_{build-up}})}, \quad (D.10)$$

Assume that $\theta_2 = 2\theta_1$ and the equation of the build-up time can be simplified as,

$$T_{build-up} = -\frac{\tau}{\ln \frac{2 \cdot P_n^1 \sin\theta_1 - P_n^2}{2 \cdot (P_n^1 - P_n^2) \cos\theta_1^2 + P_n^2}}, \quad (D.11)$$

D.3.2 varying time interval

Consider two experiments performed now with a same flip angle θ , but measured with two various time interval (τ and 2τ). The same assumption that the experiments last long enough ($n > 50$) should be followed to ensure the approximation. The polarization measured in both cases can be expressed as,

$$\begin{aligned} P_n^1 &= \frac{\sin\theta}{1-k_1} \cdot P_{max} \cdot (1 - e^{-\tau/T_{build-up}}) \\ P_n^2 &= \frac{\sin\theta}{1-k_2} \cdot P_{max} \cdot (1 - e^{-2\tau/T_{build-up}}) \end{aligned} \quad (D.12)$$

with $k_1 = \cos\theta \cdot e^{-\tau/T_{build-up}}$ and $k_2 = \cos\theta \cdot e^{-2\tau/T_{build-up}}$. Then the ratio between both build-up plateau is,

$$\frac{P_n^2}{P_n^1} = \frac{1-k_1}{1-k_2} \cdot \frac{1 - e^{-2\tau/T_{build-up}}}{1 - e^{-\tau/T_{build-up}}} \quad (D.13)$$

$$\frac{P_n^2}{P_n^1} = 1 + \frac{(1 - \cos\theta)e^{-\tau/T_{build-up}}}{1 - \cos\theta e^{-2\tau/T_{build-up}}} \quad (D.14)$$

The solution of the build-up time is,

$$T_{build-up} = - \frac{\tau}{\ln \frac{(1 - \cos\theta) - \sqrt{(\cos\theta - 1)^2 + 4 \cos\theta \left(\frac{P_n^2}{P_n^1} - 1\right)^2}}{2\left(1 - \frac{P_n^2}{P_n^1}\right) \cos\theta}}, \quad (D.15)$$

and the maximal polarization is as in equation...

$$P_{max} = \frac{2P_n^1(1 - k_1)}{\sin 2\theta_1(1 - e^{-\tau/T_{build-up}})}. \quad (D.16)$$

D.3.3 Summary

The two methods introduced in previous two sections theoretically shows the possibility of calculating maximal polarization of DNP through comparing two separate datasets of DNP buildup. In practice there are some other constraints: a) By varying flip angle θ the measurable polarization signals of the experiments is easy to distinguish, but a well calibrated flip angle is mandatory for the final calculation; b) By varying time interval τ it is difficult to observe significant difference of the measurable polarization with even different time intervals so that to precisely detect NMR signals for both measurements plays a vital role in the calculation; c) In general the polarization calculated here should come from target nuclear spins and should not be influenced by the leakage of other nuclear spins polarized simultaneously. This means, with trityl radicals this measurements should be much more accurately.

Tian Cheng

Address: Rue de la Blancherie 1
CH-1022 Chavannes-près-Renens
Switzerland
Date of birth: 17.12.1981
Place of birth: Nanchang, Jiangxi, P.R. China
Nationality: Chinese
Tel: +41 21 693 79 66
Email : tian.cheng@epfl.ch

PROFESSIONAL EXPERIENCE

- 2009 - 2013 **PhD candidate, École Polytechnique Fédérale de Lausanne, Switzerland**
- Dissolution DNP technique and its hardware developments;
 - *in vivo* DNP-enhanced magnetic resonance spectroscopy and imaging;
 - Design, simulation and construction of RF instrumentation used in MR;
 - Novel radicals development;
 - Electron Spin Resonance (ESR), functional MRI (fMRI) and its data analysis.
- Teaching assistant, École Polytechnique Fédérale de Lausanne, Switzerland
- Advanced Physics laboratory course
 - General Physics I
- 2004 - 2008 **Technical assistant, German Cancer Research Center (DKFZ):**
Part-time technical assistant at the cyclotron department of maintaining Germanium detectors with liquid nitrogen and checking residual dose of radioactive solutions used for PET
-

EDUCATION

- 2009 – 2013 PhD in Physics,
École Polytechnique Fédérale de Lausanne, Switzerland
- 2007 - 2008 MSc in Medical Physics,
University Medical Centre Mannheim, Ruprecht-Karl University of
Heidelberg, Germany
- 2003 - 2008 Dipl. in Physics,
Ruprecht-Karl University of Heidelberg, Germany
- 1998 - 2002 BA in Optoelectronics,
Beijing Institute of Technology, Beijing, P. R. China
- 1995-1998 High school
The attached Middle School to Jiangxi Normal University,
Nanchang, P.R. China

PUBLICATIONS

Mor Mishkovsky, Tian Cheng, Arnaud Comment and Rolf Gruetter. *Localized in vivo hyperpolarization transfer sequences*, Magnetic Resonance in Medicine, vol. 68, num. 2, p. 349–352, 2012.

Jessica A. M Bastiaansen; Cheng Tian; Mor Mishkovsky; Joao M. N. Duarte; Arnaud Comment; Rolf Gruetter, *In vivo enzymatic activity of acetylCoA synthetase in skeletal muscle revealed by ¹³C turnover from hyperpolarized [1-¹³C]acetate to [1-¹³C]acetylcarnitine*, Biochimica et biophysica acta, 2013 (in press)

Cheng Tian, Mor Mishkovsky, Jessica A. M. Bastiaansen, Oliver Ouari, Patrick Hautle, Paul Tordo, Ben van den Brandt, and Arnaud Comment, *Method to minimize and monitor in situ the polarization losses in hyperpolarized biomolecules prior to in vivo NMR experiments* (submitted)

Cheng Tian, Mor Mishkovsky, Matthias J. N. Junk, Dariush Hinderberger, Kerstin Muennemann and Arnaud Comment, *Producing radical-free hyperpolarized solutions for in vivo magnetic resonance* (Manuscript in preparation)

CONFERENCE CONTRIBUTIONS

J. Bastiaansen, T. Cheng, R. Gruetter and A. Comment. *Hyperpolarized [1-13C]acetylcarnitine as a tracer for cardiac metabolism*, ISMRM 21th Annual Scientific Meeting, Salt Lake City, USA, 2013.

T. Cheng, J. Jung, A. Comment, R. Gruetter and H. Lei et al., *A comparison of high-pass birdcage coils for small animal imaging at 9.4 and 14T.*, ESMRMB 29th Annual Scientific Meeting, Lisbon, 2012

T. Cheng, M. Mishkovsky, J. Bastiaansen, O. Ouari and P. Hautle et al., *Method to minimize the polarization losses in hyperpolarized biomolecules prior to in vivo MR experiments*. ESMRMB 29th Annual Scientific Meeting, Lisbon, 2012.

J. Bastiaansen, T. Cheng, J. M. N. Duarte, M. Mishkovsky and A. Comment et al. *Kinetic analysis of acetylCoA synthetase activity in skeletal muscle*. ESMRMB 29th Annual Scientific Meeting, Lisbon, 2012.

T. Cheng, M. Mishkovsky, M. Junk, D. Hinderberger and K. Münnemann et al. *Producing radical-free hyperpolarized solutions for in vivo magnetic resonance*. ISMRM 20th Annual Scientific Meeting, Melbourne, Australia, 2012.

J. Bastiaansen, T. Cheng, R. Gruetter and A. Comment. *In vivo real time cardiac metabolism using hyperpolarized acetate*, ISMRM 20th Annual Scientific Meeting, Melbourne, Australia, 2012.

J. Bastiaansen, T. Cheng, M. Mishkovsky, A. Comment and R. Gruetter. *In vivo enzymatic assay of carnitine acetyl transferase and acetylCoA synthetase using hyperpolarized acetate*, ISMRM 20th Annual Scientific Meeting, Melbourne, Australia, 2012.

T. Cheng, M. Mishkovsky and A. Comment. *In situ polarization measurement of hyperpolarized solutions prior to in vivo 9.4T MR experiments*. ISMRM 18th Annual Scientific Meeting, Montreal, Canada, 2011.

J. Bastiaansen, T. Cheng, M. Mishkovsky, A. Comment and R. Gruetter. *Study of acetylcarnitine kinetics in skeletal muscle in vivo using hyperpolarized 1-13C acetate*. ISMRM, Montreal, 2011.

M. Mishkovsky, T. Cheng, A. Comment and R. Gruetter. *Localized in vivo hyperpolarization transfer experiments*. ISMRM 19th Annual Scientific Meeting, Montreal, Canada, 2011.

Y. Takado, T. Cheng, J. Bastiaansen, M. Mishkovsky and R. Gruetter et al. *In vivo real-time metabolic studies of mice brain and skeletal muscle at 9.4T*. Third International Symposium on

Dynamic Nuclear Polarization, Lausanne, 2011.

J. Bastiaansen, T. Cheng, M. Mishkovsky, A. Comment and R. Gruetter. *The metabolic effect of hyperpolarized [1-13C]acetate dosage in vivo*. Third International Symposium on Dynamic Nuclear Polarization, Lausanne, 2011.

J. Bastiaansen, T. Cheng, R. Gruetter and A. Comment. *Kinetics of hyperpolarized [1-13C]acetate metabolism in cardiac muscle*. Third International Symposium on Dynamic Nuclear Polarization, Lausanne, 2011.

J. Bastiaansen, T. Cheng, M. Mishkovsky, A. Comment and R. Gruetter. *Hyperpolarized acetate as a metabolic tracer for skeletal and cardiac muscle energetics*. Hot Topics in Molecular Imaging - TOPIIM, Les Houches, 2011.

M. E. Merritt, M. Mishkovsky, T. Cheng, A. Jindal and Z. Kovacs et al. *In vivo hyperpolarized 89Y studies in a 9.4T animal scanner*. ISMRM 18th Annual Scientific Meeting, May 2008., Stockholm, Sweden, 2010.